Investigation of Mechanical Properties of Asymmetric Lipid Bilayers via Coarse-Grained Simulation

by

Amirali Hossein

Submitted in partial fulfillment of the
requirements for the degree of
Doctor of Philosophy
at
Carnegie Mellon University
Department of Physics
Pittsburgh, Pennsylvania

Advised by Professor Markus Deserno

August 12, 2021

Abstract

Cellular bilayer membranes consist of a diverse array of lipids and proteins. In many cases, the two constituent leaflets of the membrane are known to differ in their composition. However, existing theoretical treatments of membranes have mostly avoided this added level of complexity. In this thesis we use theory and computational methods to explore the relationship between asymmetry, thermodynamics, and mechanical properties of lipid bilayer membranes.

We review the experimental evidence for membrane asymmetry in cells and present an overview of recently developed techniques for creating model asymmetric bilayers. Measurements on these systems have yielded some unexpected results for their material properties, namely, a relatively high bending stiffness compared to their symmetric counterparts. We clarify the distinction between leaflet composition and leaflet stress as two sources of asymmetry in bilayers and develop a theoretical framework for analyzing their interplay in determining the meta-stable equilibrium state of the membrane. We consider the implications for residual stress born by membranes with externally-imposed zero-curvature constraint, for instance, through periodic boundary conditions during simulations.

We use coarse-grained molecular dynamics simulations of buckled membranes of MARTINI lipids to show how asymmetry in leaflet tension, or "differential stress", can cause a significant increase in bending rigidity of the membrane if this asymmetry exceeds a certain critical threshold. We use this observation to explain experimental results and, by inspecting lipid order in the bilayer, attribute stiffening to the formation of highly-ordered domains in the compressed leaflet of the differentially-stressed membrane. We investigate the effect of system parameters such as temperature, lipid type, and size on the stiffening transition and consider their implications. Some pitfalls of using the buckling method for measuring the bending modulus of asymmetric membranes are also examined.

We investigate the role of cholesterol in bilayer asymmetry and, using a simple theoretical model, argue that the relatively rapid flip-flop rate of cholesterol does not necessarily eliminate differential stress. In fact, we show that there are circumstances where addition of cholesterol to the system can generate stress asymmetry. We present evidence from simulations supporting our claim and address conflicting claims from other works on the matter.

Finally, we take a closer look at the coexistence of ordered and disordered phases in the compressed leaflet of an asymmetric bilayer. We use a Hidden Markov Model to classify phases and discuss barrier-crossing issues pertaining to the formation of the ordered phase.

Acknowledgments

I want to thank my academic advisor for providing scientific guidance throughout my graduate research.

I also want to thank members of my thesis committee, and I want to express gratitude to graduate students and faculty in the biophysics group at Carnegie Mellon for all the invaluable discussions during this project.

Finally, I want to thank my family for their support.

Publications

This thesis is based on research published in the following publications, parts of which have been reproduced here.

Hossein, A. and Deserno, M. (2020) Spontaneous curvature, differential stress, and bending modulus of asymmetric lipid membranes, *Biophysical journal*, **118**, 624-642.

Hossein, A. and Deserno, M. (2021) Stiffening transition in asymmetric lipid bilayers: The role of highly ordered domains and the effect of temperature and size, *The Journal of Chemical Physics*, **154**, 014704.

Contents

List of Tables

List of Figures

Chapter 1

Introduction

After introducing biological lipid membranes and their constituent molecules and the foundations of molecular dynamics simulations in this chapter, we spend the next chapter to establish the experimental evidence for ubiquitousness of asymmetry in lipid bilayers and its unexpected effect on their bending rigidity, and provide a theoretical framework for analyzing curvature elastic properties of asymmetric membranes. In chapter 3 simulations are used to explain the stiffening phenomenon observed in the experiments and the effect of system parameters such as temperature and size on this phenomenon are evaluated. Chapter 4 addresses concerns about the possibility that presence of rapidly flip-flopping species such as cholesterol in lipid bilayers can invalidate our proposed mechanism for stiffening of asymmetric bilayers. Finally, chapter 5 takes a closer look at the proposed coexistence of fluid and gel phases in the compressed leaflet of stiffened asymmetric membranes.

1.1 Biological background

Biological lipid membranes form the boundary of eukaryotic cells and divide them into compartments with specialized functionality called organelles. Their main building blocks are hundreds of different types of lipids and a large array of embedded proteins [1]. Here we will focus on phospholipids and cholesterol due to their relevance to our work.

1.1.1 Phospholipids

Phospholipids are amphiphilic molecules consisting of a hydrophilic polar head group containing a phosphate group and two hydrophobic hydrocarbon tails. The tails are usually fatty acids and can differ in length, normally containing between 14 and 24 carbon atoms. The tails can have one or more double bonds (they are then called "unsaturated"), or none ("saturated") [2,3]. The amphiphilic nature of phospholipids causes them to self-assemble into structures such as bilayers and micelles, depending

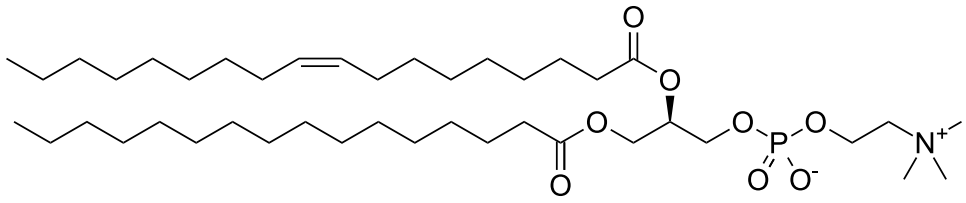

Figure 1.1: Chemical structure of 1-palmitoyl-2-oleoylphosphatidylcholine (POPC).

on the shape of the lipid, specifically the relative sizes of its head and tail portions [4, 5].

Under physiological conditions, lipid membranes are typically found in a fluid (or liquid-crystalline) phase, where the hydrocarbon chains are conformationally disordered. In lower temperatures they can enter a variety of more ordered phases, such as the gel phase, in which lipids are packed much more densely and have much lower rates of diffusion [11, 12]. At the same temperature, lipids with saturated tails tend to form more ordered bilayers compared to lipids with tails containing unsaturated double bonds [6].

Combining various fatty acids with different length and level of saturation with head-groups that differ in size, polarity, and charge leads to a diverse array of phospholipids which can form bilayers, having an equally diverse range of physical properties [2] (for instance, the ratio of the size of head-group compared to the hydrophobic tail strongly affects the preferred, or "spontanous", curvature of a monolayer leaflet made from that lipid [4]), although not all lipid species are equally abundant in biological systems that interest us, as will be discussed in more detail in section 2.1.

Fig. 1.1 shows the chemical structure of 1-palmitoyl-2-oleoylphosphatidylcholine[1] (POPC), an example of a phospholipid.

1.1.2 Cholesterol

In addition to phospholipids, the lipid bilayers in many animal plasma membranes contain large amounts of cholesterol (as much as 50%) [7–10]. Cholesterol is a sterol, containing a rigid ring structure, to which a single polar hydroxyl group and a short non-polar hydrocarbon chain are attached. The cholesterol molecules orient themselves in the bilayer with their hydroxyl group close to the polar head groups of adjacent phospholipid molecules [2]. Cholesterol modulates the properties of lipid bilayers. For example, addition of cholesterol to the membrane tends to stiffen it [2,3]. It is also known that adding cholesterol to a binary mixture of lipids can lead to emergence of coexisting liquid phases known as "liquid ordered" (L_o) and "liquid disordered" (L_d) [13–15]. Fig. 1.2 shows the chemical structure of cholesterol.

[1]This naming convention identifies the lipid's two acyl chains as belonging to palmitic and oleic acid and the head-group as choline.

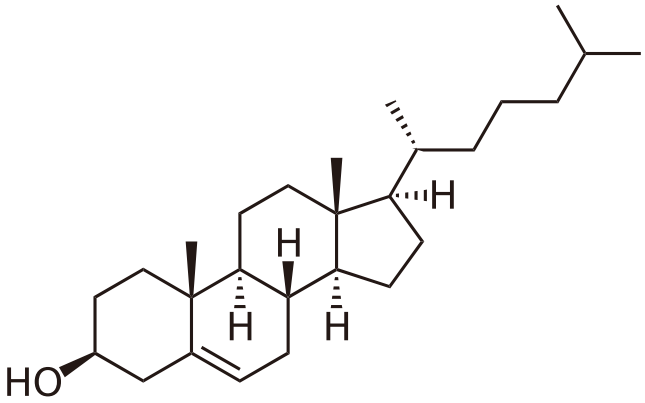

Figure 1.2: Chemical structure cholesterol.

1.2 Molecular dynamics simulations

Computer simulations are an invaluable tool for obtaining qualitative and quantitative insights about the physical behaviour of heterogeneous systems, such as biomolecules or their assemblies [20]. They complement both experiment and theory by allowing us to compare theoretical predictions with results of virtual experiments that are not feasible in reality.

In molecular dynamics (MD) simulations we numerically integrate the classical equations of motion for a set of particles representing our system over a period of time. The resulting time series is called a trajectory, which can be analyzed in order to extract relevant information [22]. Assuming ergodicity holds, for a system in equilibrium the time average of an observable over the trajectory can be taken as a stand-in for its ensemble average [29].

The natural ensemble of MD simulations is the constant-energy, constant-volume microcanonical ensemble. In order to sample from constant-temperature or constant-pressure ensembles, we generally need to add additional variables, known as extended degrees of freedom, to our system to create a "thermostat" or a "barostat". These constructs model the external environment and regulate the time-averaged values of temperature and pressure [16–18, 21, 23, 27].

The interactions between the particles representing our system in an MD simulations are described by a force field (FF). There exists a wide variety of FFs which can be categorized based on their level of resolution. The highest-resolution models are atomistic (or all-atom) models in which every atom is represented with a corresponding particle. Although available computational power has increased significantly since the days of the first MD simulation of a biomolecule nearly four decades ago [24], the simulation time-scales and length-scales necessary for investigating many biological phenomena of interest are still not readily accessible. A solution to this problem is using coarse-grained (CG) models in which multiple atoms are combined into a single

particle while the important physics of the system is preserved [19, 25, 26, 28, 30, 31].

1.3 MARTINI Model

The MARTINI force field [38, 39] is a coarse-grained model designed to be computationally fast and applicable to a broad range of biomolecular systems. It has been shown that it can accurately reproduce many structural, dynamic, and thermodynamic properties of a variety of systems and state points [35–38].

On average the MARTINI model maps four heavy atoms to one interaction center, with an exception for ring-like molecules, like cholesterol, which are mapped with a higher resolution of up to two heavy atoms to one bead to satisfy the geometric specificity of small ring-like fragments or molecules. MARTINI is an explicit-solvent model with water beads that each correspond to four water molecules.

The model consists of four main types of beads: polar (P), non-polar (N), apolar (C), and charged (Q), with each type having subtypes distinguished by their hydrogen-bonding capabilities and degree of polarity. The mass of the beads is 72 amu (equal to four water molecules) for all beads except those in ring structures for which the mass is 45 amu.

In this project we worked with the MARTINI representations of the following four glycero-phosphocholine-lipids specifically: DLPC (1,2-dilauroyl-*sn*-glycero-3-phosphocholine), which has two fully saturated C12 chains; DPPC (dipalmitoyl-*sn*-glycero-3-phosphocholine), which has two fully saturated C16 chains; POPC (1-palmitoyl-2-oleoyl-*sn*-glycero-3-phosphocholine), which has a saturated C16 *sn1*-chain and a singly (cis-)unsaturated C18 *sn2*-chain; and finally DLiPC (dilinoleoyl-*sn*-glycero-3-phosphocholine), a lipid with two doubly (cis-)unsaturated C18 chains[2]. Since MARTINI cannot properly distinguish between 16 or 18 carbons, the latter lipid is typically referred to as DIPC in the MARTINI lipidome, and we will do so, too.

Some of our simulations also contain additional cholesterol. While this lipid has been part of the original MARTINI suite [38], its parametrization was known to have numerical stability issues (due to the rigid ring structure) and exhibited several physical shortcomings; for instance, it failed to preserve fluidity of liquid-ordered domains [40, 45]. These issues were successfully addressed in a recent reparametrization by Melo *et al.* [42]. Unfortunately, their new force field relies on virtual sites, which are not supported in the present version of GROMACS-LS [43, 44] (the package we use to calculate the lateral stress profile—see below). We hence employed a revision of the Melo force field, created by Ingólfsson [41], which strives to capture the improvements achieved in Ref. [42] without the need for virtual sites.

[2]In these names the prefix "cis" refers to the configuration of the unsaturated (double) bond, indicating that both hydrogens are on the same side of the hydrocarbon chain. The prefix "sn" (for stereospecific numbering) specifies stereoisomers of chiral molecules, i.e. molecules that cannot be superposed on their mirror image by a combination of rotations and translations.

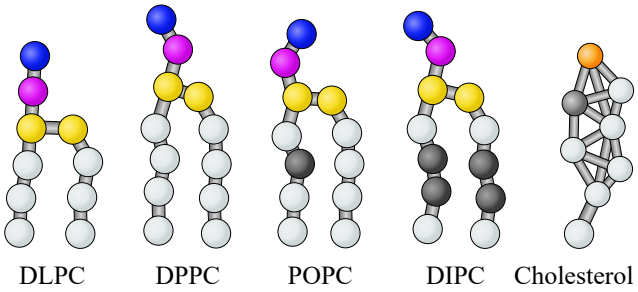

Figure 1.3: The four phospholipids used in our simulations, together with the cholesterol model. The different bead colors represent: choline group (blue); phosphate group (magenta); glycerol backbone (yellow); C_4H_8 hydrocarbon repeat with single bonds (light gray); C_4H_6 hydrocarbon repeat with a cis double bond (dark gray). In the cholesterol figure, the small white beads are smaller versions of the hydrocarbon beads, the gray bead is slightly more polar, and the orange bead is the hydroxyl group.

Fig. 1.3 illustrates the four phospholipids we use, together with the cholesterol model.

1.4 Basic theory

For length scales a few times larger than the thickness of a membrane, lipid bilayers can be effectively modeled as continuum elastic sheets and a simple continuum theory called the Helfrich theory can be used to describe them [145]. According to this theory the membrane's shape is governed by the energy functional

$$\mathcal{E}[S] = \int_S \mathrm{d}A \Big\{ \frac{1}{2}\kappa(K - K_0)^2 + \bar{\kappa} K_G \Big\} , \tag{1.1}$$

where $K = c_1 + c_2$ is the total curvature (sum of the two principal curvatures), K_0 is the spontaneous bilayer curvature, and κ is the bilayer bending modulus. $K_G = c_1 c_2$ and $\bar{\kappa}$ are Gaussian curvature and Gaussian curvature modulus, respectively. A typical value for bending modulus of a fluid bilayer is $\approx 20 k_\mathrm{B} T$ [32]. The Helfrich Hamiltonian can be made more complex by adding more terms related to other membrane observables, such as lipid tilt [33]. However, on large enough scales they act as merely minor corrections to the overall bending physics and would hence not be necessary for our current project.

Another important elastic parameter of membranes is the area expansion modulus, which relates the square of area strain and the energetic cost resulting from that strain

$$E_\mathrm{stretch} = \frac{1}{2} K_A \frac{(A - A_0)^2}{A_0} , \tag{1.2}$$

where E_{stretch} is the stretching energy of the elastic surface, A is the area, A_0 is the equilibrium area, and K_A is the area expansion modulus, with a typical value of $\approx 240\text{mN/m}$ for fluid bilayers of common phospholipids [34, 114].

Chapter 2

Nature of asymmetry

2.1 Membrane asymmetry in real cells

It has long been suspected that many biological lipid membranes have leaflets with differing compositions, supported by experiments on plasma membranes (PM) of animal red blood cells (RBCs) going back for as long as half a century [60, 61, 71, 72]. (It is however worth mentioning that membrane asymmetry can exists even if the two leaflets are identical, for example, through a difference between the solute concentrations in either side of the bilayer.)

Recently, modern mass spectroscopy techniques were used to comprehensively measure the lipid components of the two PM leaflets in human RBCs [53,55], broadly confirming classical estimates of PM asymmetry, showing headgroup asymmetry with an outer (exoplasmic) leaflet primarily comprising the choline-headgroup phospholipids phosphatidylcholine (PC) and sphingomyelin (SM) and an inner (cytoplasmic) leaflet with greater quantities of phosphatidylethanolamine (PE) and the charged lipids phosphatidylserine (PS) and phosphatidylinositol (PI). Moreover, lipidomics shows interleaflet differences in acyl chain structure, with inner leaflet lipids being about twice as unsaturated compared to the outer leaflet lipids [50, 53]. Lorent *et al.*observed that the PM asymmetry is also reflected in the lipid-accessible surface area of single-pass protein transmembrane domains (TMDs), with the TMD regions being relatively thinner in the exoplasmic leaflet [53]. In addition to the late secretory and endocytic membranes, bioinformatics analysis of the shape of TMDs suggests asymmetry of PM is ubiquitous in eukaryotic organisms [53]. This leads to the conclusion that membrane asymmetry plays a fundamental role in the function of eukaryotic cells.

The most abundant single component of the PM is cholesterol at about 40 mol%, and therefore understanding interleaflet distribution of cholesterol is of utmost importance. However, existing evidence on cholesterol distribution spans a range of possible outcomes, from 80% of cholesterol residing in the inner leaflet to 90% in the outer leaflet [48, 52, 69].

It is important to note that bilayers with asymmetric composition are not in a state of thermodynamic equilibrium [46]. If left undisturbed, they will approach the higher-entropy symmetric state through spontaneous movements of lipids between the leaflets, called "flip-flops". For most lipid species flip-flops happen on time-scales much longer than time-scales (hours or days [119]) of relevant biological processes, although cholesterol is an exception to this, as its flip-flop rate is believed to be in the microsecond range [65–68]. Evidently, living cells are not in equilibrium and their membranes' asymmetric composition is maintained through active processes involving energy-consuming enzymes such as flippases, which are transporters that move lipids from the exoplasmic to the cytosolic face, and floppases, which transport in the reverse direction [47]. There also exist scramblases, which act as passive catalysts that relax asymmetry at a rate much faster than that of spontaneous flip-flops [49, 57].

The ubiquity of membrane asymmetry in cells, and the required energy for its active maintenance, demonstrates its important functional role. Examples [50] of phenomena where active maintenance or relaxation of membrane asymmetry plays an essential part include maintenance and pruning of neuronal connections [51, 58], muscle development [70], mammalian fertilization [62], and immune signaling [54, 56, 59, 63].

2.2 Experiments

Until very recently it was essentially impossible to artificially create well-controlled asymmetric model membranes, in which the consequences of asymmetry could be explored while sidestepping many of the confounding factors present in living systems. But this has changed with the advent of multiple preparation techniques.

In the *phase transfer protocol* [87, 89, 93, 97] the vesicles are essentially assembled "one monolayer at a time": we start with a water-in-oil emulsion with one type of lipid forming monolayers around water droplets that are then pushed through a second water-oil interface with another type of lipid, making vesicles with two different type of lipids in either of their leaflets. Fig. 2.1 shows a schematic of generating a Giant Unilamellar Vesicle (GUV) with asymmetric lipid composition using the phase transfer protocol [84].

Another method for generating asymmetric model membranes is the *lipid exchange protocol* [77–80], in which lipids on the outside of a vesicle are partially replaced by other ones that are loaded into a soluble exchange agent, typically methyl-β-cyclodextrin.

The most recently developed method is the *hemifusion protocol* [85], in which asymmetry is achieved through the hemifusion of giant unilamellar vesicles and a supported lipid bilayer, leading to the lipid exchange of the fused outer leaflets mediated by lipid diffusion.

Even though no mechanism exists to also *maintain* this asymmetry, the beyond-hours time scale for decay ensures that many consequences of asymmetry can still be

studied, provided the experiments can be done quickly enough.

With the advent of these new model systems, much focus has been devoted to optimizing these protocols, examining biological questions enabled by these techniques (such as the impact of asymmetry on protein function [91], protein sorting [98], directional peptide insertion [99], and inter-leaflet coupling of domains [88, 94]), and exploring novel applications (such as using the phase transfer protocol for cargo compartmentalization [82, 83] and in synthetic biology [76, 86, 95, 96, 100, 101]).

Less emphasis has been placed on probing the materials properties of these systems, even though the broken up-down symmetry could have profound consequences for them. Indeed, recent biophysical investigations have found that basic thermodynamic and mechanical properties of asymmetric membranes can also be strongly affected in unexpected and posssibly consequential ways. For instance, Eicher *et al.* [81] found that the main phase transition in asymmetric membranes is unusual and depends on how the asymmetry is oriented relative to the curvature of the asymmetric liposome. And several studies have found that the bending rigidity of asymmetric vesicle can be much larger than the naïvely expected average of the two cognate symmetric membranes: Elani *et al.* [84] generated asymmetric GUVs with DOPC in one leaflet and POPC in the other leaflet using phase transfer and found them to be about 150% stiffer than their symmetric counterparts. Karamdad *et al.* [90] used a microfluidic technique based on phase transfer to create asymmetric POPC-DOPC GUVs and found them to be about 50% stiffer than symmetric GUVs with an equal 50:50 composition of POPC and DOPC in both leaflets. In both experiments the bending rigidity was measured using fluctuation analysis. A similar experiment by Chiarot *et al.* [92], in which they measured bending rigidity of asymmetric DMPC-DOPC GUVs using micropipette aspiration techniques, produced similar results (asymmetric bilayers about 50% stiffer than symmetric counterparts).

This is surprising for at least two reasons. First, leaflet asymmetry obviously affects a bilayer's spontaneous curvature; but this only enters the curvature energy at the linear level, whereas the bending rigidity multiplies the *square* of the curvature and hence involves qualitatively different physics. And second, if asymmetry does not change the bending rigidity of an individual leaflet from the value it would have in a symmetric membrane, then it is hard to see why the rigidity of an asymmetric membrane would not be the average rigidity of the two corresponding symmetric bilayers.

It is of note that Elani *et al.* [84] also conducted control experiments, comparing stiffness of symmetric bilayers made using their phase transfer method with those made using the standard method of electroformation, and found no difference in their bending rigidities. This is crucial in dispelling the possibility of the observed stiffening being attributed to artifacts of the vesicle preparation method, such as entrapment of trace amounts of oil in the hydrophobic core of the bilayers. We will revisit the results of these experiments in section 3.3.

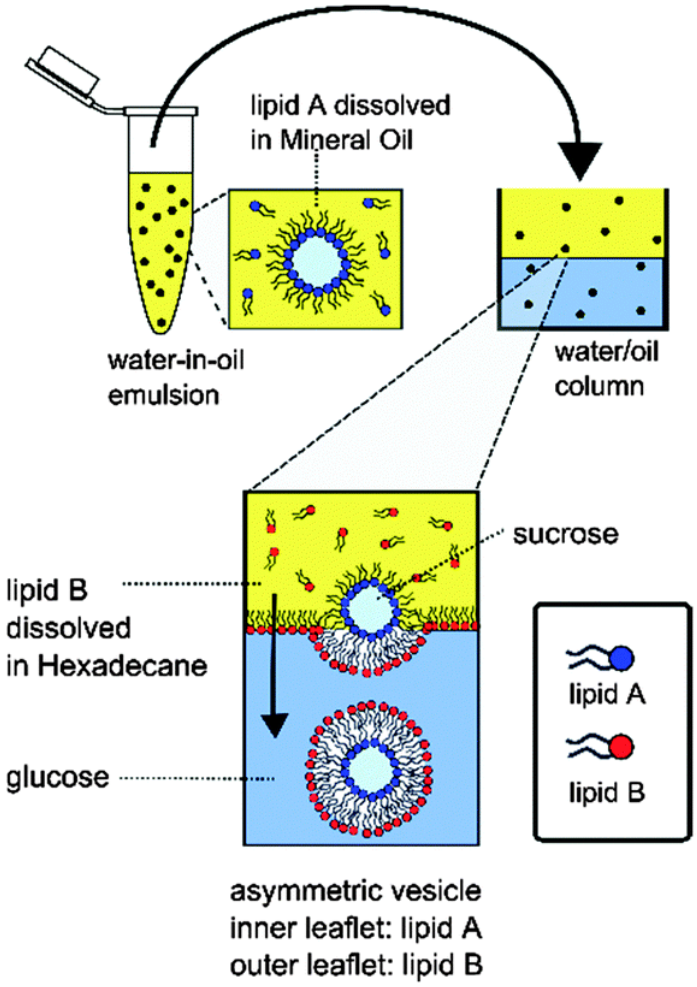

Figure 2.1: Schematic of asymmetric GUV preparation via phase transfer. Water droplets are encased in a monolayer of type A lipids in a water-in-oil emulsion, which is then added to a water-oil column with type B lipids dissolved in the oil phase and assembled as a monolayer at the interface. Gravity lowers the droplets through the column, enveloping them by a second monolayer, forming asymmetric GUVs with lipid A in the inner leaflet and lipid B in the outer leaflet. Figure reproduced from Ref. [84] with permission from the Royal Society of Chemistry.

2.3 Theory

In this section we present a general review of the connection between bilayer asymmetry, spontaneous curvature, and differential stress. Bilayer asymmetry can manifest in two independent observables: leaflet composition and leaflet stress. Both give rise to characteristic spontaneous curvatures, and the interplay between bending moments and lateral stresses determine the overall spontaneous curvature of the bilayer and

describe its elastic properties. This subject has been discussed in a number of publications in the past [102, 115–117, 120], however, we wish to revisit the key ideas, because some of the implications appear to not have been explicitly spelled out.

2.3.1 Leaflet composition

Consider a compositionally asymmetric membrane whose two leaflets are characterized by monolayer bending rigidities $\kappa_{\mathrm{m}+}$ and $\kappa_{\mathrm{m}-}$ and spontaneous curvatures $K_{\mathrm{m}+}$ and $K_{\mathrm{m}-}$. We will use the subscript "m" to indicate monolayer observables and labels "+" and "−" for the upper and lower leaflet, respectively. The same sign convention is used for bilayer quantities and the upper leaflet. In all following discussions we ignore the Gaussian curvature contribution, which merely contributes an overall constant as long as the topology stays the same.

If we impose a weak curvature K, permit the two leaflets to slide past each other and ensure that they are individually without tension, then the energy density can be written as the sum of two bending terms:

$$e_0(K) = \frac{1}{2}\kappa_{\mathrm{m}+}(K - K_{\mathrm{m}+})^2 + \frac{1}{2}\kappa_{\mathrm{m}-}(K + K_{\mathrm{m}-})^2 \ . \tag{2.1}$$

The first term captures the upper leaflet, the second term the lower one, and the swapped sign of $K_{\mathrm{m}-}$ allows for the fact that the lower leaflet curvature is flipped with respect to the upper one.

We can find the spontaneous materials curvature of the bilayer $K_{0\mathrm{b}}$ by minimizing this energy density. This curvature, at which the net *bending* stress vanishes, and which is hence identified with the subscript "b", is the *rigidity-weighted difference* of the two spontaneous leaflet curvatures:

$$\left.\frac{\partial e_0(K)}{\partial K}\right|_{K=K_{0\mathrm{b}}} = 0 \quad \Rightarrow \quad K_{0\mathrm{b}} = \frac{\kappa_{\mathrm{m}+}K_{\mathrm{m}+} - \kappa_{\mathrm{m}-}K_{\mathrm{m}-}}{\kappa_{\mathrm{m}+} + \kappa_{\mathrm{m}-}} \ . \tag{2.2}$$

Using this, the bending energy density can be rewritten as

$$e_0(K) = \text{const.} + \frac{1}{2}\kappa(K - K_{0\mathrm{b}})^2 \ , \tag{2.3}$$

where the bilayer curvature modulus is the sum of the monolayer curvature moduli, $\kappa = \kappa_{\mathrm{m}+} + \kappa_{\mathrm{m}-}$, and the constant can be absorbed into the net tension.

Since $K_{\mathrm{m}+}$ and $K_{\mathrm{m}-}$ can be large, this can be true for $K_{0\mathrm{b}}$, too. As a numerical example, let us look at the membrane parameters reported in Table 2.1, which are determined from atomistic simulations.

For an asymmetric DOPC-POPC membrane, we get $K_{0\mathrm{b}} \approx -0.017\,\mathrm{nm}^{-1}$ or a curvature radius of $R_{0,\mathrm{b}} = 2|K_{0\mathrm{b}}^{-1}| \approx 120\,\mathrm{nm}$, a typical size for a large unilamellar vesicle (LUV) or many intracellular transport vesicles. But if we take an asymmetric DOPC-DOPE membrane, we get $K_{0\mathrm{b}} \approx 0.1\,\mathrm{nm}^{-1}$; a sphere with this curvature would have a radius of $R_{0,\mathrm{b}} = 2|K_{0\mathrm{b}}^{-1}| \approx 20\,\mathrm{nm}$, typical for small unilamellar vesicles (SUV) or synaptic vesicles.

lipid	T [K]	κ_m [pN nm]	K_m [nm^{-1}]	d [nm]
DOPC	298	59	-0.0714	2.737
POPC	303	66	-0.0317	2.752
DOPE	298	59	-0.2703	2.996

Table 2.1: Material parameters for some typical lipid systems, determined from atomistic simulations [123]. The length d is the distance between the average C_2 carbon position in the leaflets and is a measure of the hydrophobic thickness of the bilayer.

2.3.2 Leaflet stress

Even if the bilayer satisfies $K = K_{0\mathrm{b}}$, it is generally *not* in an equilibrium state, since the underlying asymmetric lipid distribution can relax into a symmetric one through lipid flip-flops between the two leaflets. However, given the relatively long time scales associated with this process (times between many hours and many days have been repeatedly measured for not-too-short lipids in unsupported membranes [64]), on time scales much shorter than the typical flip-flop time, the asymmetric distribution can be treated as a metastable equilibrium.

But in that case, *other* metastable states made possible by the slow flip-flop rate must also be considered—chiefly among them *differentially stressed* states in which the mechanical tensions $\Sigma_\pm$ in the two leaflets are unequal [105, 112, 115, 122]. The easiest situation to consider, and to which we will restrict our analysis here, is one in which the two leaflets individually exhibit a nonzero tension that is equal in magnitude but opposite in sign such that the *net* bilayer tension $\Sigma = \Sigma_+ + \Sigma_-$ vanishes. In such a bilayer, one layer is subject to tensile stress (positive tension), and the other one is subject to compressive stress (negative tension).

Differentially stressed membranes can relax by bending, similar to bimetallic strips. We will assume that this happens as illustrated in Fig. 2.2; specifically, we demand that the two leaflets share a common midplane before and after a change in curvature. Assume therefore that at some particular spontaneous curvature $K_{0\mathrm{s}}$ the differential area strain vanishes (hence the additional subscript "s"). Notice that unlike $K_{0\mathrm{b}}$, which by Eqn. (2.2) is a material parameter, $K_{0\mathrm{s}}$ instead characterizes the lipid packing in the two leaflets, which is likely set by whatever kinetics process creates the bilayer.

From the parallel surface theorem [103, 104], the area element $\mathrm{d}A_\pm$ of a parallel surface at a normal distance $z_\pm$ from the bilayer midplane above or bellow an area element $\mathrm{d}A$ with curvature K is given by

$$\mathrm{d}A_\pm = \mathrm{d}A\big(1 \pm z_\pm K\big) + \mathcal{O}(z_\pm^2). \tag{2.4}$$

If $\mathrm{d}A_{\pm 0}$ is the area element of the respective planes at curvature $K_{0\mathrm{s}}$ where the area

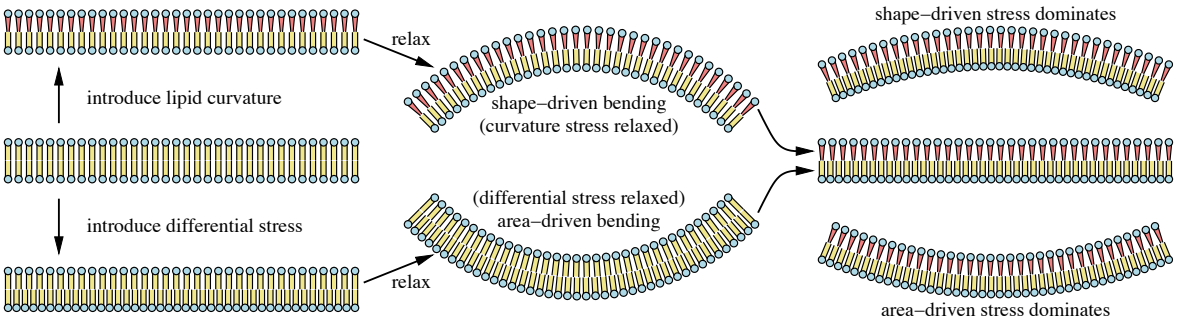

Figure 2.2: Illustration of the interplay between a spontaneous curvature $K_{0\mathrm{b}}$ driven by lipid shape and a spontaneous curvature $K_{0\mathrm{s}}$ driven by area strain. An initially flat and relaxed membrane can be asymmetrically stressed either by a leaflet imbalance of lipid shape, or a leaflet imbalance in the area density. Such membranes relax by assuming a shape- or area-driven spontaneous curvature. When both effects occur simultaneously (see right hand side), the resulting spontaneous curvature K_0 arises as the balances expressed in Eqn. (2.9), which can include an asymmetric, flat, and differentially stressed membrane as a special case.

strain from lipid packing is relaxed, changing the curvature from $K_{0\mathrm{s}}$ to K creates a *local* differential area strain

$$\gamma_\pm(K) = \frac{\mathrm{d}A_\pm(K) - \mathrm{d}A_{\pm 0}}{\mathrm{d}A_{\pm 0}} = \pm(K - K_{0\mathrm{s}})z_\pm + \mathcal{O}(z_\pm^2) \tag{2.5}$$

in leaflet reference surfaces a distance $z_\pm$ away from the bilayer midplane. But since individual leaflets can slide, the physically meaningful strain is not the local one, but the one distributed over the whole membrane. This yields a *non-local* curvature elastic energy density that has been included in numerous membrane models [106–108, 111, 118, 121]

$$e_{\mathrm{nl}} = \frac{1}{2}K_{A,\mathrm{m}+}\gamma_+^2(\bar{K}) + \frac{1}{2}K_{A,\mathrm{m}-}\gamma_-^2(\bar{K}) \tag{2.6a}$$

$$= \frac{1}{2}\kappa_{\mathrm{nl}}(\bar{K} - K_{0\mathrm{s}})^2 \ , \tag{2.6b}$$

which quadratically penalizes the deviation of the surface-averaged curvature

$$\bar{K} = \frac{1}{A}\int_{\mathcal{S}} \mathrm{d}A\ K \tag{2.6c}$$

from the differential stress curvature $K_{0\mathrm{s}}$ with the non-local bending rigidity[1]

$$\kappa_{\mathrm{nl}} = K_{A,\mathrm{m}+}z_+^2 + K_{A,\mathrm{m}-}z_-^2 \ . \tag{2.6d}$$

[1] A similar non-local bending rigidity κ' is defined in Refs. [111,118], however with a curious extra factor of π, so that we have $\kappa_{\mathrm{nl}} = \pi\kappa'$.

Making the additional simplifying assumption that $z_+ = z_- \equiv z_0$ and defining the bilayer area expansion modulus as $K_A = K_{A,\mathrm{m}+} + K_{A,\mathrm{m}-}$, we have

$$\kappa_{\mathrm{nl}} \approx K_A z_0^2 \ . \tag{2.7}$$

Choosing $z_\pm$ to be the surfaces at which bending and stretching deformations decouple (called the neutral surfaces [109]), then—by definition—the associated elastic energy (2.6b) of stretching or compression simply adds to the curvature energy from Eqn. (2.1). Up to a constant, which can be subsumed in the net tension, this leads to the total energy density

$$e_{\mathrm{tot}}(K, \bar{K}) = \frac{1}{2}\kappa(K - K_{0\mathrm{b}})^2 + \frac{1}{2}\kappa_{\mathrm{nl}}(\bar{K} - K_{0\mathrm{s}})^2 \ . \tag{2.8a}$$

These are two quadratic curvature terms, a local and a nonlocal one, for which $K_{0\mathrm{b}}$ and $K_{0\mathrm{s}}$ are the respective spontaneous curvatures. The first term is traditionally referred to as the "spontaneous curvature model" [145], and the second as the "area difference elasticity" model [111]. These are usually viewed as two alternative models for describing curvature elasticity in the presence of an asymmetry that prefers a nonzero bilayer curvature. It is worth noting, however, that not only do these two models describe conceptually very different origins of such an asymmetry, they also describe different elastic energies: bending versus stretching. Therefore it is legitimate to write the total elastic energy as their sum.

For simplicity, we limit ourselves to constant mean curvature surfaces (such as planes, spheres, cylinders, or unduloids), for which $K \equiv \bar{K}$, and again calculate the overall curvature at which the energy is minimized. We get

$$\left.\frac{\partial e_{\mathrm{tot}}(K, K)}{\partial K}\right|_{K=K_0^\star} = 0 \quad \Rightarrow \quad K_0^\star = \frac{\kappa K_{0\mathrm{b}} + \kappa_{\mathrm{nl}} K_{0\mathrm{s}}}{\kappa + \kappa_{\mathrm{nl}}} \ . \tag{2.9}$$

A new spontaneous curvature, $K_0^\star$, once again arises as a weighted mean—this time of the curvatures associated with optimal bending, $K_{0\mathrm{b}}$, and optimal stretching, $K_{0\mathrm{s}}$, for which κ and κ_{nl} are the respective weighting factors.[2]

In the balance condition (2.9) the stretching penalty is expected to be the dominant term, because bending is the softer degree of freedom, and so we should expect $\kappa/\kappa_{\mathrm{nl}}$ to be small. Indeed, the polymer brush model [114] tells us that a reasonable approximation for the bending rigidity of a bilayer is $\kappa \approx K_A d_{\mathrm{h}}^2/24$, where d_{h} is the hydrophobic thickness of the bilayer, which is typically about 2/3 of its total width d. Since furthermore $z_0 \approx d_{\mathrm{h}}/2$ [110, 127] and $\kappa_{\mathrm{nl}} \approx K_A z_0^2$, we find $\kappa/\kappa_{\mathrm{nl}} \approx 1/6$.

[2]Incidentally, up to a constant the energy has the form $\frac{1}{2}C(K - K_0^\star)^2$ with some "effective" bending rigidity $C = \kappa + \kappa_{\mathrm{nl}}$. This is not surprising, since Eqn. (2.8a) essentially describes two springs in parallel. However, C should *not* be interpreted as a local bending rigidity, since the derivation relied on constant mean curvature surfaces in order to trivially combine the local and the non-local bending part.

Despite being energy minimized, the curvature-relaxed state from Eqn. (2.9) with $K = K_0^\star$ exhibits a differential strain $\gamma_\pm = \pm(K_0^\star - K_{0\mathrm{s}})z_\pm$ and a concomitant differential stress

$$\Sigma_\pm = K_{A,\mathrm{m}\pm}\gamma_\pm \approx \pm\frac{\kappa}{2z_0}\frac{K_{0\mathrm{b}} - K_{0\mathrm{s}}}{1 + \kappa/\kappa_{\mathrm{nl}}} \ . \tag{2.10}$$

This stress vanishes only in the special case where $K_{0\mathrm{s}} = K_{0\mathrm{b}}$. But other scenarios are also possible: for instance, a flat membrane in which the differential stress exactly cancels the bending moment induced by the spontaneous curvature $K_{0\mathrm{b}}$; in other words, *an asymmetric bilayer that nevertheless has zero net spontaneous curvature*: $K_0^\star = 0$. From Eqn. (2.9) this implies $K_{0\mathrm{s}} = -(\kappa/\kappa_{\mathrm{nl}})K_{0\mathrm{b}}$ and therefore

$$\Sigma_\pm(K_0^\star = 0) = \pm\frac{\kappa K_{0\mathrm{b}}}{2z_0} \ . \tag{2.11}$$

The physical meaning of the sign can be understood as follows: if from a spontaneous curvature point of view we have $K_{0\mathrm{b}} > 0$, so that the upper leaflet "wants" to be convex, it also needs to be under a positive tension to pull it back into a flat state. Using the previously discussed numbers, an asymmetric DOPC-POPC membrane in such a state would then end up with a noticeable differential stress of $|\Sigma_\pm| \approx 0.8\,\mathrm{mN/m}$, while for a DOPC-DOPE membrane we get $|\Sigma_\pm| \approx 4\,\mathrm{mN/m}$, which is a very large value.

Of course, these two particular states of stress just discussed are simply special cases in a *continuum of states* that can be parametrized by $K_{0\mathrm{s}}$, or (as long as $K_{0\mathrm{b}} \neq 0$) by the dimensionless stress-curvature parameter α_{sc} defined as

$$\alpha_{\mathrm{sc}} := \frac{1 - K_{0\mathrm{s}}/K_{0\mathrm{b}}}{1 + \kappa/\kappa_{\mathrm{nl}}} \ , \tag{2.12}$$

which labels states harbouring the differential stress

$$\Sigma_\pm(\alpha_{\mathrm{sc}}) = \pm\alpha_{\mathrm{sc}} \times \frac{\kappa K_{0\mathrm{b}}}{2z_0} \ . \tag{2.13}$$

The two previously mentioned cases correspond to $\alpha_{\mathrm{sc}} = 0$, a membrane that assumes its "materials-based" curvature $K_{0\mathrm{b}}$ and is free of differential stress, and $\alpha_{\mathrm{sc}} = 1$, a flat membrane that exhibits differential stress, respectively. Since α_{sc} can vary continuously, asymmetric membranes really constitute (at least) a *one-parameter family of metastable states*, and for this reason *they are insufficiently characterized by their compositional asymmetry alone*. In other words, there is no particular value for the differential stress (say, zero) that is the "right" one, unless there is some independent argument that would permit reducing this one-parameter family of legitimate states to that special case.

2.3.3 Residual stress

The interplay between asymmetry and tension in lipid bilayers gives rise to another intriguing issue, recently identified in simulations [124, 125]: the state point at which the areas per lipid in each leaflet of an asymmetric membrane agree with those in their tensionless symmetric counterparts need not coincide with the point where the differential stress vanishes. This is of practical relevance: if one wishes to simulate asymmetric membranes whose leaflets are individually tensionless (recall: a possible choice, even though not the only valid one), then it is insufficient to match the specific lipid areas in each leaflet to those in the cognate symmetric bilayers. (Ref. [124] proposes a method to correct for this, if zero tension is indeed what one wants.) Here we will attempt to rationalize this empirical finding within the framework developed in the preceding sections.

Taking the specific area from simulations of a flat symmetric membrane is equivalent to imposing $K_{0\mathrm{s}} = 0$; but the bending torque that arises in the asymmetric case induces a nonzero spontaneous bilayer curvature and associated differential stress, given by Eqns. (2.9) and (2.10), respectively (while setting $K_{0\mathrm{s}} = 0$ in both equations). However, for such a membrane to be spontaneously flat, it would need to be subject to the slightly larger differential stress from Eqn. (2.11). The difference between these two is

$$\Delta\Sigma_\pm = \Sigma_\pm(K_0^\star = 0) - \Sigma_\pm(K_{0\mathrm{s}} = 0) \tag{2.14a}$$

$$= \pm\frac{\kappa K_{0\mathrm{b}}}{2z_0}\,\frac{1}{1+\kappa_{\mathrm{nl}}/\kappa}\ . \tag{2.14b}$$

In other words, forcing the membrane to be planar requires this much more differential stress. Of course, we cannot "summon" additional intrinsic stress; but spanning a membrane patch into a simulation box amounts to *externally* imposing the *negative* of this differential stress via the applied periodic boundary conditions. This results in the observed *residual differential stress* of

$$\Sigma_\pm^{(\mathrm{res})} = -\Delta\Sigma_\pm = \mp\frac{\kappa K_{0\mathrm{b}}}{2z_0}\,\frac{1}{1+\kappa_{\mathrm{nl}}/\kappa} \approx \mp\frac{\kappa K_{0\mathrm{b}}}{14z_0}\ , \tag{2.15}$$

where in the last step we used the previously discussed estimate $\kappa_{\mathrm{nl}}/\kappa \approx 6$.

Notice that $\Sigma_\pm^{(\mathrm{res})}$ and $K_{0\mathrm{b}}$ strive to bend the membrane in the same direction. Hence, the *sign* of a membrane's residual differential stress conforms to what we would expect based on its spontaneous curvature. But its *magnitude* does not: it is smaller than the torque couple associated stress $\mp\kappa K_{0\mathrm{b}}/2z_0$ by the sizable factor $(1+\kappa_{\mathrm{nl}}/\kappa)$. This shows that the residual differential stress does *not* merely embody a bilayer's spontaneous materials curvature but instead reflects a more subtle balance between bending and stretching—as quantified by the difference between $K_0^\star$ and $K_{0\mathrm{s}}$. Notice in particular that it incorporates a specific choice of boundary- and initial conditions (namely: a simulation box and $K_{0\mathrm{s}} = 0$).

The first moment of the stress profile, the torque density $\mathcal{T}$ [115] can be calculated from the stress profile as:

$$\mathcal{T} = \int_{-\infty}^{+\infty} \mathrm{d}z \; \sigma_0(z) \, z \; , \tag{2.16}$$

which, in the absence of both net and differential stress, is connected to the bilayer's spontaneous materials curvature $K_{0\mathrm{b}}$ (see Eqn. (2.2)) [33, 115, 128, 150]:

$$\kappa K_{0\mathrm{b}} = -\mathcal{T} \qquad \text{if } \; \Sigma_\pm = 0 \; . \tag{2.17}$$

If we wanted to calculate $\kappa K_{0\mathrm{b}}$ as the first moment of the stress profile belonging to the area-matched membrane, using Eqns. (2.16) and (2.17), we encounter the slight complication that this system has differential stress and so Eqn. (2.17) does not strictly apply, as there are now *two* physical sources of spontaneous curvature. However, we can self-consistently correct for that. If we denote the actual stress profile by $\sigma(z)$ and assume that the residual stress $\Sigma_\pm^{(\mathrm{res})}$ acts approximately evenly over the thickness $d_{\mathrm{m}\pm}$ of each leaflet, then the profile with the residual differential stress removed is given by

$$\sigma_0(z) = \sigma(z) - \begin{cases} \Sigma_+^{(\mathrm{res})}/d_{\mathrm{m}+} & 0 < z < d_{\mathrm{m}+} \\ \\ \Sigma_-^{(\mathrm{res})}/d_{\mathrm{m}-} & d_{\mathrm{m}+} < z < 0 \end{cases} \; . \tag{2.18}$$

Combining this "de-stressing" correction with Eqns. (2.16), (2.17), and (2.15) then leads to

$$\Sigma_\pm^{(\mathrm{res})} = \pm \frac{\mathcal{T}}{2z_0(1 + \kappa_{\mathrm{nl}}/\kappa) + d/2} \approx \pm \frac{\mathcal{T}}{15.5 \, z_0} \; , \tag{2.19}$$

where the torque density $\mathcal{T}$ is the first moment of the *actual* stress profile $\sigma(z)$ (*i. e.*, the one that has a differential stress) and $d = d_{\mathrm{m}+} + d_{\mathrm{m}-}$ is the bilayer thickness. Also, since the neutral surface can typically be found one-third of the distance along the hydrocarbon chain from the polar head group [127], meaning $z_0 \approx \frac{2}{3} d_{\mathrm{m}}$, we estimated $d = 2d_{\mathrm{m}} \approx 3z_0$ in the last step. Had we alternatively assumed that the residual stress localizes at the neutral surface, and accordingly subtracted $\Sigma_\pm^{(\mathrm{res})} \delta(z \mp z_0)$ from each bare leaflet stress, the extra term "$+d/2$" in the denominator of Eqn. (2.19) would have been replaced by "$+z_0$", and the numerical value in the last expression then drops from 15.5 to 15. The precise functional form of the residual stress is dictated by the z-dependence of the area expansion moduli $K_{A,\mathrm{m}\pm}(z)$ [126], but our two limiting cases (entirely even vs. delta-localized) yield fairly similar results. In fact, the change with respect to Eqn. (2.15) is minor: simply replacing $\kappa K_{0\mathrm{b}}$ with $-\mathcal{T}$ gives an answer only about 10% too big. This is almost certainly less than the error incurred by empirical estimates such as $\kappa_{\mathrm{nl}}/\kappa \approx 6$ or $d = 3z_0$.

To test Eqns. (2.15) or (2.19), one would have to measure both the residual differential stress $\Sigma_\pm^{(\mathrm{res})}$ as well as either the spontaneous materials curvature $K_{0\mathrm{b}}$ or

the torque density $\mathcal{T}$. Luckily, all of these are reported—over a range of spontaneous bilayer curvatures—in a recent paper by Miettinen and Lipowsky [125]: For their "lollipop-like" model of GM1, their Fig. 5 shows that $\kappa K_{0\mathrm{b}} \approx 0.15\phi\,\mathrm{pN}$ for a membrane that contains a fraction ϕ of GM1 lipids only in its upper leaflet (hence giving the membrane a positive spontaneous curvature). Estimating $z_0 \approx 1.5\,\mathrm{nm}$ from their Fig. 1, our Eqn. (2.19) then predicts residual single leaflet tensions of $\Sigma_\pm^{(\mathrm{res})} \approx \mp 0.0065\phi\,\mathrm{mN/m}$, or a difference between these of $-0.013\phi\,\mathrm{mN/m}$. For comparison, their Fig. 3 reports about $-0.016\phi\,\mathrm{mN/m}$ for this difference, which agrees fairly well with our estimate.

A slightly different analysis regarding residual differential stress has been proposed in a recent, as of yet unpublished work by Pastor *et al.*, which we will summarize and discuss here. Pastor *et al.* argue that an asymmetric bilayer under periodic boundary conditions (PBC) is required to be flat, *i. e.*, have zero (mean) curvature, but does not necessarily have zero differential stress curvature $K_{0\mathrm{s}}$ (they also posit that residual differential stress $\Sigma_\pm^{(\mathrm{res})}$ as calculated via the measured stress profile should in fact be the required differential stress to force the bilayer to be flat, not its negative). From Eqn. (2.5) and Eqn. (2.10) the intrinsic differential stress of a curvature-relaxed asymmetric membrane would be

$$\Sigma_\pm^* = K_{A,\mathrm{m}\pm}\gamma_\pm(K_0^\star) \approx \pm K_{A,\mathrm{m}\pm}(K_0^\star - K_{0\mathrm{s}})z_0. \tag{2.20}$$

When the bilayer bends toward a different curvature K, the differential stress becomes $\Sigma_\pm(K)$, *i. e.*, an additional differential stress, $\Delta\Sigma_\pm(K) = \Sigma_\pm(K) - \Sigma_\pm^*$, to the intrinsic differential stress would be needed. The imposition of PBC sets $K = 0$ and thus, the required additional differential stress, which is the measured residual differential stress would be

$$\Sigma_\pm^{(\mathrm{res})} = \Sigma_\pm(K=0) - \Sigma_\pm^* \approx \mp\frac{\kappa_{\mathrm{nl}}K_0^\star}{2z_0} = \mp\frac{\kappa K_{0\mathrm{b}} + \kappa_{\mathrm{nl}}K_{0\mathrm{s}}}{2z_0(1+\kappa_{\mathrm{nl}}/\kappa)}. \tag{2.21}$$

For an area-balanced asymmetric bilayer ($K_{0\mathrm{s}} = 0$) it reduces to an expression that is larger by a factor of $\kappa_{\mathrm{nl}}/\kappa \approx 6$ compared to our result.

The torque density of stress-free monolayers can be written as

$$\mathcal{T}_\pm = \pm\int_0^{+\cdots} \mathrm{d}z\;\sigma_0(\pm z)\,z \;\; = -\kappa_{\mathrm{m}\pm}K_{\mathrm{m}\pm} \tag{2.22}$$

where the second equality is the analogue of Eqn. (2.17) for a monolayer. Removing residual stress from the observed stress profile, calculating the torque density, and using Eqn. (2.2) we get

$$\kappa_{\mathrm{m}+}K_{\mathrm{m}+} - \kappa_{\mathrm{m}-}K_{\mathrm{m}-} = -\mathcal{T} + \Sigma_+^{(\mathrm{res})}\frac{d}{2}. \tag{2.23}$$

Using Eqn. (2.22) this can be rearranged as

$$\Sigma_+^{(\mathrm{res})} = \frac{\mathcal{T} - (\mathcal{T}_+ - \mathcal{T}_-)}{d/2}. \tag{2.24}$$

We use data from our simulations of symmetric MARTINI DLPC and POPC bilayers and an area-balanced, asymmetric DLPC-POPC bilayer in 300 K to calculate torque densities and differential stress in Eqn. (2.24). We found $\mathcal{T} = 8.26(24)\,\mathrm{pN}$ for the torque density for the area-balanced DLPC-POPC bilayer, $\mathcal{T}_+ = -9.20(10)\,\mathrm{pN}$ and $\mathcal{T}_- = -3.93(11)\,\mathrm{pN}$ for torque density of stress-free monolayers of POPC and DLPC respectively, and we have $\Sigma_+^{(\mathrm{res})} = 5.68(8)\,\mathrm{mN/m}$. Using these values and Eqn. (2.24) we find the estimate for the value of bilayer thickness as $d \approx 2.4\,\mathrm{nm}$, which is reasonably close to typical values for thickness of a MARTINI bilayer.

While the line of argument from Pastor *et al.* seems more valid to us in hindsight, and their conclusions are supported by results from simulations accompanying their work, the relatively good agreement of results from simulations by Miettinen and Lipowsky [125] and our initial equation for residual stress is somewhat puzzling. Alas, we are unable to better resolve this confusing situation at this juncture.

2.4 Simulating asymmetric membranes

Using a more coarse-grained model reduces the computational load of our simulations, allowing us to reach length and time scales necessary for investigating phenomena of interest. Even when the use of a more fine-grained model is computationally feasible, however, it would still be preferable to utilize a model that is merely as detailed as necessary to capture the complexity of the physical phenomenon under consideration; This would enable us to find the physical essence of the connection between microscopic attributes of the constituent units of our system and its larger scale behavior in the clearest possible fashion. In the case of simulating asymmetric membranes, while many aspects of asymmetry, such as large scale shape deformations, do not depend on fine chemical details of the lipids, we need a model with high enough resolution to be able to represent a meaningful difference between membrane components.

A highly coarse-grained implicit solvent model that has been widely used to study bilayer elastic phenomena is the Cooke model [129,130], in which a lipid is represented by three beads: one acting as the headgroup and two representing the tail region. This strongly coarse grained lipid model has a significantly higher flip-flop rate compared to real systems, which would not be a problem if we were only interested in equilibrium properties. However, we need a model with a lower flip-flop rate in order to be able to study metastable but relatively long-lived states of bilayers with compositional or stress asymmetry. A four-bead version of the Cooke model with suppressed flip-flop rates has recently been introduced [131], but since this model was not available at the time of our research, we chose the MARTINI coarse grained model (1.3) to use in our simulations.

While the flip-flop rate for regular phospholipids in MARTINI model is low enough to let us adequately sample metastable asymmetric states of interest for systems

consisting these species, it also maintains the benefit of having a flip-flop rate for cholesterol that is orders of magnitude faster, therefore allowing us to investigate the important role of this abundant component of membranes.

Chapter 3

Differential stress induced stiffening transition

This chapter starts with descriptions of the methods for calculating various observables such as membrane rigidity and order parameters from simulations. This is followed by results from simulations describing the phenomenon of stiffening due to differential stress, and explanation for experiments measuring asymmetric vesicles rigidity based on this phenomenon. We then present results of simulations probing the effect of system parameters such as temperature and size on the stiffening transition, and finish the chapter by addressing the symmetry braking that occurs in asymmetric buckled membranes. A glossary containing definitions of some the symbols used in this chapter (and the rest of thesis) is available at the end of the thesis 7.

3.1 Methods

3.1.1 Buckling

The two most common methods for measuring the bending rigidity of lipid bilayers from simulations are fluctuation analysis [132–144] and buckling [73, 75, 148]. The former makes use of theories relating various elastic moduli to the power spectra of observables such as membrane undulation, lipid orientation fluctuation, and lipid tilt fluctuation.

Our attempt at finding the bending rigidity of asymmetrically stressed membranes using regular fluctuation analysis did not achieve the needed precision, which is why we chose to use the buckling method.

In this method, we set up an anisotropic cuboid simulation box with a dimension L_x along which we then buckle the membrane (Fig. 3.1 shows the schematic shape of a buckled surface). This length exceeds both the box and membrane width L_y (which is fixed, otherwise the fluid bilayer would expand in the y-direction and relax the

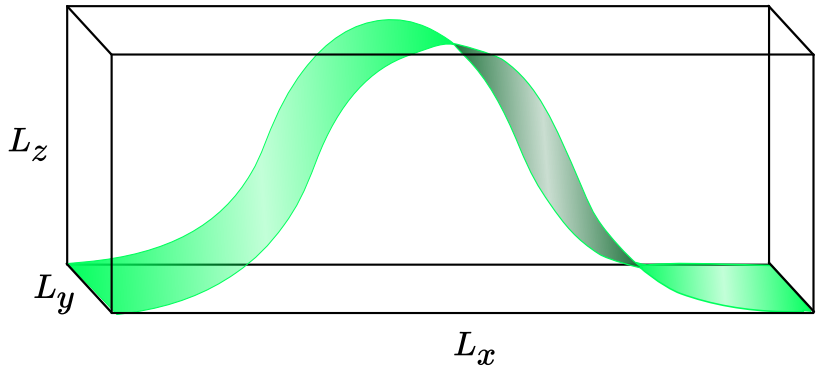

Figure 3.1: Schematic shape of a buckled surface.

pressure in the x-direction, flattening the buckle) as well as the box height L_z (which adjusts to the external pressure in order to maintain the constant pressure of the solvent) by a factor of around 6 (deemed appropriate based on previous experience with similar simulations). We first determine the zero-tension relaxed rest length L of the membrane by creating constant pressure conditions along the x-direction and measuring the corresponding expectation value of the box length: $L = \langle L_x \rangle_{\Sigma=0}$. We then buckle the membrane along x by imposing a fixed box-length $L_x < L$, which corresponds to a dimensionless buckling strain

$$\gamma = \frac{L - L_x}{L} \ . \tag{3.1}$$

The force $f_x(\gamma)$ per unit length along the x-direction (the so-called "stress-strain-relation") is measured from

$$f_x(\gamma) = \big[P_x(\gamma) - P_z\big] L_z \ , \tag{3.2}$$

where P_x and P_z are the pressure in the x and z-direction, respectively. Assuming quadratic curvature elasticity in accordance with the Helfrich Hamiltonian, $f_x(\gamma)$ can be expressed as a series expansion in γ [148]:

$$f_x(\gamma) = \kappa \left(\frac{2\pi}{L}\right)^2 \left\{1 + \frac{1}{2}\gamma + \frac{9}{32}\gamma^2 + \frac{21}{128}\gamma^3 + \cdots\right\} \ . \tag{3.3}$$

Here we have ignored negligible fluctuation corrections due to thermal membrane undulations. (While asymmetry between the leaflets by itself does not affect the validity of this equation for describing a bilayer, the potential effect of lateral hetrogeneity has been briefly addressed in Sec. 3.8.) Once membranes exhibit a sufficiently large stress-asymmetry between the leaflets, we found it necessary to extend this theory to permit for curvature softening, as previously used by Diggins *et al.* to quantitatively model the significant deviations from conventional curvature elasticity found in

gel-phase membranes [75]. Briefly, the quadratic curvature elastic energy density of $\frac{1}{2}\kappa K^2$ (where K is the total curvature, *i. e.* the sum of the two principal curvatures) is replaced by the softened expression

$$e(K) = \kappa\ell^{-2}\left[\sqrt{1+K^2\ell^2}-1\right] , \tag{3.4}$$

where the new material parameter ℓ is a cross-over length that indicates below which curvature radius softening sets in. This empirical functional has the properties that (*i*) it reduces to the original quadratic theory in the limit $\ell \to 0$; (*ii*) it has a negative quartic contribution $-\frac{1}{8}(\kappa\ell^2)K^4$ that promotes softening; and (*iii*) its post-quartic terms render the complete functional bounded below—in fact, convex. The modified stress-strain relation for Eqn. (3.4) is [75]

$$\begin{aligned} f_x(\gamma,\delta) =& \kappa\left(\frac{2\pi}{L}\right)^2\left\{1+\frac{1}{2}\Big(1-3\delta^2\Big)\gamma\right. \\ &+\frac{3}{32}\Big(3-14\delta^2+31\delta^4\Big)\gamma^2 \\ &\left.+\frac{1}{128}\Big(21-129\delta^2+447\delta^4-779\delta^6\Big)\gamma^3+\cdots\right\} , \end{aligned} \tag{3.5}$$

where $\delta = 2\pi\ell/L$ is a dimensionless smallness (or "softening") parameter: $\delta \to 0$ implies $\ell \to 0$ and reduces this more complicated expression to the simpler one from Eqn. (3.3). We always used Eqn. (3.5) to fit the stress-strain-relation measured in our simulations (using the parameters κ and δ); finding $\delta = 0$ within error bars indicates that the membrane exhibits conventional curvature elasticity. Eqn. (3.5) works well as long as the buckling strains are not too large. For larger γ values it becomes necessary to use more expansion terms (as calculated in [146]) to get reasonably accurate results.

The width-to-length ratio of the buckles was chosen such that L_y is small enough for the undulations along the y-direction to be negligible, and the relaxed length L is not too large, since a larger L leads to heightened fluctuations along the x-direction, as well as making the value of our "signal", the force f_x, more noisy. We also require that L is not too small, since ℓ is a size-independent materiel parameter and reducing L increases the softening parameter δ. Fig. 3.2 shows the stress-strain relation for a few select values of δ.

It is worth noting that, with hindsight about the emergence of macroscopic lateral elastic heterogeneities (see 3.5) in asymmetrically stressed membranes, it becomes more clear why the absence of a theory for the fluctuation spectrum in the presence of differential stress makes using that method unfeasible for the purpose of our work, while in a buckling analysis the emergence of stiffer domains can be dealt with more adequately, using ideas such as curvature softening. Some aspects of the effect of asymmetry on buckling analysis are examined more thoroughly in the coming sections.

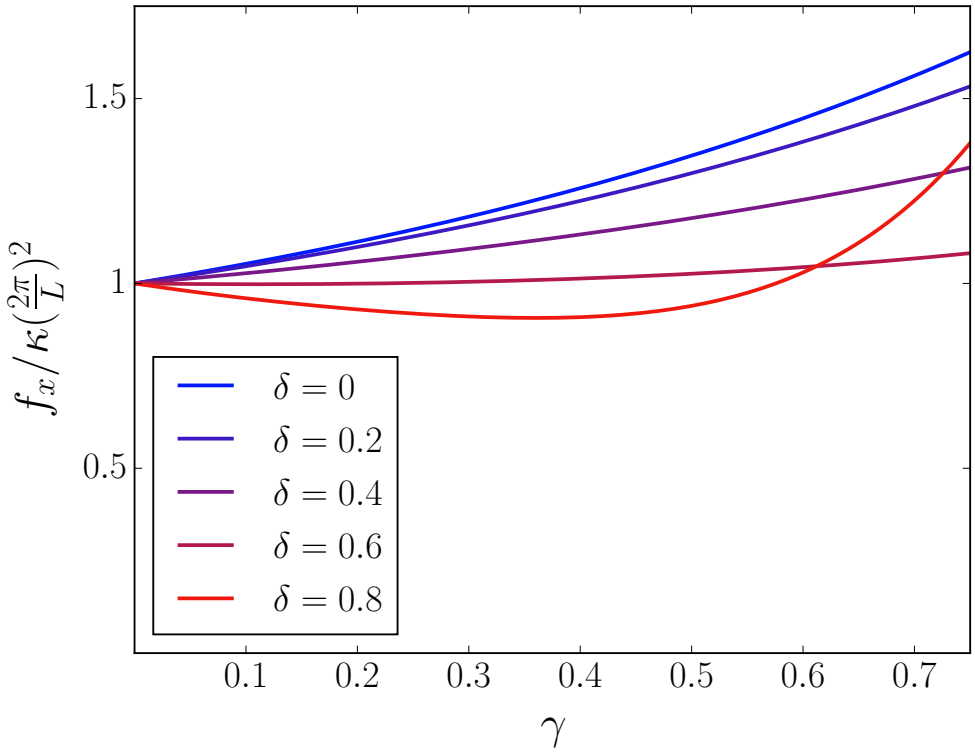

Figure 3.2: Force per unit length f_x as a function of buckling strain γ for different values of curvature softening parameter δ.

3.1.2 Stress profile

Using the GROMACS-LS package [43, 44] we can calculate the lateral stress profile $\sigma_0(z)$ of a bilayer spanned in the xy-plane. In our simulations we use the suggested sampling frequency by the package developers and repeat each simulation 20 times to be able to perform statistical abalysis on the results and determine error values.

This stress is defined as

$$\sigma_0(z) = P_{zz}(z) - \frac{1}{2}\big[P_{xx}(z) + P_{yy}(z)\big] \ , \tag{3.6}$$

where the $P_{ii}(z)$ are the diagonal components of the local pressure tensor in a thin slice at position z. For reasons of mechanical stability $P_{zz}(z)$ must actually be constant [149], which is a good first test for correctness and convergence. To avoid fluctuation blurring of $\sigma_0(z)$, it is best to simulate small membranes with only $\mathcal{O}(100)$ lipids [148].

The tension per leaflet, $\Sigma_\pm$, is the integral of $\sigma_0(z)$ over the respective leaflet, ranging from the bilayer midplane into the bulk water phase. Since $\sigma_0(z)$ rapidly decays to zero for z values outside the membrane, the precise location of the outer

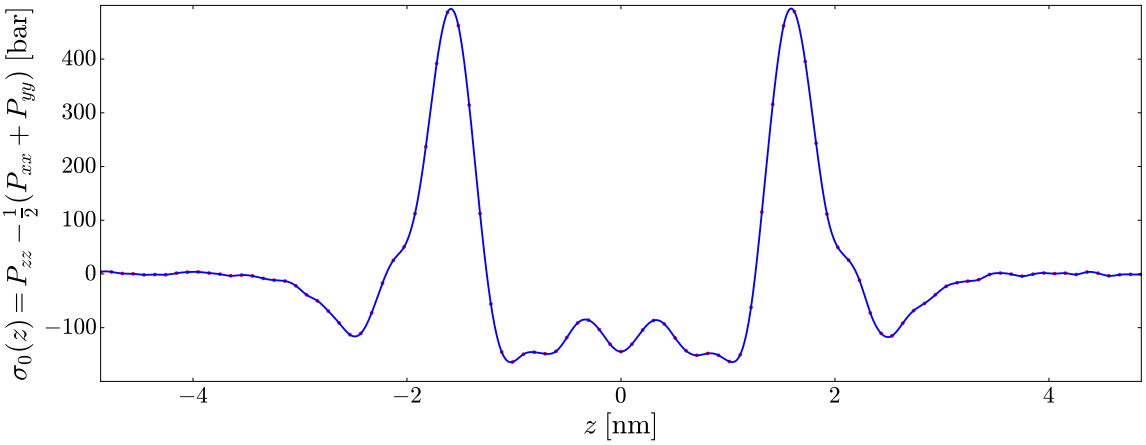

Figure 3.3: Stress profile of a POPC bilayer. $z = 0$ is the average position of the end beads of the lipids in the two leaflets. The red points are the discrete data points calculated by GROMACS-LS and the blue line a cubic spline to the data points.

boundary is immaterial, provided it is sufficiently far away from the membrane:

$$\Sigma_{\pm} = \int_0^{+\cdots} \mathrm{d}z \; \sigma_0(\pm z) \; , \tag{3.7}$$

where $z = 0$ marks the location of the midplane. Notice that for asymmetric membranes the latter need not coincide with the z-coordinate of the membrane's center of mass, which is the location to which GROMACS-LS shifts the membrane if one chooses to center it. We use the average z position of all tail beads as the location of the midplane. The integral itself can be easily done numerically by a Gaussian quadrature [153] of the local stresses calculated by GROMACS-LS for each individual z-bin.

Fig. 3.3 shows the calculated stress profile corresponding to a symmetric bilayer with 80 MARTINI POPC lipids in either leaflet. Notice the relatively large peak in lateral tension roughly at position of the lipid backbone where there is the equivalent of a hydrophilic-hydrophobic interface and the bilayer is being pulled together. Consequently, both the tails and the heads of the lipids are now being compressed, resulting in negative tension in the tail and upper head regions. If the membrane is not subject to a net lateral tension, the net total stress (the integral over $\sigma_0(z)$) vanishes. One might be surprised by the very large (hundreds of bars) values of the the stresses, but considering typical values for the oil-water surface tension ($\sim$ 50 mN/m) [151] and the fact that the hydrophilic to hydrophobic environment transition occurs over a region with $\sim$ 1 nm in width, the pressure we expect at the peak is indeed $\sim (50\,\mathrm{mN/m}) \div (1\,\mathrm{nm}) = 500\,\mathrm{bar}$ [152].

3.1.3 Order parameters

Order parameters are quantitative measures of local or global order. Here we introduce two such measures that were utilized in this project. Another order parameter that is commonly used in analyzing lipid bilayers is the lipid acyl chain order parameter S_{CH} which is calculated based on the angle between C-H bonds in the lipid tails and a reference surface [155, 156]. Given that we do not use atomistic models, this method of measuring order is not applicable to our simulation data.

Orientational order parameter

A standard measure for assessing the degree of lipid orientational order is the so-called P_2 order parameter. This quantity, which we only calculate for flat bilayers, is defined as

$$P_2 = \langle \mathrm{P}_2(\cos\vartheta_i)\rangle = \frac{1}{2}\left(3\left\langle\cos^2\vartheta_i\right\rangle - 1\right) \ , \tag{3.8}$$

where $\mathrm{P}_2(x)$ is the second Legendre polynomial, and ϑ_i is the angle between the orientation of a lipid i and the average membrane normal, which is the z-direction for our simulations. The average is taken over all lipids in a membrane, or all lipids in one of the leaflets. A MARTINI lipid's orientation is defined through the vector pointing from the midpoint between the two tail-endbeads to the choline head bead. Larger values of P_2 indicate stronger lipid alignment; $P_2 = 1$ indicates perfect alignment, $P_2 = 0$ signals completely random directions, and $P_2 = -\frac{1}{2}$ occurs when lipids align perpendicularly to the chosen axis.

Hexatic order parameter

The hexatic order parameter Ψ_6 of a two-dimensional planar collection of points (think of particle coordinates on a flat surface) measures the extent to which the points' positional distribution exhibits a local six-fold rotational symmetry. The value of the hexatic order parameter for a given particle k at position $\mathbf{r}_k$ is obtained by first calculating the complex local bond orientational parameter

$$\psi_6(\mathbf{r}_k) := \frac{1}{6}\sum_{l=1}^{6}\exp\{6\mathrm{i}\theta_{kl}\} \ , \tag{3.9}$$

where θ_{kl} is the angle which the direction between particles k and l makes with some arbitrarily defined direction (say, the x-axis), and the sum extends over the 6 nearest neighbors of particle k, which we can efficiently find using the routine `spatial.cKDTree` from SciPy [154]. The hexatic order parameter is then obtained by averaging the modulus of the bond orientational parameter,

$$\Psi_6 := \langle|\psi_6(\mathbf{r}_k)|\rangle \ , \tag{3.10}$$

where the average may be over the whole system, or over time, or over both—depending on whether one wishes Ψ_6 to be resolved in time or space.

Interestingly, calculating the hexatic order parameter of a membrane from the centers of mass (CMs) of lipids gives a very low value. Lipids do not sit on a particularly well defined triangular lattice. However, *individual lipid tails do*. Hence, for each lipid we define *two* points, the CMs for each of its two tails, and use these coordinates to calculate the hexatic order parameter.

We also use the hexatic order parameter to analyze order in non-flat bilayers. To calculate Ψ_6 for lipids in a buckled membrane, we proceed in three steps:

1. Construct the midsurface of the membrane, which we assume to have strict translational symmetry along the buckle's y-direction; in other words, it can be written as a function $h(x)$ that only depends on the horizontal coordinate x. This assumes the buckle does not have "overhangs", but we never employ strains large enough for that to happen. Each point on the midsurface has two coordinates (s, y), where s is the arc-length along the buckled surface (measured from some reference point) and y determines the position along the buckle's width.

2. Project the center of mass (CM) of each individual lipid tail onto the midsurface, which for each lipid yields the coordinate pair (s_k, y_k).

3. Calculate Ψ_6 from the resulting set of (intrinsically flat) $2d$ coordinates.

For the first step, we fit a cubic smoothing spline (using `interpolate.splrep` from the SciPy package [154], with an empirically determined smoothing parameter of $s = 10$) to the coordinate pairs (x, z) of the CMs of lipid tails, which gives us the function $h(x)$ describing the estimated midsurface of the leaflet. To ensure that the slope of the spline function matches that of a periodic buckle at the two box ends, we copy half a buckle and attach the data to either side of our box.

The second step involves the projection onto the curved surface $h(x)$. This is technically difficult, but fortunately it suffices to get a good approximate solution, exploiting the fact that the CMs of all lipid tails are already fairly close to the midsurface. If the Cartesian coordinates of a CM are (x, y, z), we first project them vertically down onto the midsurface, giving the first estimate $(x, y, h(x))$. This is not yet accurate enough, though, because the vertical distance between CM and surface is comparable to the distance between lipids, and hence comparable to the local length scale that affects the order parameter calculation. To work out the next order correction, we construct the tangent plane to the surface at the location x and project the coordinates of the CM onto that plane, instead of vertically down. Fig. 3.4 shows the geometry of approximately projecting a CM coordinate some distance away from the buckle onto the tangent plane erected at the CM's x-coordinate. We see that $s/(z - h(x)) = \cos\alpha$, $\Delta x/s = \sin\alpha$ and $h'(x) = \tan\alpha$. Using $\sin\alpha\,\cos\alpha = \tan\alpha/(1 + \tan^2\alpha)$, this yields

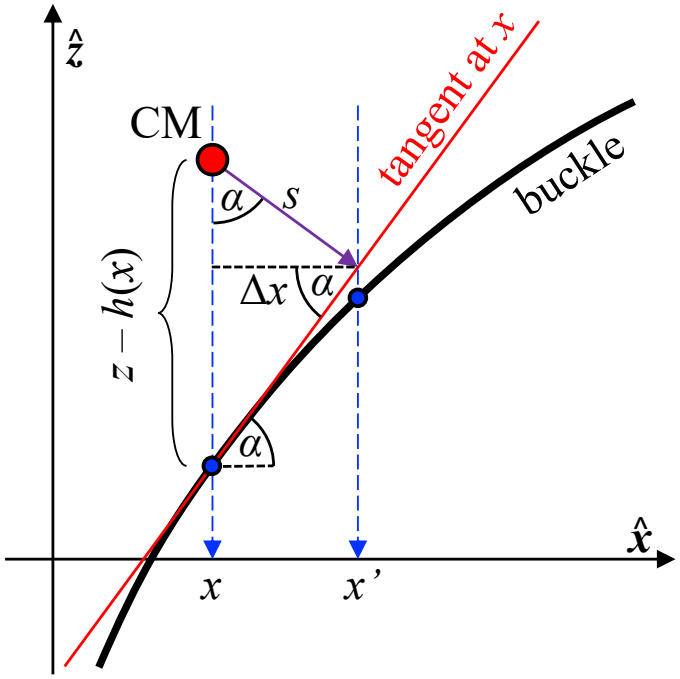

Figure 3.4: Projecting a point away from the buckle onto its surface.

the improved horizontal position

$$x' = x + \Delta x = x + \frac{h'(x)}{1 + [h'(x)]^2}\big[z - h(x)\big] \ . \tag{3.11}$$

Knowing $h(x)$, we find the arc length s corresponding to the horizontal position x' by numerically integrating

$$s(x') = \int_{x_0}^{x'} \mathrm{d}x \ \sqrt{1 + [h'(x)]^2} \ , \tag{3.12}$$

where x_0 is a pre-chosen reference point (e.g. the absolute minimum of the buckle).

The previous two steps have resulted in the two-dimensional coordinates $(s(x'_k), y_k)$ for the CMs of all lipid tails, from which the hexatic order parameter is then readily calculated using Eqn. (3.10).

3.1.4 Specific heat

We calculate the isobaric specific heat c_P for membranes (in the flat state) as a common means to probe for phase transitions. Recall that c_P is defined as the rate of change of enthalpy $H = E + PV$ with respect to temperature T at constant pressure P per total number of particles N, which in our case is the total number of beads:

$$c_P = \frac{1}{N}\Big(\frac{\partial H}{\partial T}\Big)_P \tag{3.13}$$

The classical fluctuation-response theorem teaches that c_P is proportional to the enthalpy fluctuations:

$$\frac{c_P}{k_\mathrm{B}} = \frac{\sigma_H^2}{N(k_\mathrm{B}T)^2} \ , \tag{3.14}$$

where $k_\mathrm{B}T$ is the Boltzmann constant and $\sigma_H^2 = \langle H^2 \rangle - \langle H \rangle^2$ is the variance of the enthalpy.

Two small comments are in order. First, even though we simulate our aqueous membrane systems at fixed pressure, their tiny compressibility renders the difference between the isobaric and isochoric specific heat negligible—we find $(c_P - c_V)/k_\mathrm{B} \sim \mathcal{O}(10^{-4})$. And second, it is well known that the Berendsen thermostat does not precisely reproduce the canonical ensemble, since it suppresses fluctuations in the kinetic energy [157]. For us this matters only insofar as the value of c_P calculated via Eqn. (3.14) will miss part of its kinetic contribution (we found it to be about $0.75\,k_\mathrm{B}$ too small). However, the impact on the configurational degrees of freedom vanishes like $1/N$, and so the thus calculated c_P is still an excellent indicator for phase transitions, which are driven by the potential contribution to the Hamiltonian.

3.1.5 Simulation details

We employed GROMACS 5.1 [158] and GROMACS 2018.1 for our simulations. We used a time step of $\delta t = 20\,\mathrm{fs}$ and a 1.4 nm Verlet cutoff neighbor list updated every 10 steps. Cutoffs for Lennard-Jones and Coulomb interactions were set to 1.2 nm, and the relative dielectric constant was set to $\epsilon_\mathrm{r} = 15$. A Berendsen thermostat [159] was used with a time constant $\tau_T = 1\,\mathrm{ps}$ to fix the simulation temperature. If we needed constant pressure conditions along some coordinate direction i, we used a Berendsen barostat [159] with reference pressure $P_i = 1\,\mathrm{bar}$, time constant $\tau_P = 3\,\mathrm{ps}$, and isothermal compressibility $\kappa_T = 3 \times 10^{-5}\,\mathrm{Pa}$.

There are two points worth elaborating regarding our choices for simulation parameters: The first point involves the use of a Berendsen thermostat and barostat. These algorithms do not reproduce the correct thermodynamic ensemble, but their use was still relatively common at the time of the start of this project. Berendsen algorithms suppress fluctuations in kinetic degrees of freedom [157], while their impact on configurational degrees of freedom rapidly vanishes for systems consisting of $N \sim 100$ or higher particles, and thus their effect on phase behaviour of the systems, which is what we are interested in and which is driven by potential contributions, is insignificant. While we did not expect major changes for quantities that do not explicitly analyze fluctuations, we checked the robustness of our results by performing control simulations using the Parinello-Rahman barostat and the velocity-rescale thermostat, which lead to qualitatively and quantitatively similar results. The other point is related to the fact that the rigidity for MARTINI DLPC determined in our work is almost $6\,k_\mathrm{B}T$ (or 20%) larger than the rigidity for MARTINI DMPC in Ref. [148]. While the relevant bead-parameters of the DLPC lipid in the updated

Table 3.1: Simulated systems and results for measured observables. Buckle length L, number of lipids in overfilled ($N_>$) and underfilled ($N_<$) leaflet, asymmetry, lipid order parameter in overfilled ($P_{2,<}$) and underfilled ($P_{2,>}$) leaflet, tension Σ_+ in the upper leaflet, bending rigidity κ, cross-over length ℓ in the curvature-softened energy density (3.4) and corresponding softening parameter $\delta = 2\pi\ell/L$. In all simulations the box width is $L_y = 8\,\mathrm{nm}$.

leaflets	L [nm]	$N_>/N_<$	δn [%]	c_p/k_B	$P_{2,>}$	$P_{2,<}$	Σ_+ [mN/m]	κ [$k_\mathrm{B}T$]	ℓ [nm]
DLPC/DLPC	41.39 ± 0.02	580/580	0	0.85 ± 0.02	0.699(1)	0.699(1)	0.07 ± 0.07	34.8 ± 1.1	2.0 ± 0.8
POPC/POPC	45.03 ± 0.02	580/580	0	n.d.	n.d.	n.d.	0.03 ± 0.07	34.4 ± 1.3	2.6 ± 0.9
DLPC/POPC	40.60 ± 0.03	568/522	4.22	n.d.	n.d.	n.d.	-5.68 ± 0.08	34.1 ± 0.9	1.7 ± 0.7
DLPC/POPC	40.02 ± 0.01	540/530	0.93	n.d.	n.d.	n.d.	-0.03 ± 0.06	32.9 ± 0.4	1.1 ± 0.4
DLPC/DLPC	39.50 ± 0.01	580/552	2.47	0.84 ± 0.01	0.715(1)	0.683(1)	-5.64 ± 0.08	33.6 ± 0.7	1.5 ± 0.7
DLPC/DLPC	40.17 ± 0.01	580/544	3.20	0.83 ± 0.01	0.718(1)	0.678(1)	-6.97 ± 0.07	34.5 ± 0.7	2.0 ± 0.5
DLPC/DLPC	39.91 ± 0.01	580/536	3.94	0.84 ± 0.01	0.722(1)	0.672(1)	-8.46 ± 0.08	44.1 ± 0.3	6.7 ± 0.2
DLPC/DLPC	39.50 ± 0.01	580/522	5.26	0.87 ± 0.01	0.729(1)	0.663(1)	-11.18 ± 0.09	47.0 ± 0.5	5.5 ± 0.1
DLPC/DLPC	37.38 ± 0.21	580/515	5.94	8.68 ± 4.63	0.765(6)	0.686(5)	-12.59 ± 0.06	47.0 ± 0.8	5.4 ± 0.1
DLPC/DLPC	33.93 ± 0.10	580/463	11.22	1.23 ± 0.31	0.853(1)	0.625(1)	-13.93 ± 0.09	50.2 ± 0.6	4.6 ± 0.1

martini_2.1 force field (used in our simulations) is identical to the DMPC lipid in the martini_2.0 forcefield (used in Ref. [148]), we used a cutoff value for Coulomb and for Lennard-Jones interaction that is longer than the recommended value of 1.1 nm for simulations using a Verlet neighbor list [160]. This will have implications on the order parameter, gel-phase transition temperature, and the elastic moduli. However, since we do not need absolute numbers and do not compare to experimentally measured bending rigidities or gel transition temperatures, this discrepancy does not affect our conclusions.

3.2 The stiffening transition

We begin by measuring the bending rigidity κ of symmetric DLPC and POPC bilayers that are tensionless and hence, due to their symmetry, also free of differential stress. Our results indicate that both membranes have basically the same value of κ within error bars ($34.8 \pm 1.1\,k_\mathrm{B}T$ and $34.4 \pm 1.3\,k_\mathrm{B}T$ respectively) and show only weak (albeit statistically significant) signs of curvature softening (with curvature softenning parameter δ of 0.05(2) and 0.06(2) respectively). See Tab. 3.1 for all measurement results. GROMACS 5.1 was used for simulations discussed in this section.

Next, we investigate an asymmetric membrane in which one leaflet is pure DLPC and the other one pure POPC and first choose the specific lipid areas in each leaflet to match those in simulations of their cognate symmetric tensionless system (DLPC: $a_\ell = 0.5709(3)\,\mathrm{nm}^2$; POPC: $a_\ell = 0.6212(3)\,\mathrm{nm}^2$). This results in a quite sizable residual differential tension $\Sigma_\mathrm{DLPC} \approx -5.7\,\mathrm{mN/m}$ that puts the DLPC leaflet under compression. Nevertheless, the resulting asymmetric membrane has a bending rigidity of $34.1(9)\,k_\mathrm{B}T$ that does not differ statistically significantly from the two pure cases ($34.8(11)\,k_\mathrm{B}T$ and $34.4(13)\,k_\mathrm{B}T$, for pure DLPC and POPC respectively) and (more generally relevant) from their average. To test whether the sizable differential stress creates any artifacts, we also performed a simulation for a system in which this stress

was relaxed by reducing the overabundance of DLPC lipids, resulting in a system with the differential stress $\Sigma_{\mathrm{DLPC},0} \approx -0.03(6)\,\mathrm{mN/m}$. We found its curvature rigidity to be $\kappa = 32.9(4)\,k_\mathrm{B}T$, which again agrees with the pure systems within statistics.

Having investigated stress-free compositional asymmetry, we now explore the opposite case: a compositionally symmetric DLPC membrane in which the number of lipids differs between the two leaflets, thus rendering them stress-wise asymmetric. As a measure of number asymmetry we use the relative excess δn, defined as

$$\delta n := \frac{N_> - N_<}{N_> + N_<} \,, \tag{3.15}$$

where $N_>$ and $N_<$ are the number of lipids in the more or less populated leaflet, respectively. This measures the percentage by which each leaflet is over- or underfilled compared to the balanced average.

Our simulation results, summarized in Tab. 3.1 and illustrated in Fig. 3.5, show that for an asymmetry up to about $\delta n = 3.2\%$ the rigidity does not significantly differ from that of a stress-balanced bilayer, nor does it show any more curvature softening. (Observe that the differential stress at that point, about $\pm 8\,\mathrm{mN/m}$, is larger than the stress of our asymmetric area balanced DLPC-POPC system.) However, for larger lipid number asymmetry there is a noticeable and sudden rise of κ, which increases by almost 50% at the largest asymmetry we tested, $\delta n = 11.2\%$. Near the transition, the fit to Eqn. (3.5), which is nonlinear in the curvature softening parameter δ, exhibits metastable minima (indicated as open symbols in Fig. 3.5). Together with the stable solutions, they support the scenario of a discontinuous stiffening transition, as illustrated by the drawn curve (an empirical guide to the eye, for which we have no descriptive theory). This transition is accompanied by a significant (and equally abrupt) increase in curvature softening, *i. e.* a jump to larger values of δ, leading to a length ℓ that is comparable to bilayer thickness, about 2.5 times larger than in the stress-balanced case. Remarkably, the sudden increase in curvature rigidity is *not* accompanied by jumps in the lipid order parameters $P_{2,>}$ and $P_{2,<}$ in the over- and under-filled leaflets, respectively. Instead, $P_{2,>}$ increases continuously (but slowly) up to about 5% asymmetry, while $P_{2,<}$ decreases by a comparable amount. Only at around 6% do these order parameters change more dramatically. The latter is driven by the gel transition, which is easily recognized by its strong signal in the specific heat, see Fig. 3.5a. However, by then the bilayer stiffening transition has long since happened.

3.2.1 Compositional asymmetry alone does not stiffen membranes

We find that a compositionally asymmetric DLPC-POPC membrane with sufficiently small differential stress is no stiffer than (the average of) its two symmetric counterparts, DLPC-DLPC and POPC-POPC. Granted, a single example for the absence

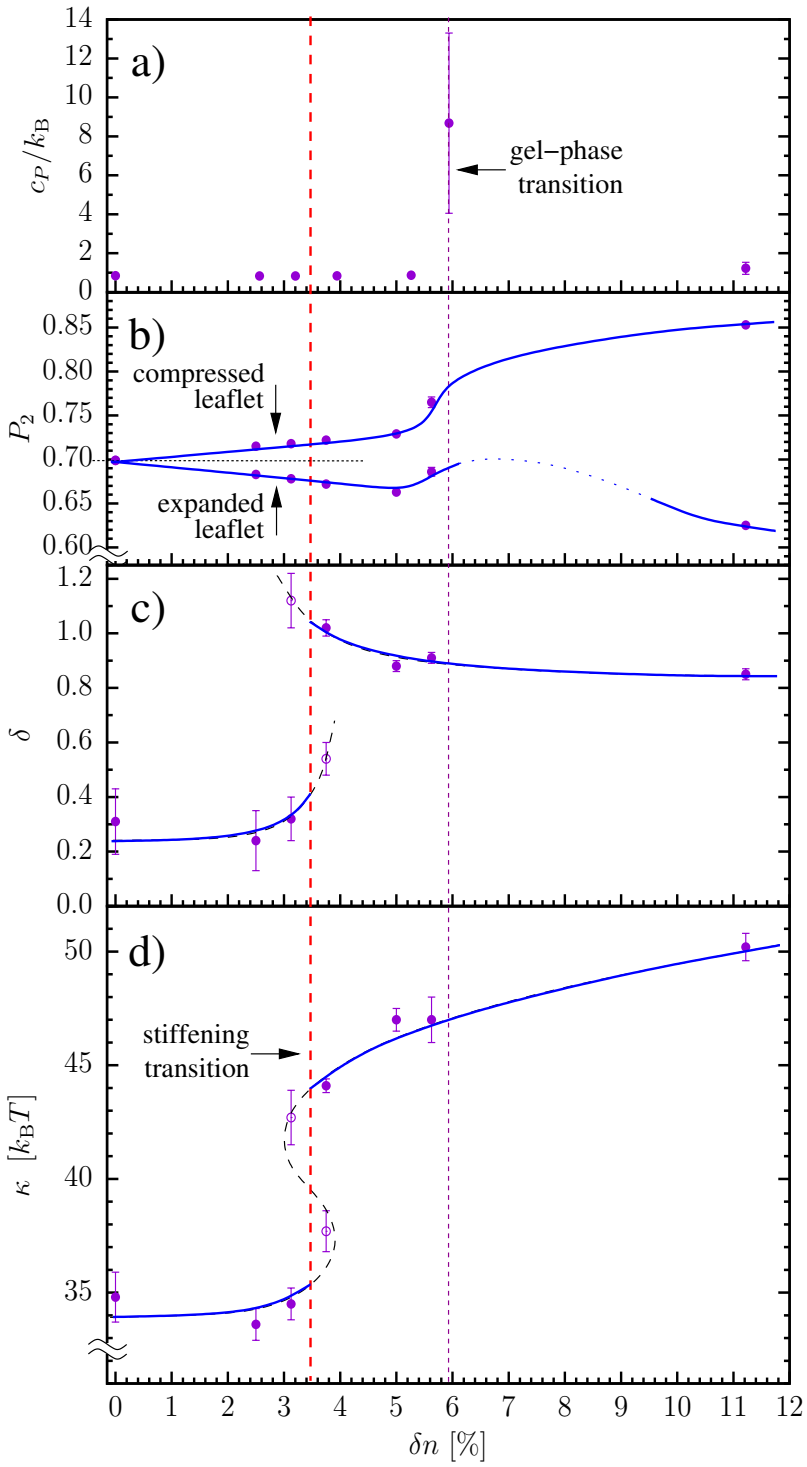

Figure 3.5: Several observables of differentially stressed MARTINI DLPC membranes as a function of asymmetry δn. Open symbols denote metastable states in the nonlinear fit; curves are guides to the eye. a) specific heat; b) orientational order parameter P_2; c) softening parameter δ; d) curvature modulus κ. The red vertical dashed line suggests the approximate location of the stiffening transition, the magenta dotted line suggests the location at which the compressed leaflet transitions into the gel phase.

of stiffening does not rule it out for all conceivable cases. But it must be recalled that this is the expected outcome: as long as the two leaflets can freely slide, and their individual structure matches that of their symmetric bilayer counterparts, basic elasticity considerations demand that leaflet rigidities simply add. Hence, the burden of proof lies with any claim of stiffening, and our particular negative result merely establishes the expected baseline.

One might worry that our two lipids were elastically too similar to begin with, but the experimentally observed increase in bending modulus (factor ~ 2.5, or about 150% stiffer) is much bigger than the disparity between the moduli of the two individual lipids (factor ~ 1.3, or about 30% stiffer) [84, 90], and so it is unlikely that this is a major factor. In contrast, the two leaflets might influence each other more directly via their free energy of adhesion, which depends on their area per lipid. Since our two coarse-garined lipids differ by about 9% in that regard, this effect would be even slightly bigger than what the experimental difference between the lipids used in the stiffening studies [84, 90] (POPC and DOPC) would be—with DOPC having an area about 6% larger ($68.3 \pm 1.5\,\text{Å}^2$ and $72.4 \pm 0.5\,\text{Å}^2$ respectively), when measured by the same technique [164].

3.2.2 Differential stress can stiffen membranes

What we instead find is that differential stress, if large enough, increases a bilayer's curvature modulus. Before addressing the origin of this effect, let us first rule out an incorrect attempt at a geometric explanation: could it be that the buckle of a differentially stressed membrane assumes some potentially asymmetric shape that strains the leaflets differently, thereby giving rise to a nonzero additional *stretching* contribution to the overall energy? The answer is no, because buckling does not globally strain the leaflets at all. To see why, let us calculate the membrane area $A_\pm$ of the upper and lower leaflet (taken for instance at their neutral surfaces $\pm z_\pm$), using the parallel surface theorem [103, 104]:

$$A_\pm = \int \mathrm{d}A \left\{1 \pm z_\pm K + z_\pm^2 K_\mathrm{G}\right\} \tag{3.16a}$$

$$= A_\mathrm{mid} \pm z_\pm \int \mathrm{d}A\; K + z_\pm^2 \int \mathrm{d}A\; K_\mathrm{G}\;, \tag{3.16b}$$

where the integral is taken over the buckle's midplane, which has area A_mid, and where K_G is the Gaussian curvature. By the Gauss-Bonnet theorem [104], the integral over K_G is a topological invariant and hence coincides with its value for the unbuckled membrane, for which $K_\mathrm{G} = 0$; hence this term vanishes. And the integral over K can be rewritten to an excellent approximation by assuming that the buckle only significantly curves *along* the buckling direction, not perpendicularly to it. This is ensured in simulations by making the transverse direction L_y much smaller than the buckle's length L, with L_y being about 6 times smaller than L in our simulations,

Since the buckling threshold scales inversely with the square of the buckle's length, see Eqns. (3.3) or (3.5), the force at which the y-direction would buckle is bigger than the membrane's x-buckling threshold by a factor of $(L/L_y)^2$. It is hence easy to ensure that the membrane will be flat along the y-direction. Therefore, we can describe the buckle by a single function $\psi(s)$, the angle against the horizontal as a function of arc length s. The curvature can then be expressed as $K = -\partial\psi(s)/\partial s$, and so we can simplify Eqn. (3.16b) to

$$A_\pm = A_{\text{mid}} \mp z_\pm L_y \int_0^L \mathrm{d}s \, \frac{\partial\psi(s)}{\partial s} \tag{3.16c}$$

$$= A_{\text{mid}} \mp z_\pm L_y \left[\psi(L) - \psi(0)\right] \tag{3.16d}$$

$$= A_{\text{mid}} \ , \tag{3.16e}$$

where in the last step we exploited periodic boundary conditions: $\psi(0) = \psi(L)$. We hence see that in fact *any* leaflet reference surface (not just the neutral surface) keeps its area when buckled under periodic boundary conditions. Notice that this does not even require the buckle's geometry to be the solution of some shape equation; *any* shape will do. The two additions in Eqn. (3.16b) both vanish identically—for (different) *topological* reasons. Evidently, this same argument also shows that the buckling protocol is insensitive to the spontaneous bilayer curvature: this only contributes a linear term in K to the energy density, which then vanishes under periodic boundary conditions.

3.2.3 Stressed leaflets differ elastically from unstressed ones

While our simulations clearly show that differential stress can stiffen a bilayer, the data by themselves do not yet offer an explanation for this observation. However, based on our collective findings, our hypothesis is that a stress-induced change in the elastic properties of the individual leaflets lies at the heart of the phenomenon. Recall that a major puzzle of the experimental results was the apparent "lack of additivity" [84]: the rigidity of an asymmetric membrane is not the average of the corresponding two symmetric parent membranes. And yet, our own theoretical analysis always assumed additivity—see Eqns. (2.1) and (2.6a). This is no contradiction, though, because the differential stress generally present in asymmetric bilayers puts each of their leaflets into a thermodynamic state that differs from its counterpart in a stress-free symmetric bilayer. This of course also affects the leaflet rigidities, but it is unfortunately difficult to anticipate the magnitude of this change from measurements performed on symmetric membranes: the higher lipid density in the compressed leaflet cannot be recreated by laterally compressing a symmetric membrane, since it would relax the area strain via buckling; and while the lower lipid density in the expanded leaflet can in principle be produced by applying tension to a symmetric membrane, it is then difficult to measure its rigidity (for instance because tension would strongly

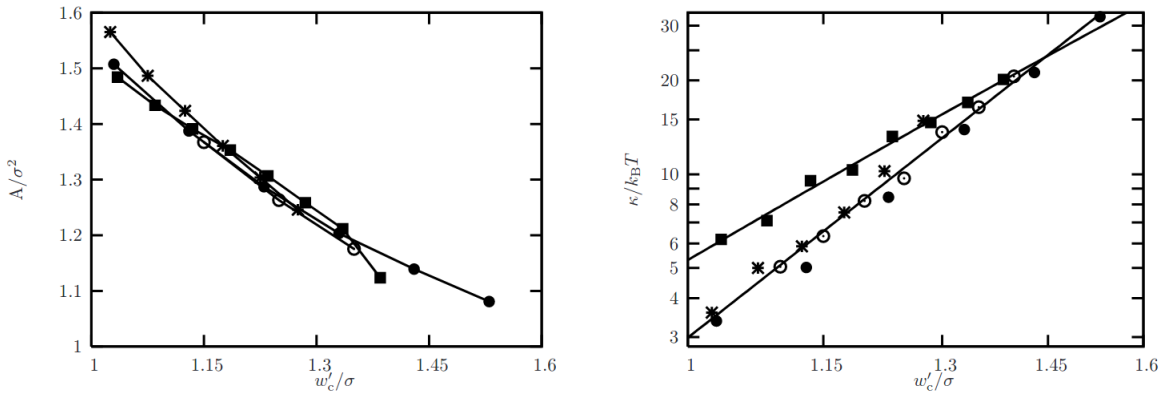

Figure 3.6: Area per lipid (left) and bending rigidity (right) of Cooke lipid bilayers for different temperatures as a function of w_c', a measure of attractive interaction strength. Figure reproduced from Ref. [129].

suppress bending modes in a flicker spectroscopy experiment). This observation shows that additivity might well hold, but *we do not know what leaflet-rigidities we actually have to add.*

Nevertheless, it seems highly plausible that, all else being equal, membranes with a smaller area per lipid are stiffer than those with a larger one. But if this dependency were linear, then it would cancel in a differentially stressed membrane, in which to a very good approximation the area strains are simply opposite in sign. However, there are good reasons to believe that *for dense systems* the relation is not linear. Recall that for an ideal gas the isothermal bulk modulus $K_T = -V(\partial P/\partial V)_T$ is proportional to the density, but in the liquid phase of a van der Waals gas it grows much more strongly with density (in fact, it diverges at the maximal "close-packing" density). The same physics reappears in fluid lipid bilayers: polymer brush theory [114] shows that the lateral leaflet pressure Π is proportional to $1/a_\ell^3$, where a_ℓ is the specific lipid area; hence $K_A = -a_\ell(\partial\Pi/\partial a_\ell)_T = 3\Pi$ shows the same strong increase with compression.

In simulations, a clean way to reduce the area per lipid is to artificially increase the cohesive energy between lipids. This can be done quite easily in coarse-grained lipid models in which this cohesion is one of the few tuning parameters. For instance, doing exactly this in the coarse-grained Cooke model [129, 130, 161] shows that the curvature rigidity of fluid Cooke-membranes scales approximately *exponentially* with the lipid area density (Fig. 3.6 shows how strengthening the attractive potential in the Cooke model increases bending rigidity linearly while it decreases area per lipid exponentially). Hence, the stiffening of the compressed leaflet overwhelms the softening of the expanded one, leading to an overall rigidity increase of differentially stressed membranes.

3.2.4 The link between stiffening and the gel transition

That a bilayer's curvature rigidity strongly increases with lipid density is particularly vivid in gel phase membranes, whose lipid density is typically about 30% higher than that of fluid phases, but whose rigidity is easily an order of magnitude larger [163,165, 166]. Curiously, gel phases also exhibit *much* stronger curvature softening than fluid phases ($\ell \approx 14\,\mathrm{nm}$ for MARTINI DMPC [75]); in fact, the modified curvature energy density in Eqn. (3.4) that allows for softening, together with its stress-strain relation (3.5), was originally developed by Diggins *et al.* to describe gel phases [75]. These authors also noticed that for coarse-grained models (such as MARTINI) $\kappa_{\mathrm{gel}}/\kappa_{\mathrm{fluid}}$ is not quite as large as seen in experiments—provided both phases are extrapolated to the transition temperature [162]. This mirrors our finding that the rigidity increase driven by differential stress (about 50%) is likewise not as large as the one that is experimentally observed (about 150%). Considering that coarse-grained models are typically designed to get the properties of fluid phases right, this discrepancy is not overly disturbing.

While the increase in membrane rigidity upon entering the gel phase is well established, our data nevertheless shows the stiffening transition does not coincide with a complete conversion of the compressed leaflet into gel phase. However, we can visually identify small transient gel regions in the compressed leaflet after the stiffening transition. These patches appear to prefer the vicinity of a buckle's inflection points, not its turning points. A more in-depth look at the microscopic description of the transition is presented in 3.5.

If transient gel or gel-like domains prefer the vicinity of inflection points, this would bias a buckle's shape to be flatter in these regions than expected for classical Euler elastica. Diggins *et al.* [75] captured precisely this feature in their curvature-softened buckling theory, where it shows up as an increase in ℓ or δ. This still leaves open the question whether in the present case it arises as a consequence of a "biphasic" membrane (as just described), or a "monophasic" membrane comprising a material with a fairly nonlinear elastic response (as Diggins *et al.* [75] concluded for pure gel phases). In Sec. 3.5 we use an analysis based on hexatic order parameter of lipid tails to shed more light onto this question. All the same, any flattening of the buckle near its inflection points (irrespective of the cause), and the associated non-Eulerian stress-strain response, prevents the fit from misreading the still soft turning points (or "hinges") as being representative of the entire membrane's rigidity.

Even more fundamentally, how a single-leaflet gel transitions takes place in such strongly differentially stressed bilayers is likely very subtle due to the competition between the two leaflets: upon increasing the asymmetry, the depleted one ever more strongly tries to compress the overfilled one, until the latter finally gives in; but when that happens, the concomitant reduction in area of the depleted leaflet also reduces its driving force for this very transition. In other words, it is not sufficient to picture the gel transition of the compressed leaflet as being driven by a fixed imposed stress. A more refined analysis of this scenario will be presented in chapter 5.

3.2.5 Localizing the stiffening transition

In this section we elaborate more on how we calculate the values for bending rigidity κ and the curvature softening parameter δ from our simulation data, and explain the method we use to identify the asymmetry value at which the stiffening transition happens.

The stress strain relation depends parametrically on the curvature rigidity κ and the curvature softening parameter δ. It is linear in the former, but nonlinear in the latter. In our analysis, we scan the value of δ and do a linear regression on κ, which leads to a δ-dependent value of κ as well as the fit's reduced chi-squared,

$$\chi^2_\nu(\delta) := \min_\kappa \frac{1}{\nu} \sum_{i=1}^{N} \left(\frac{f_{x,i} - f_x(\gamma_i; \{\kappa, \delta\})}{\delta f_{x,i}} \right)^2 , \tag{3.17}$$

where $f_{x,i}$ and $\delta f_{x,i}$ are the stresses and their uncertainties measured at the N strains γ_i, and ν is the number of degrees of freedom, equal to the number of observations minus the number of fitting parameters, amounting to $N - 1$ in this case.

Since the regression of the stress-strain relation is nonlinear in δ, it can lead to multiple solutions that (at least locally) minimize the chi-squared. This is illustrated in Fig. 3.7. Typically, $\chi^2_\nu(\delta)$ has two minima: one at a low value of δ and a low corresponding κ (*i. e.*, a "normal" membrane with hardly any curvature softening) and one at a larger value of δ and an elevated κ (*i. e.*, a stiffened membrane that noticeably softens upon bending). For low enough asymmetry δn, the $\chi^2_\nu(\delta)$ minimum at small δ is the global minimum, but as δn increases, the curvature-softened minimum drops down, until it becomes the global minimum, leading to a discontinuous transition into a stiffened state.

We define the stiffening transition to be the point where these two minima have the same height. But instead of monitoring where the height difference vanishes, we found it more consistent when comparing different δn to look at the asymmetry at which the ratio becomes one. The reason is that the overall quality of the fit (and hence magnitude of χ^2_ν) depends on the system under study: for systems close to the stiffening transition the fit works less well (because of transient ordered domains, as we will explain in Sec. 3.5), and so the χ^2_ν values are large for either δ; in contrast, away from the transition the fits work much better and the χ^2_ν values are small. To compare the $\delta_\pm$ values across different δn, we found it advantageous to consider the ratio of χ^2_ν values, for which the disparity in fitting quality cancels out. We hence define the stiffening transition to happen when

$$r(\delta n) := \frac{\chi^2_\nu(\delta_+)}{\chi^2_\nu(\delta_-)} \simeq 1 , \tag{3.18}$$

where δ_- and δ_+ are the smaller and larger δ-values, both calculated for a system at asymmetry δn.

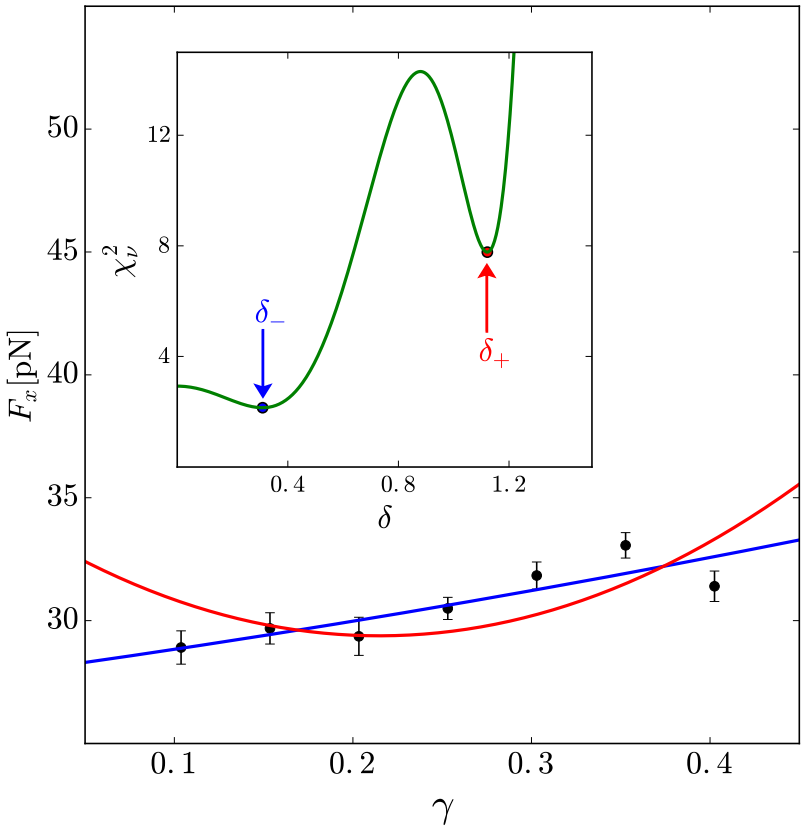

Figure 3.7: Measured buckling force $F_x = L_y f_x$ as a function of buckling strain γ, together with two fits of the stress strain relation from Eqn. (3.5), for the case of MARTINI DLPC at $T = 300\,\mathrm{K}$ and $\delta n = 3.20\%$. The two different fits correspond to the two minima of the reduced χ^2_ν as a function of softening parameter δ (see inset): a global one (at δ_-, blue) and a local one (at δ_+, red).

Since these simulations are computationally expensive (for each system and each value of δn, a number of buckles with different values of γ need to be simulated), it is not practical to produce many data points in the vicinity of δn_c to pin down its precise value. We instead estimate it by linearly extrapolating from the two asymmetries δn_1 and δn_2 nearest to 1, according to

$$\delta n_c = \delta n_1 + \frac{1 - r(\delta n_1)}{r(\delta n_2) - r(\delta n_1)} (\delta n_2 - \delta n_1) \ . \tag{3.19}$$

We can estimate the error by bootstrapping the stress-strain fits for the two asymmetries, which gives the uncertainties on the ratios $r(\delta n_i)$, from which we get the uncertainty of the extrapolation by an error propagation on Eqn. (3.19). Fig. 3.8 shows the χ^2_ν as a function of δ for the two closest simulations to the transition, with error estimates in the second and third columns, and the line extrapolating to find

the critical δn in the first column, for MARTINI DLPC bilayers simulated at four different temperatures.

3.2.6 Stress-strain plots

Fig. 3.9 shows the plots of buckling force $F_x = L_y f_x$ as a function of buckling strain γ, together with fit(s) of the stress strain relation for MARTINI DLPC at $T = 300\,\mathrm{K}$ and various values of δ. The inset of the plots shows the reduced χ^2_ν as a function of softening parameter δ. It can be clearly seen how increasing the asymmetry gradually makes the fit with the higher value of the stiffening parameter δ become more stable until the minimum associated with it in the χ^2_ν graph passes the minimum with the smaller stiffening parameter as the the asymmetry crosses the critical threshold.

3.3 Revisiting experiments

The experimental results of Elani *et al.* [84] suggest that compositionally asymmetric membranes are more rigid than their symmetric counterparts, while we instead argue that differential stress lies at the core of stiffening. But Elani *et al.* did not aim for differential stress; they expressly aimed for compositional asymmetry, and this is what the phase transfer protocol is supposed to produce. Moreover, Elani *et al.* were quite conscious of the possibility that the phase transfer protocol might generate undesired artifacts, and so they devised a control experiment in which they created *symmetric* membranes via the more elaborate layer-by-layer process—finding them to be elastically indistinguishable from symmetric membranes made by conventional electroformation. To explain why this negative outcome does not exclude the possibility of differential stress, we now discuss a scenario in which asymmetry is in fact a *prerequisite* for the phase transfer protocol to engender differential stress.

Consider, therefore, a compositionally asymmetric bilayer vesicle that is built by joining two individual leaflets, each initially present as a monolayer at an oil water interface [82, 83, 87, 89, 93, 97]. We will assume that the area per lipid in these monolayers is determined by some equilibrium condition (say, the equilibrium spreading pressure set by the chemical potential of lipids in the oil phase) and given by $a_{\mathrm{s}j}$ (where $j \in \{+,-\}$ labels the leaflets). The vesicle's initial area is then given by $A_\mathrm{i} = N_j a_{\mathrm{s}j}$ (for both j). The crucial point is that the monolayer areas per lipid need not coincide with those in a stress-free leaflet of a lipid bilayer, a_{0j}, and therefore each leaflet harbors energy due to tangential stress, given by

$$E_\mathrm{stretch} = \frac{1}{2} K_{A,\mathrm{m}+} \frac{(A_\mathrm{i} - N_+ a_{0+})^2}{N_+ a_{0+}} + \frac{1}{2} K_{A,\mathrm{m}-} \frac{(A_\mathrm{i} - N_- a_{0-})^2}{N_- a_{0-}} \,. \tag{3.20}$$

The vesicle can lower this energy, and hence eliminate the *net stress* Σ, by changing its initial area A_i to some final area A_f. The energy minimization condition $\Sigma =$

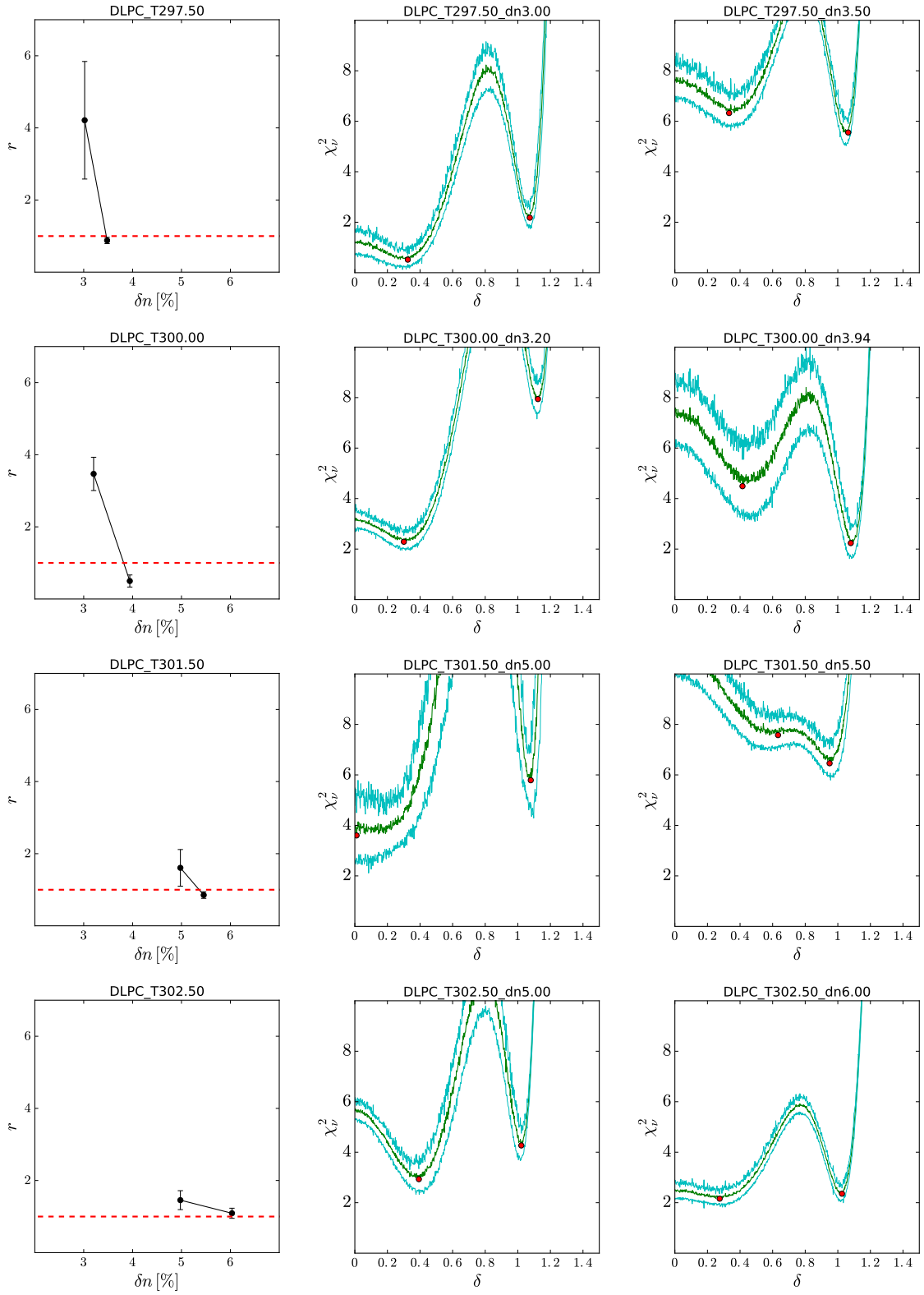

Figure 3.8: Plots of χ^2_ν as a function of δ for two closest values of δn to the transition (second and third columns), and the extrapolation for finding δn_c (first column), for MARTINI DLPC bilayers simulated at four different temperatures.

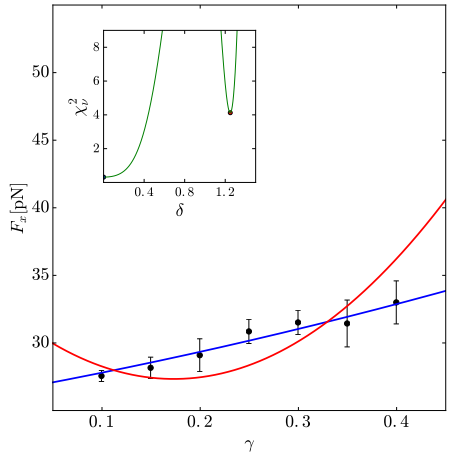

$\delta n = 2.47$

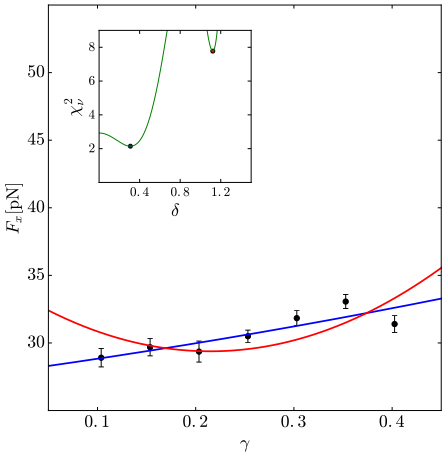

$\delta n = 3.20$

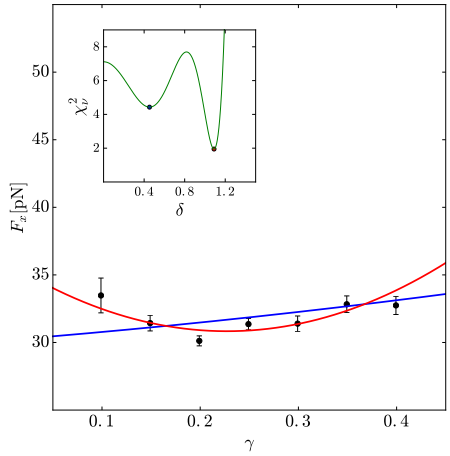

$\delta n = 3.94$

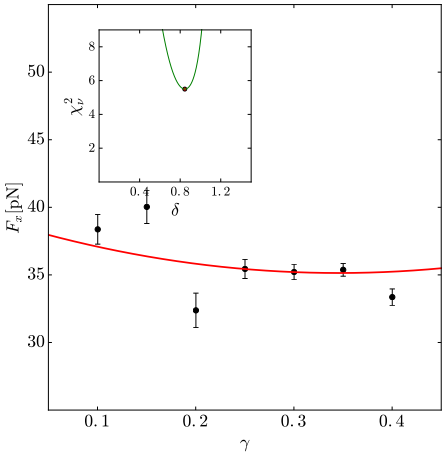

$\delta n = 5.26$

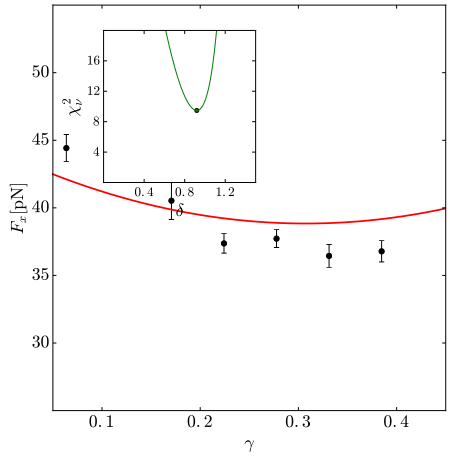

$\delta n = 5.94$

Figure 3.9: Stress-strain plots for DLPC at 300 K simulated at different number asymmetry values δn.

$\partial E_{\mathrm{stretch}}/\partial A_{\mathrm{f}} = 0$ then leads to

$$\frac{A_{\mathrm{i}}}{A_{\mathrm{f}}} = \alpha_+ \frac{a_{\mathrm{s}+}}{a_{0+}} + \alpha_- \frac{a_{\mathrm{s}-}}{a_{0-}} \ , \tag{3.21}$$

where we defined $\alpha_j = K_{A,\mathrm{m}j}/(K_{A,\mathrm{m}+} + K_{A,\mathrm{m}-})$. Eqn. (3.21) fixes the equilibrium areas per lipid, $a_j^* = A_{\mathrm{f}}/N_j$, from which we can subsequently calculate the area strain $\gamma_\pm$ in each leaflet:

$$\gamma_\pm = \frac{a_\pm^*}{a_{0\pm}} - 1 = \alpha_\mp \, \frac{a_{\mathrm{s}\pm}/a_{0\pm} - a_{\mathrm{s}\mp}/a_{0\mp}}{\alpha_+ \, a_{\mathrm{s}+}/a_{0+} + \alpha_- a_{\mathrm{s}-}/a_{0-}} \ . \tag{3.22}$$

Since $\Sigma_\pm = K_{A,\mathrm{m}\pm}\gamma_\pm$, we readily verify that $\Sigma_+ + \Sigma_- = 0$. Moreover, with a fairly good approximation $\alpha_+ = \alpha_- = 1/2$, which permits the further simplification

$$\gamma_\pm = \pm \, \frac{r-1}{r+1} \qquad \text{with} \qquad r = \frac{a_{\mathrm{s}+}/a_{0+}}{a_{\mathrm{s}-}/a_{0-}} \ , \tag{3.23}$$

showing that at this level even the strains add to zero.

Notice now that the two ratios $a_{\mathrm{s}j}/a_{0j}$ quantify the extent to which the area per lipid differs between a monolayer and a single stress-free leaflet in a bilayer. This ratio depends on the lipid composition of the leaflet (and the experimental conditions for the respective monolayers), and so the ratio r of these two ratios generally differs from 1 when asymmetric membranes are created in a layer-by-layer process. Eqn. (3.23) then explains how the two leaflets inherit a nonzero area strain and a *differential stress*, even after the *net stress* has relaxed. However, if we create a symmetric membrane by this layer-by-layer process, the two ratios $a_{\mathrm{s}j}/a_{0j}$ will be identical, implying $r = 1$ and $\gamma_\pm = 0$. This shows that even though the phase transfer protocol starts out with two monolayers, neither of which need reproduce the correct area per lipid for a bilayer, the symmetric control experiment actually restores the stress balance. If stiffening really results from differential stress, symmetric vesicles produced in this way would not show stiffening—in agreement with the actual observation [84].

There is another observation which suggests that at least *some* differential stress ought to have been present in the vesicles of Elani *et al.*: recall from our discussion in 2.3.1 that an asymmetric DOPC-POPC membrane in the absence of differential stress should have a spontaneous curvature of $K_{0\mathrm{b}} \approx -0.017\,\mathrm{nm}^{-1}$. Since the giant unilamellar vesicles used in these experiments had radii of about $R_0 \sim 20\,\mu\mathrm{m}$, this implies a huge reduced spontaneous curvature $|R_0 K_{0\mathrm{b}}| \sim 300 \gg 1$, which in turn indicates that these vesicles should have a very high tendency to tubulate. The fact that this was not observed suggests a differential stress which compensates the huge materials-based spontaneous curvature. As we have shown following Eqn. (2.11), the overall spontaneous curvature $K_0^\star$ gets reduced to zero when a tension of about $0.8\,\mathrm{mN/m}$ is present.

T [K]	290	297.5	300	301.5	302.5	310
δn_c	gel	3.46	3.82	5.36	6.30	none
$\Delta\,\delta n_c$		± 0.59	± 0.22	± 1.30	± 1.76	

Table 3.2: Estimated critical asymmetry δn_c and its statistical uncertainty $\Delta\,\delta n_c$ for simulated MARTINI DLPC bilayers at different temperatures. For 290 K the membrane entered a gel phase already at zero differential stress, and for 310 K we never observed stiffening.

3.4 The effect of temperature and lipid type

In the previous section we analyzed stiffening driven by differential stress for a MARTINI DLPC membrane at 300 K, showing that beyond a critical asymmetry of $\delta n_c \approx 3.8\%$ the membrane enters a phase in which the bending rigidity is significantly larger than at smaller asymmetries. To see how the location of this transition depends on the temperature of the system, we here extend the analysis to a range of temperatures around the original state point $T = 300\,\mathrm{K}$. The results are summarized in Table 3.2 and displayed in Fig. 3.13. GROMACS 2018.1 was used for simulations discussed in this section. The underlying stress-strain curves and fits for the additional temperatures of 297.5 K, 301.5 K, and 302.5 K can be found in Fig. 3.10, Fig. 3.11, and Fig. 3.12, respectively.

We determine the membrane rigidity for asymmetries up to $\delta n = 6.5\%$. Within a temperature range of several degrees around the previously studied case we again find stiffening—characterized both by a discontinuous increase in bending rigidity κ and a concomitant increase in the curvature softening parameter δ. Importantly, as the temperature grows, the critical asymmetry δn_c required to enter the stiffened phase increases as well. This effect is very strong: within a window of about 5 K the critical asymmetry grows by about 3 percentage points, with the data suggesting that the slope of $\partial\delta n_c/\partial T$ also increases with temperature (notice, though, that we have no model to explain the functional form of $\delta n_c(T)$).

The bilayer asymmetry δn_c is accompanied by a differential stress between the two leaflets. Within a simple empirical model we can estimate its magnitude: if the upper and lower leaflets contain N_+ and N_- lipids, which in equilibrium have specific area a, then the elastic energy of the bilayer as a function of its area A is

$$E = \frac{1}{2}K_{A,\mathrm{m}}\frac{(A - N_+a)^2}{N_+a} + \frac{1}{2}K_{A,\mathrm{m}}\frac{(A - N_-a)^2}{N_-a}\ , \tag{3.24}$$

where $K_{A,\mathrm{m}}$ is the monolayer expansion modulus (at equilibrium area). The condition $\partial E/\partial A = 0$ yields the resting area at zero net tension, namely a times the harmonic

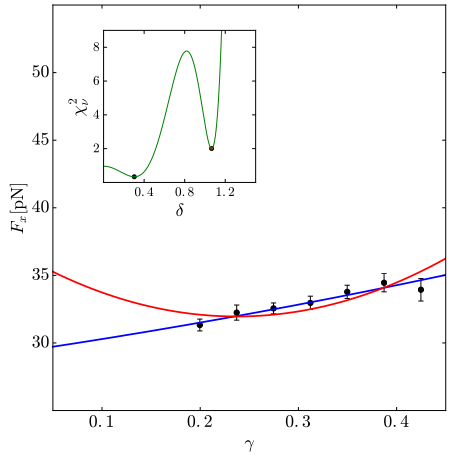

$\delta n = 3.02$

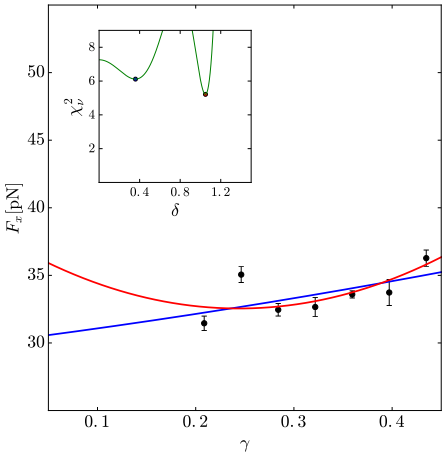

$\delta n = 3.48$

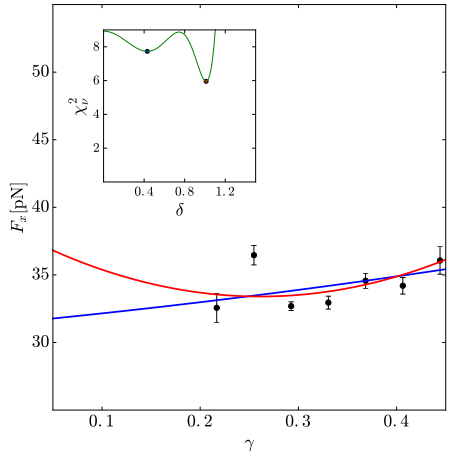

$\delta n = 4.04$

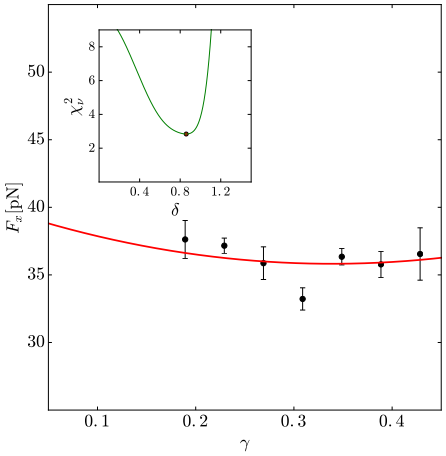

$\delta n = 4.50$

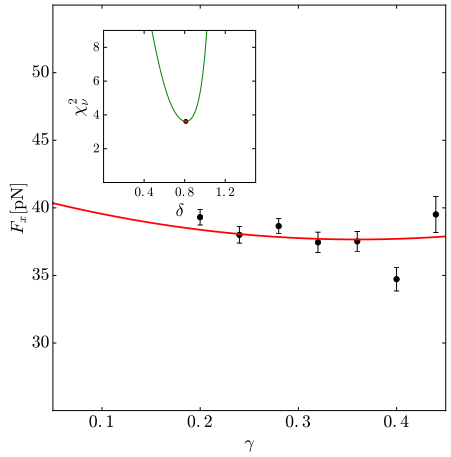

$\delta n = 4.98$

Figure 3.10: Stress-strain plots for DLPC at 297.5 K simulated at different number asymmetry values δn.

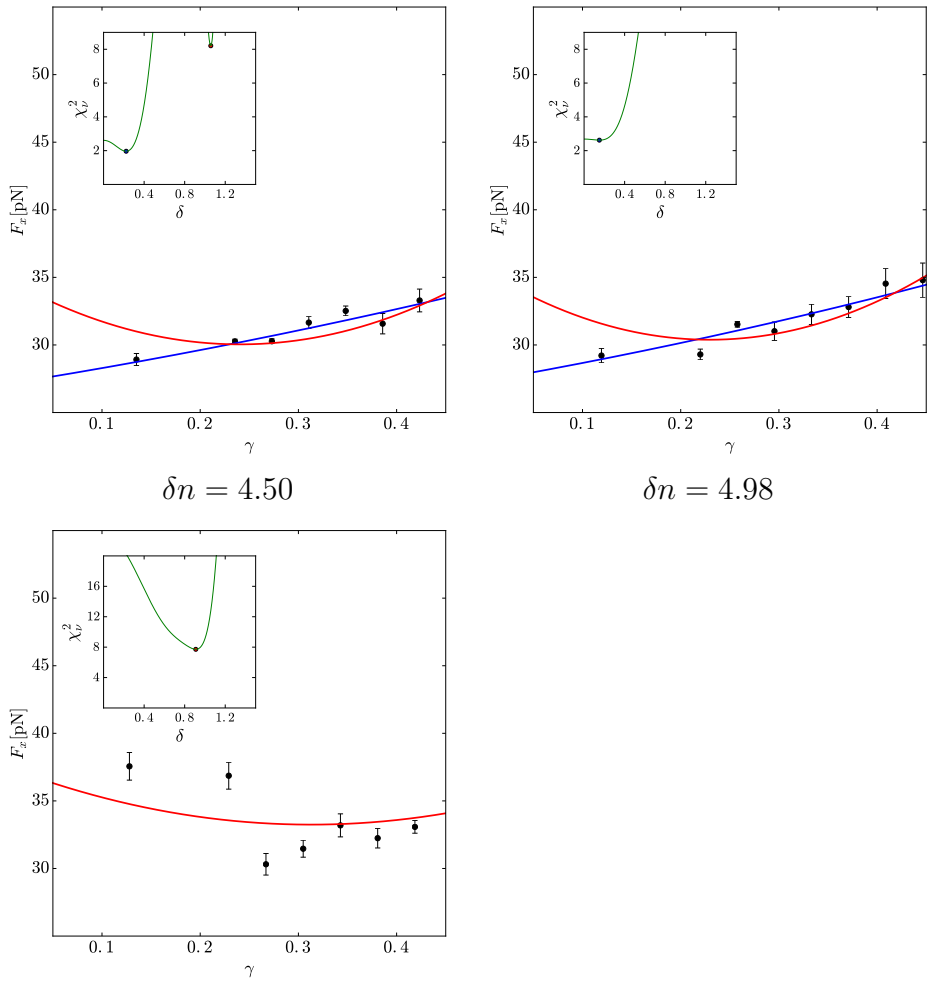

Figure 3.11: Stress-strain plots for DLPC at 301.5 K simulated at different number asymmetry values δn.

mean of N_+ and N_-, from which we get the tension in each leaflet:

$$\Sigma_\pm = \mp K_{A,\mathrm{m}}\,\delta n\ . \tag{3.25}$$

For many lipid bilayers $K_{A,\mathrm{m}} = \frac{1}{2}K_A$ is about 120 mN/m [114]. A change in δn by one percentage point therefore increases the leaflet tensions by about 1 mN/m. For comparison, the rupture tension of membranes comprising lipids with up to one double bond in the tails is about 10 mN/m, with significantly smaller values as the degree of unsaturation increases [167]. We suspect that this also limits the leaflet tension that differentially stressed membranes can maintain, even though—in contrast to a tense membrane—a differentially stressed one need not rupture as a whole. Instead, we expect that a defect opens up in the tense leaflet that will permit lipids from the

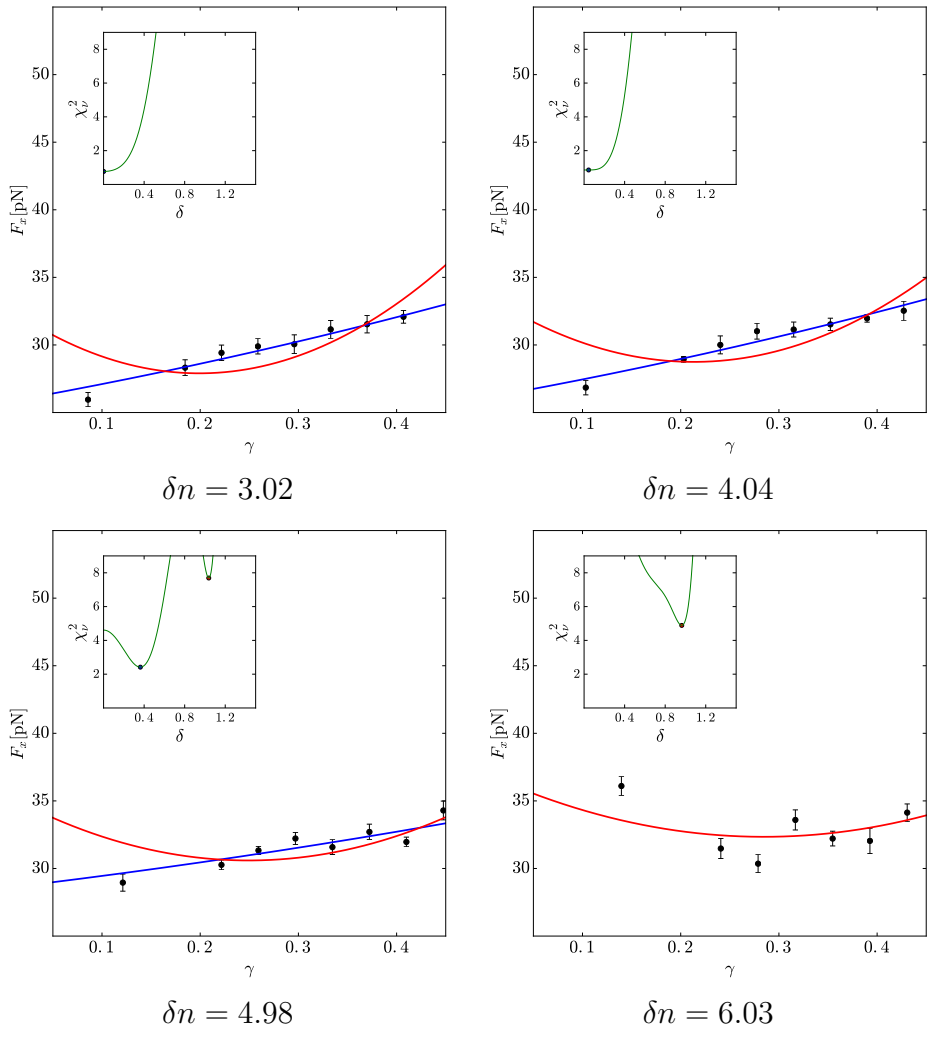

Figure 3.12: Stress-strain plots for DLPC at 302.5 K simulated at different number asymmetry values δn.

overcrowded leaflet to flip through, thereby lowering the differential stress, until the local defect closes up.

Assuming that the achievable differential stress is indeed limited to about 10 mN/m, and remembering that (from Fig. 3.13) each mN/m translates to a temperature change of about 1 K, we expect the temperature range within which a stiffening transition can be observed to be no more than about 10 K. We caution the reader, though, that our data are based on MARTINI level simulations under conditions of very significant differential stress, *i. e.*, conditions for which this CG force field has not been parameterized or validated. It is hence conceivable that the temperature window for which stiffening happens in experiment is somewhat different. However, that increasing temperatures require an increasing asymmetry to drive stiffening strikes us as robust.

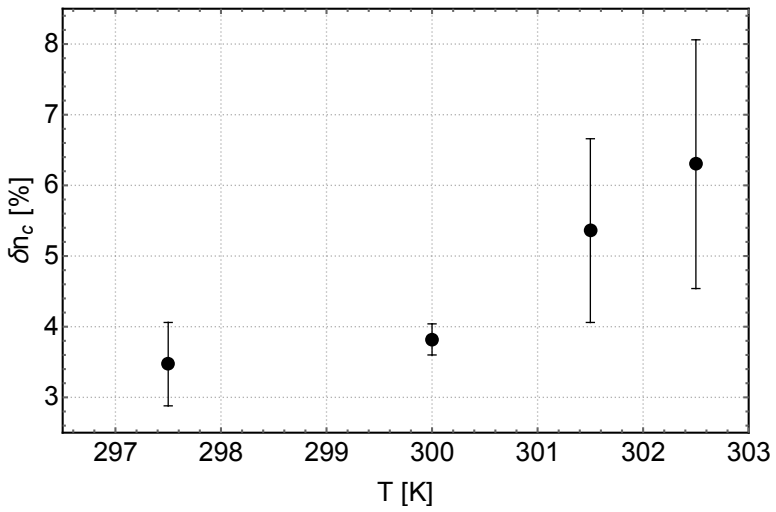

Figure 3.13: Estimated critical asymmetry δn_c of MARTINI DLPC membranes as a function of temperature; data from Tab. 3.2.

Compared to disordered fluid phases, a membrane's curvature rigidity is larger for ordered lipid phases [169,173,177], in particular for gel phases [163,165,166,168,171]. This suggests a connection between the stiffening transition and the main phase transition; but if so, the relation is subtle. We have shown that increasing differential stress will ultimately drive a DLPC membrane across a phase transition (presumably induced by the forced reduction in area per lipid of the compressed leaflet, which makes it increasingly gel-like), but a complete transition to the gel phase requires a higher asymmetry than the one at which the stiffening transition occurs.

Still, the findings in Fig. 3.13 indicate that as the temperature T increases, and with it the distance to the main phase transition T_m, increasingly large asymmetries are required to trigger the stiffening transition—or, conversely, ever smaller ones are needed as we approach the gel transition from above. Below the gel transition itself stiffening would then be present without any asymmetry, and so we expect the stiffening transition only to be observable for $T > T_m$. This then also implies that the temperature window of about 10 K mentioned above begins at T_m, and hence we expect that a stiffening transition only occurs within 10 K above a membrane's main phase transition (at least when based on our MARTINI data).

Increasing the temperature generally increases a membrane's area per lipid and decreases its lipid order. But the same effect on a membrane's fluidity can also be achieved by adding double bonds to the tails, *i. e.*, increasing the degree of tail unsaturation, or by decreasing lipid tail length [11]. Consider two lipids for comparison: DLPC (di-12:0 phosphatidyl choline), which we have investigated so far, and POPC (16:0-18:1 phosphatidyl choline), which has longer tails but also a cis double bond in its sn2 chain. The longer tails would raise the melting temperature, while the double bond lowers it, and it turns out that in this case both effects compensate: both

DLPC and POPC undergo their main phase transition at approximately the same temperature, −1 °C for DLPC [174] and −2.5 °C for POPC [170].

Recall, though, that the transition temperatures for MARTINI lipids need not coincide with those of their real counterparts, and they are also not very precisely known. Rodgers *et al.* [172] find that MARTINI-DLPC transitions at 274 K, which is actually fairly close to the expected value. However, the authors suspect hysteresis effects that are difficult to pinpoint, which may be up to 20 K. In our own simulations (in elongated boxes, to avoid artifacts due to "strutting") we find that MARTINI-DLPC at 290 K is soundly in the gel phase, and even our simulations at 297.5 K can be pushed into a gel phase in which it is at least metastable. We wish to emphasize, though, that the more recently recommended shorter cutoff of 1.1 nm for non-bonded interactions in the MARTINI model [160] reduces the overall cohesion and hence lowers the main phase transition temperature. We hence do not wish to put too much significance onto the absolute value of the temperature; what matters more is that we are close to but above the phase transition.

To the best of our knowledge, the transition temperature for MARTINI-POPC has not been determined. We find that at 300 K the lipid is in the fluid phase, which is expected. Moreover, we observe that an asymmetric MARTINI-POPC membrane does not enter a stiffened phase, at least up to $\delta n = 6.52\%$ (the largest asymmetry we studied), suggesting that it is more fluid than MARTINI DLPC. However, for the two largest studied asymmetries ($\delta n = 4.98\%$ and 6.52%), we observe the characteristic double-minimum structure in $\chi^2_\nu(\delta)$; and the minimum at large δ, even though still metastable, has come down close enough that we expect a transition to occur shortly above the highest asymmetry we studied. Extrapolating from the two last points we estimate the stiffening transition to occur at $\delta n_\mathrm{c} = (6.86 \pm 0.56)\%$. Fig. 3.14 shows stress-strain plots for simulations of MARTINI POPC bilayers with different asymmetry values at 300 K.

3.5 Interplay of order and curvature

Symmetric, flat, tensionless membranes transition into a gel phase at some well-defined temperature, but for asymmetric membranes we expect several differences. We will leave a more detailed analysis of the underlying physics to future work, but without going into details, it is clear that the overfilled leaflet is more likely to gel, because the reduced area per lipid already places it into a state of higher lipid order. But then, this leaflet is unlikely to transition "in on go", since its overall area is tightly coupled to the area of the apposing underfilled leaflet. In other words, the compressed leaflet's lateral boundary condition is not one of constant stress but contains aspects of both a constant stress and a constant strain ensemble. As such, we should expect to find finite domains of higher order, at least at sufficient asymmetry. This is indeed true, as Fig. 3.15 shows: the compressed leaflet in a differentially stressed flat membrane strip can develop an ordered domain (which connects across

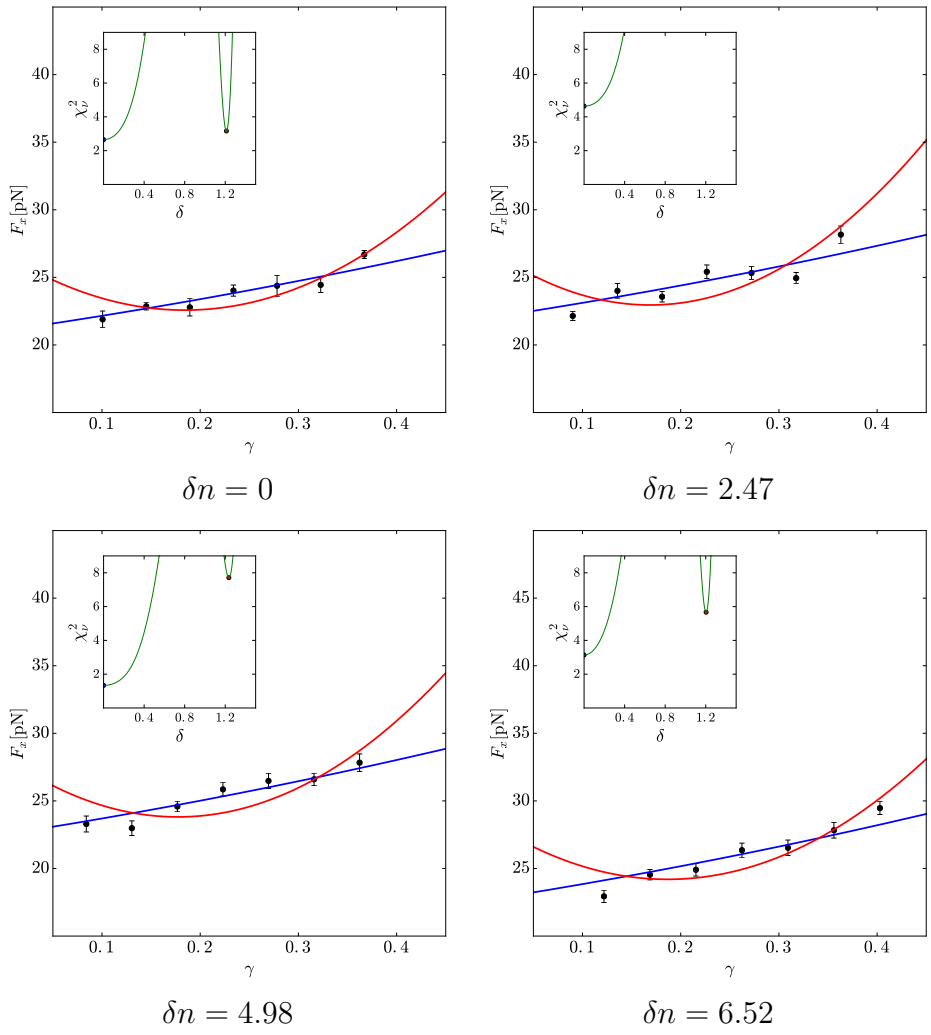

Figure 3.14: Stress-strain plots for POPC at 300 K simulated at different number asymmetry values δn.

the short dimension), but this domain need not grow to cover the entire leaflet.

Now recall that buckling breaks a bilayer's translational symmetry by creating curvature gradients, and that a high degree of lipid order is more likely to occur in the flat regions surrounding a buckle's inflection point than in the curved regions where it turns (especially the "inside" bends). This suggests that finite domains of higher lipid order, created by the asymmetry, are driven towards a buckles' inflection points, due to shape gradients. As a result, we get buckled membranes that are likely stiffer in their inflection regions than their turning regions, which will render the resulting buckle more "pointy" compared to classical Euler buckles. This is precisely the scenario captured by the theory for curvature softening we used [75].

In order to quantitatively examine this scenario, we have measured the average

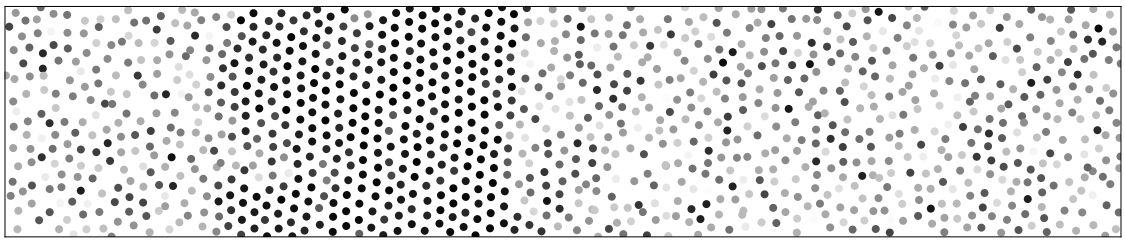

Figure 3.15: Typical snapshot of the location of lipid tails in the compressed leaflet of a differentially stressed but *flat* MARTINI-DLPC membrane ($T = 300\,\mathrm{K}$, $\delta n = 5.94\%$). The greyscale represents hexatic order parameter, ranging from white to black for values of HOP from 0 to 1. The ordered band visible on the left side does not grow to encompass the whole leaflet, even though its overall width slightly fluctuates.

hexatic order parameter $\Psi_6(s,t)$ of lipid tails, by some suitable binning resolved along the arc length s of the buckle and the time t, as described in Sec. 3.1.3. Once the membrane has transitioned into a stiffened phase, we indeed observe well-defined "bands" of more highly ordered lipids in the compressed leaflet, which invariably start at and then hover near an inflection point—see Fig. 3.16. At stronger asymmetry, or lower temperature, they are more likely to appear and, if so, are also wider. Particularly wide bands might link the two inflection points via the outer (and hence less curved) turning point. Ultimately, the entire compressed side can be ordered.

The emergence of these ordered domains shows distinct characteristics of a first order transition, just as the stiffening transition does. Most visibly, if an initially disordered leaflet develops an ordered band, it grows to its equilibrium width fairly rapidly, but it may take quite a while for the growth to start—as one would expect for a nucleation process that requires a barrier to be crossed. This is most noticeable for asymmetries in the vicinity of the stiffening transition, for which the width of the band also shows more pronounced fluctuations. For instance, Fig. 3.17 shows the time series of the hexatic order parameter $\Psi_6(t)$, averaged over the entire compressed leaflet of a buckled DLPC membrane, for three independent simulations at $T = 301.5\,\mathrm{K}$ and asymmetry $\delta n = 5.45\%$, always at the buckling strain $\gamma = 13\%$. The fairly rapid transition into the more ordered phase is readily visible, but the waiting times for that transition are very different.

To get more statistics, we simulated this system 24 times: 8 times while holding it at 301.5 K, 8 times in which the simulation had been preceded by a 300 ns successive warm-up starting at the lower temperature 300 K, and 8 times in which the simulation had been preceded by a 300 ns successive cool-down starting at the higher temperature 303 K. The order parameter Ψ_6 for the compressed leaflet, averaged over the entire leaflet as well as over time, takes values between about 0.44 and 0.55 (which hardly depend on the temperature history). This scatter does not happen because all these order parameters can stably occur, but because Ψ_6 is a linear combination of the two order parameter values that corresponds to states with and without an ordered band,

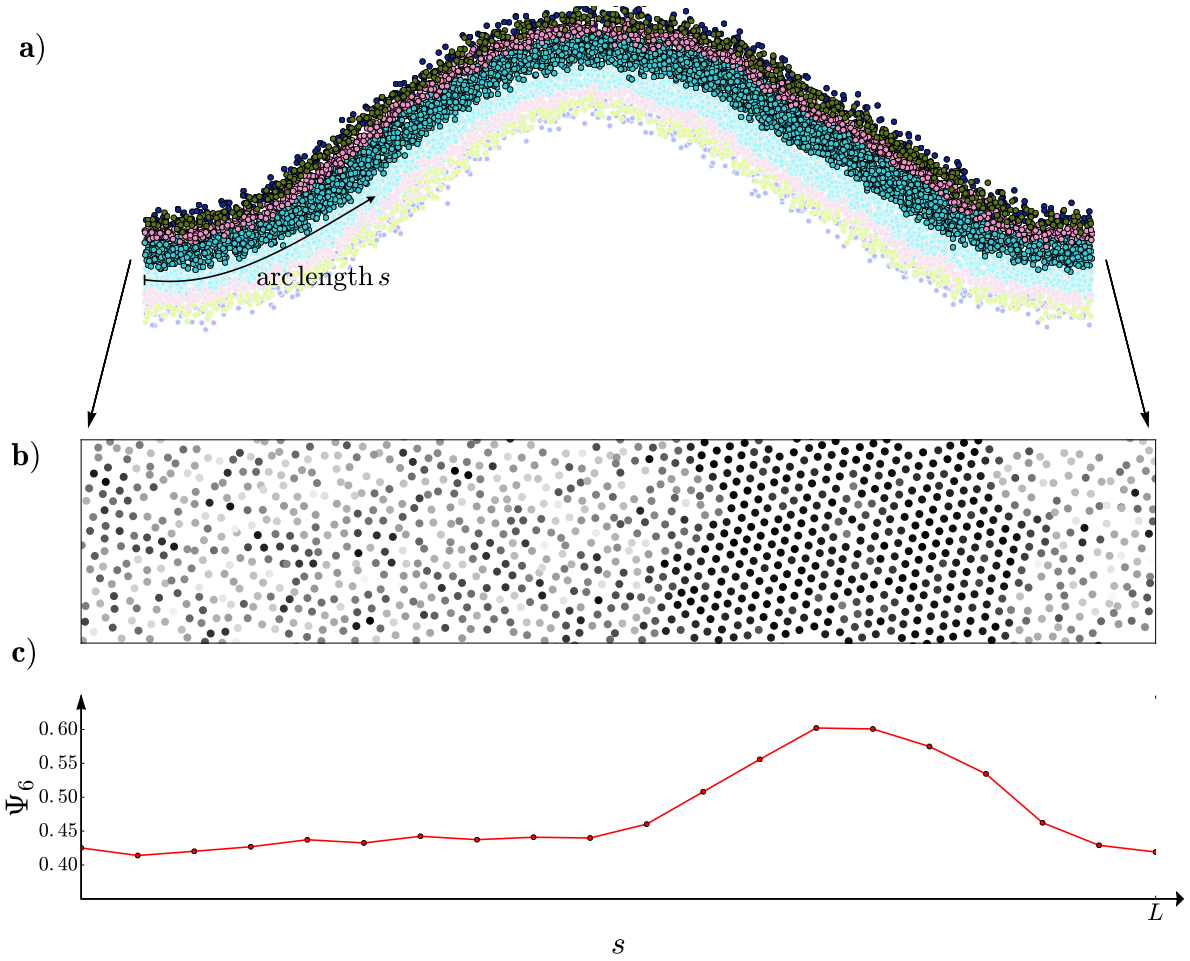

Figure 3.16: a) Side-view of a MARTINI-DLPC buckle ($T = 300\,\mathrm{K}$, $\delta n = 3.94$, $\gamma = 15\%$) that exhibits an ordered domain in the compressed (upper) leaflet near the right inflection point. b) Location of upper-leaflet lipid tails in the (s, y) coordinate system of the upper leaflet's reference surface, with the ordered band (corresponding to $\Psi_6 \gtrsim 0.45$) clearly visible in the right half. (This is the buckled analog of Fig. 3.15.) c) Hexatic order parameter $\Psi_6(s)$ as a function of arc length s, averaged over y and simulation time of $\Delta t = 1600\,\mathrm{ns}$.

weighted by the fraction of time the system spends in each state (see again Fig. 3.17). If we further plot the average buckling force $F_x = L_y f_x$ against Ψ_6, we arrive at a linear relation—as seen in Fig. 3.18. This indicates that the buckling stress, too, is a linear combination of the stresses belonging to states with and without an ordered band, and the state with a band resists buckling more strongly.

In the vicinity of the stiffening transition the ordered bands may require a long time to form—"long" at least compared to our overall simulation time. Considering that near the transition we expect the system to fluctuate back and forth between

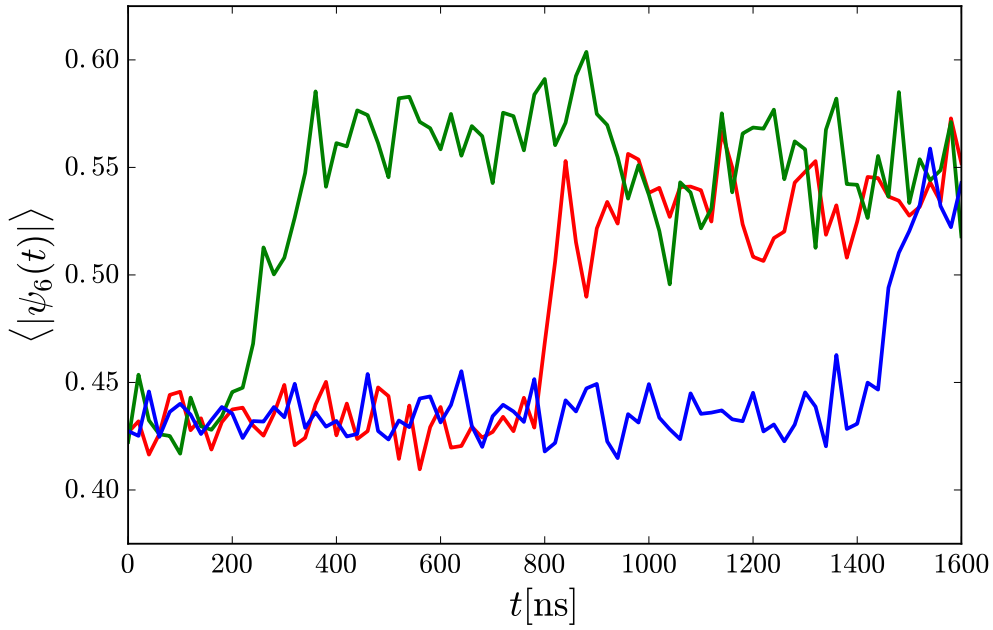

Figure 3.17: Three representative time series of the hexatic order parameter $\Psi_6(t)$, averaged over the compressed leaflet of a differentially stressed MARTINI-DLPC buckle ($T = 301.5\,\mathrm{K}$, $\delta n = 5.45$, $\gamma = 13\%$), obtained in three independent simulations. The transitions mark the emergence of an ordered band and take a comparatively short time to complete, while the waiting times up to a transition shows a wide distribution.

banded and non-banded states, with long waiting times between transitions, it is impossible to sample the two states (with their two different buckling stresses) with their correct statistical weight (at least without resorting to additional sampling tricks). For that reason, the stress-strain relation near the stiffening transition shows a lot of data scatter and is much more difficult to fit than buckles well below the transition (which are readily fit with low values for κ and δ) or well above (which are readily fit with high values for κ and δ). While this makes a prediction for the precise *location* of the stiffening transition difficult, the fact that it *exists* is uncontroversial.

Let us illustrate the first order nature of this leaflet ordering transition with one final example. We observed that one of the simulated DLPC buckles ($T = 297.5\,\mathrm{K}$, $\delta n = 3\%$, $\gamma = 10\%$), underwent a transition in which it lost its buckling amplitude. Inspection revealed that the entire compressed leaflet turned into a gel phase, which reduced the buckle's contour length L close enough to L_x such that the strain γ vanished, and with it the net buckling stress. However, subsequently relaxing the constraint of fixed L_x and simulating this particular configuration instead under zero lateral tension along the x-direction did not trigger a re-melting of this membrane. This is of note, because this very system had previously been simulated as a flat bilayer at zero tension, set up in a fluid phase, in order to calibrate the reference

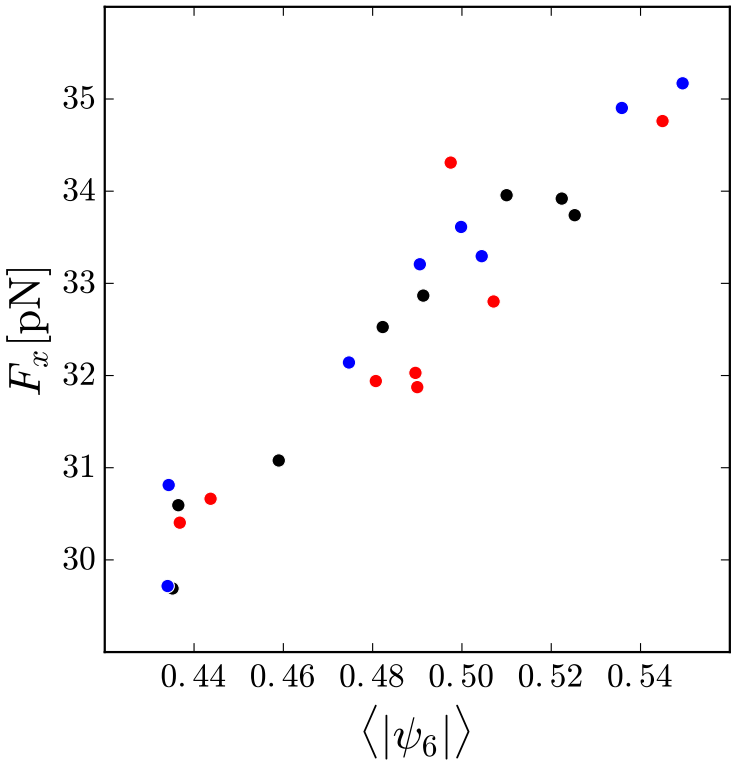

Figure 3.18: Average hexatic order parameter of all lipids in all frames of trajectories of multiple simulations of DLPC at $T = 301.5\,\mathrm{K}$ with $\delta n = 5.45$ buckled with $\gamma = 13\%$ plotted against the average pressure force F_x of that buckle in the x-direction. Red ("hot") points are from simulations initiated at $T = 303\,\mathrm{K}$ and gradually cooled down in steps of $0.1\,\mathrm{K}$, blue ("cold") points are from simulations initiated at $T = 300\,\mathrm{K}$ and gradually heated.

length L_x needed to calculate the strain after buckling. Hence, the system can exist in two different states of different area—a fluid membrane and one where the upper leaflet has gelled—that are separated by a sizable free energy barrier.

3.6 Finite size effects

To evaluate the impact of finite size effects on our stiffening simulations, we simulated the DLPC system at $T = 300\,\mathrm{K}$ with $\delta n = 3.20$ at two different system sizes: with 25% more and 25% fewer lipids than the previously studied system (which contained 580 lipids in its upper leaflet). Since we keep the buckle's width the same, this results in a $\pm 25\%$ change in the relaxed length of the bilayer, and a corresponding change in the radii of curvature.

Recall that at this asymmetry our original system did not exhibit stiffening (it only

set in at $\delta n_c = 3.82\%$, see Tab. 3.2). We observe that the smaller and larger systems do not experience stiffening either, but their distance from the transition point changes: while the small system moves even farther from the transition (no double minimum structure in $\chi^2_\nu(\delta)$ visible, unlike in the mid-sized system), the big system moves closer to the transition, in the sense that the minimum in $\chi^2_\nu(\delta)$ corresponding to the stiffened phase drops down so far that it is close to becoming the more stable phase.

We propose that this trend manifests the balance between lipid ordering and membrane curvature: the lipid number asymmetry in the bilayer increases the density of the compressed leaflet and moves it closer to an ordering transition, while the curvature we impose in the buckle used to measure the associated stiffening acts against lipid ordering. However, larger buckles have more extended flat regions near their inflection points, which seems conducive to the formation of an ordered phase in the compressed leaflet of the membrane (in the form of a "stripe", see Fig. 3.16), and so the suppression of order is weaker in bigger systems.

This result implies that the bare numbers we quote for the stiffening transition are system size dependent. More precisely, the observed trend, and the rationale for it, indicates that these number are *upper bounds* for δn, in the sense that the transition in the limit of ever smaller curvatures will move to smaller asymmetries. This is important for assessing the relevance of our proposed stiffening scenario for actual experimental systems: the giant unilamellar vesicles (GUVs) in which stiffening has originally been observed [84, 90, 92] are several orders of magnitude larger than the systems we study, and hence exhibit curvatures that are smaller by that same factor. It is therefore conceivable that substantially smaller asymmetries suffice to trigger stiffening in such macroscopic systems, compared to values such as $\delta n_c \sim 4\%$ which we find in our much smaller and much more highly curved buckles. And while number asymmetries of that magnitude appear to be within the range of what can be experimentally achieved if one explicitly sets out to do so, we remind the reader that the actual stress asymmetries arising in the original experiments [84,90,92] were likely ancillary—artifacts resulting from an incomplete cancellation of errors (see Sec. 3.3).

3.7 Broken mirror symmetry

One interesting aspect of the stiffening transition is that we almost never observe an ordered band at *both* inflection points of a buckle (see *e.g.* Fig. 3.16a). This asymmetry is particularly visible once bands become wider (*i. e.*, at larger asymmetries), because it may visibly affect the shape of the buckle by expanding the stiffer region around the banded inflection point and shortening the softer region around the non-banded inflection point—in other words, by breaking a buckle's mirror symmetry with respect to a vertical plane that cuts through the maximum. For a buckle at the state point $T = 297.5\,\mathrm{K}$, $\delta n = 4.50\%$, and $\gamma = 23\%$, this is illustrated in Fig. 3.19a: it "leans" slightly to the left, in accord with the fact that an ordered domain exists around the right inflection point.

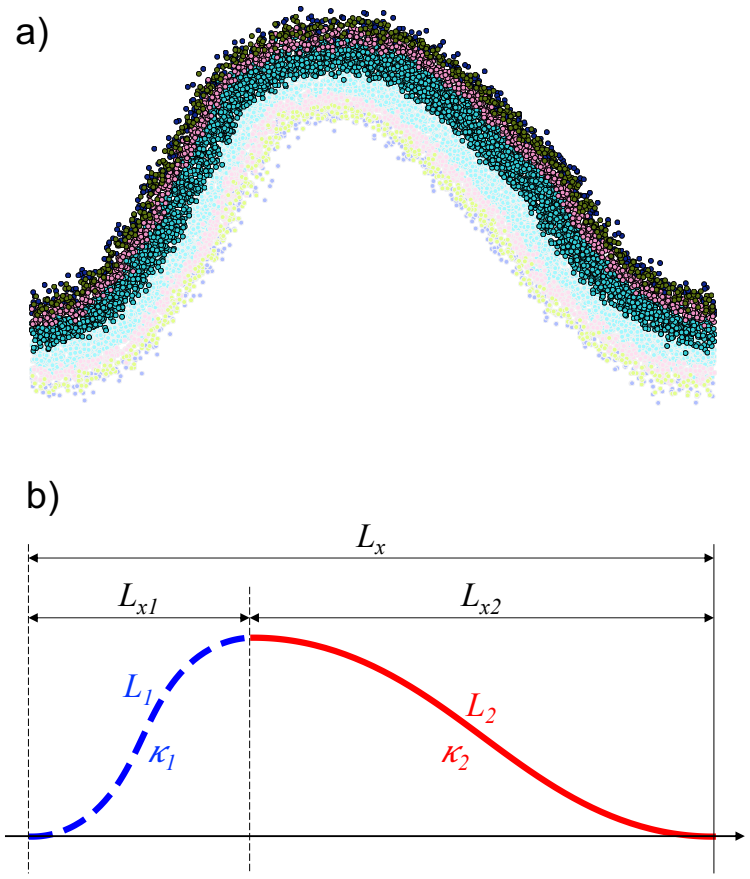

Figure 3.19: a) side-view of a MARTINI DLPC membrane (at $T = 297.5\,\mathrm{K}$, $\delta n = 4.50$, $\gamma = 23\%$) which exhibits an ordered domain in the compressed (upper) leaflet near the right inflection point. The observed shape asymmetry does not merely reflect an expedient choice of snapshot but holds up under a statistical analysis, at $p < 10^{-12}$. b) shape parameters describing the geometry of buckle with broken mirror symmetry.

To ascertain that the observed small asymmetry is significant, and not just a particularly large fluctuation in a suggestively chosen simulation snapshot, we define the order parameter $\phi = (L_{x2} - L_{x1})/L_x$, using the notation described in Fig. 3.19b; its value is nonzero if mirror symmetry is broken. (L_{x1} and L_{x2} were found by fitting a cubic spline to the buckle and calculating the horizontal distance between the minimum and the maximum of the curve, taking periodic boundary conditions into account.) For the system illustrated in Fig. 3.19a we find $\phi = 0.058 \pm 0.008$, and a (one-sided) significance test shows that $\phi > 0$ at $p = 2 \times 10^{-13}$. For a second system ($T = 297.5\,\mathrm{K}$, $\delta n = 4.98\%$, and $\gamma = 20\%$) we find $\phi = 0.083 \pm 0.007$, which is positive at $p = 10^{-32}$. This analysis shows that while the observed asymmetry is not large, it is systematically present.

That domains preferentially form at one inflection point, and then break a buckle's

mirror symmetry, is quite remarkable, because it is not expected within the theoretical model we have used so far—that of a bilayer capable of curvature softening [75]. One consequence of that model's analytical shape equation (with or without curvature softening) is that the local curvature is an even function of the buckle's angle with respect to the horizontal (see Eqn. (S8) in the supporting information of Ref. [75]), which immediately implies mirror symmetry.[1] Spontaneous symmetry breaking therefore needs an additional bistability in the free energy. In our case this is most likely provided by the phase behavior of the asymmetric membrane, which—as we have pointed out above—permits coexistence between a soft disordered and a stiff ordered phase (the "band"), separated by a free energy barrier. Notice that the coupling to the membrane geometry provides an additional positive feedback mechanism: if one inflection point develops a band and stiffens, its flat region extends at the expense of the flat region around the other inflection point, thus making it less likely for that second inflection point to also transition into a more ordered phase.

In practical terms, a broken mirror symmetry renders our analytical model for a buckle's stress-strain relation $f_x(\gamma)$ incomplete. While it captures a key idiosyncrasy of curvature localization—the non-monotonic behavior of $f_x(\gamma)$—the geometric shape underlying this prediction is incorrect. However, we believe this to be less problematic than it might seem at first, because we aim to predict the *energy* (or its derivative, the stress), not the *shape*. Recall that in all functional minimization problems a linear deviation in the function is only associated with a quadratic deviation of the functional's value, provided we are "close enough" to the minimum. This is for instance the reason why the Rayleigh-Ritz variational approach for estimating a Hamiltonian's ground state *energy* is often remarkably good, even if the associated estimate for the ground state *wave function* is not very reliable.

The more important lesson here is that differential stress does not stiffen a membrane by homogeneously changing its properties, or at least those of its compressed leaflet. Instead, beyond a critical asymmetry we find finite domains in the compressed leaflet, whose size increases with asymmetry, and which have a higher lipid order and a higher rigidity. The membrane hence becomes a *composite material*, and observables such as its bending modulus should be viewed as *effective* parameters that capture its properties over scales larger than the composite's granularity. If both inflection points were to form ordered bands, our extended theory for buckling already captures the effective nature of the problem, and the curvature softening parameter δ becomes a measure for how strongly the localized stiffening affects the global response. If instead such a band only forms at one inflection point, the symmetry breaks and we must develop more refined theories. This is not our goal in the present work; but in order to illustrate the basic idea, we give an explicit example in the the next section for how buckling of such a composite sheet leads to an effective bending modulus that arises as a (typically nontrivial) average of the two pure-phase rigidities.

[1] I would like to thank Zach McDargh for this elegant argument.

δn	γ	$\kappa(\delta n)$	κ_1	κ_2
4.50%	23%	43.23 ± 1.02	38.28 ± 0.99	47.04 ± 1.16
4.98%	20%	44.84 ± 0.80	39.46 ± 0.80	50.11 ± 0.99

Table 3.3: Membrane curvature moduli (measured in units of $k_{\mathrm{B}}T$) for two types of DLPC buckles at $T = 297.5\,\mathrm{K}$ that exhibit a broken mirror symmetry. $\kappa(\delta n)$: the net rigidity of the full buckle, measured at this asymmetry δn; κ_1: the rigidity inferred for the shorter (and less ordered) half-buckle via an analyis of the buckle's broken mirror symmetry and Eqn. (3.31); κ_2: the rigidity inferred for the longer (and more ordered) half-buckle via the κ_2-analogue of Eqn. (3.31).

3.8 Two dissimilar half-buckles in series

Here we briefly investigate the effective rigidity of a composite membrane by looking at the special case of a buckle that comprises two domains of different rigidity, each of which constitutes exactly half of a buckle. To keep the analytical effort manageable, we will not use the generalized buckling theory for curvature softening membranes but restrict to ordinary Euler elastica. Some of the underlying mathematics can be found in Ref. [148].

Consider therefore a system like the one in Fig. 3.19b. A buckle of total length L has two consecutive regions, labeled "1" and "2", where the bending rigidity is κ_1 and κ_2, respectively. These two regions take up the lengths $\{L_1, L_2\}$ along the buckle, such that $L_1+L_2 = L$, as well as the *projected* lengths $\{L_{x1}, L_{x2}\}$, with $L_x = L_{x1}+L_{x2}$ being the projected length of the full buckle. We restrict to the special case in which both regions are half-buckles, which hence share the same amplitude and transmit the same (horizontal) buckling stress.

Let us define the fractions which these two regions take up along the buckle or along the projection as

$$\alpha_i = \frac{L_i}{L} \quad \text{and} \quad \alpha_{xi} = \frac{L_{xi}}{L_x} \ , \tag{3.26}$$

and the two individual buckling strains as

$$\gamma_i = \frac{L_i - L_{xi}}{L_i} = 1 - \frac{\alpha_{xi}}{\alpha_i}(1-\gamma) \ , \tag{3.27}$$

where $\gamma = (L - L_x)/L$ is the strain of the entire buckle.

The amplitude of an Euler buckle is given by $2\lambda\sqrt{m}$, where $\lambda^2 = \kappa/f_x$ is the ratio between bending rigidity and buckling stress, and where $m \approx \gamma - \frac{1}{8}\gamma^2 - \frac{1}{32}\gamma^3 - \cdots$ is the strain-dependent elliptic parameter entering the analytical solution [148]. Since two half buckles in series which differ in rigidity still share both amplitude and buckling stress, this gives, to lowest order in the strain,

$$\kappa_1\gamma_1 = \kappa_2\gamma_2 \ . \tag{3.28}$$

And the equality of stresses implies, again to linear order in the strain [148],

$$\kappa_1 \left(\frac{\pi}{L_1}\right)^2 \left(1 + \frac{1}{2}\gamma_1\right) = \kappa_2 \left(\frac{\pi}{L_2}\right)^2 \left(1 + \frac{1}{2}\gamma_2\right) . \tag{3.29}$$

We can view Eqns. (3.28) and (3.29) as two equations determining α_1 and α_{x1}. The solutions can be written down analytically, but are fairly complicated. However, in the limit of weak buckling, $\gamma_i \to 0$, they strongly simplify, and we find

$$\alpha_1 = \alpha_{x1} = \frac{1}{1 + \sqrt{\kappa_2/\kappa_1}} + \mathcal{O}(\gamma) . \tag{3.30}$$

And if we interpret the overall stress of the composite buckle as arising from a one-component system with rigidity κ, we can get its value by insisting that

$$\kappa \left(\frac{2\pi}{L}\right)^2 \left(1 + \frac{1}{2}\gamma\right) = \kappa_1 \left(\frac{\pi}{L_1}\right)^2 \left(1 + \frac{1}{2}\gamma_1\right) . \tag{3.31}$$

The presence of an extra factor of 2 on the left hand side reflects the fact that the effective buckle is a *full* buckle, while the two individual pieces are only *half* buckles. Inserting Eqn. (3.30) now yields (again: for small strain)

$$\kappa = \left(\frac{\sqrt{\kappa_1} + \sqrt{\kappa_2}}{2}\right)^2 , \tag{3.32}$$

which shows the effective rigidity to be the (delightfully unusual) square-mean-root average of the individual rigidities. (Due to the power mean inequality, this value lies between the geometric and the arithmetic mean of the two rigidities.)

Let us test these simple predictions by analyzing buckles which throughout a simulation trajectory exhibited persistent mirror symmetry breaking. We investigated two specific cases, both for the system at $T = 297.5\,\mathrm{K}$, which is close to the gel transition and hence likely to produce sizable ordered domains that can strongly affect the shape of the half-buckle on which they reside. Specifically, we looked at the systems $(\delta n = 4.50\%; \gamma = 23\%)$ and $(\delta n = 4.98\%; \gamma = 20\%)$, and we have argued in the previous section that their observed broken mirror symmetry is statistically highly significant.

Knowing the rigidity of the overall buckle, determined by the means described in Sec. 3.1.1, we can also quantify the asymmetry of the buckle by measuring the dimensions of its two half-buckles, as defined in Fig. 3.19b. We then use Eqn. (3.31) to infer the rigidities κ_1 and κ_2 of the un-stiffened and stiffened half-buckles, respectively. The results are shown in Table 3.3.

Since κ_1 refers to the un-stiffened part of the buckle, it should be the same between these two measurements; the (two-sided) p-value for that being the case is very high, $p = 35\%$. Moreover, we can also compare these κ_1 values to the rigidity of this

system at the smallest asymmetry we studied, in which it has not yet stiffened, which is $\kappa(\delta n = 3.02\%) = (36.16 \pm 0.99)\, k_{\mathrm{B}}T$. The p-values that these agree are $p_{\delta n=4.5\%} = 13\%$ and $p_{\delta n=4.98\%} = 1\%$.

Overall, this asymmetry analysis works remarkably well—better than it likely should, considering that the underlying theory relies on several simplifications (such as: the full buckle decomposes into two Eulerian half-buckles, both of which can be described by a non-curvature stiffened stress strain relation in the limit $\gamma \to 0$). At any rate, it supports the notion of stiffened domains that on average lead to a more rigid "composite" membrane.

Chapter 4

The role of cholesterol

While the relaxation times for asymmetric lipid compositions are very long for typical charged or zwitterionic phospholipids, cholesterol is believed to flip-flop several orders of magnitude faster [65, 187]. Hence, there exists a physiologically relevant time window within which phospholipids maintain their compositional asymmetry, while the cholesterol distribution is equilibrated between the leaflets. How does this change our considerations for spontaneous curvature and differential stress?

A comprehensive discussion of this situation goes beyond the scope of the present work, since it would require a much more careful treatment of the equation of state of lipid-cholesterol mixtures, as for instance recently given by Allender *et al.* [117]. But there is one important point we wish to emphasize: even if the cholesterol distribution can relax, this does *not* automatically imply that any previously existing differential stress will decay to zero, in contrast to a recent claim by Miettinen and Lipowsky [125]. This is because stress equilibration is not the thermodynamic condition that determines the distribution of cholesterol between the leaflets. The correct condition is equilibration of *chemical potential* [117], and this will not entail a stress relaxation, any more than the ability of water to cross a semipermeable membrane between two different osmolytes will relax the osmotic pressure.

4.1 Theory

Let us illuminate this point with a strongly simplified model. Consider a bilayer that contains $L_\pm$ lipids of type $\pm$ and specific area $a_\pm$ in its $\pm$ leaflets, and also add $N_\pm$ cholesterol molecules of specific area a to these leaflets. Making the rather crude assumption that lipid areas add, we expect an equilibrium total area $\mathcal{A}_\pm = L_\pm a_\pm + N_\pm a$ for each leaflet. Since generally $\mathcal{A}_+ \neq \mathcal{A}_-$, the membrane will be differentially stressed even at zero net tension. If the "normal" lipids stay in their leaflets, but cholesterol flip-flops to equilibrate its chemical potential (subject to the constraint $N_+ + N_- = N$), what is then the equilibrium area A, the final cholesterol distribution, and the resulting differential stress?

We propose that, for the purpose of the present argument, the relevant physics can be captured by an approximate empirical free energy that accounts for the following three major physical effects: (*i*) the partitioning free energy $g_\pm$ per cholesterol molecule into the two leaflets; (*ii*) the elastic energy of leaflet stretching or compression; and (*iii*) the entropy of cholesterol's distribution between the leaflets:

$$\begin{aligned} G(A, N_+) = &-g_+ N_+ - g_- N_- \\ &+ \frac{1}{2} K_{A,\mathrm{m}+} \frac{(A - \mathcal{A}_+)^2}{\mathcal{A}_+} + \frac{1}{2} K_{A,\mathrm{m}-} \frac{(A - \mathcal{A}_-)^2}{\mathcal{A}_-} \\ &+ N k_\mathrm{B} T \big[\varphi \log \varphi + (1 - \varphi) \log(1 - \varphi) \big] \ , \end{aligned} \tag{4.1}$$

where $\varphi = N_+/N$ is the cholesterol fraction in the +-leaflet and the last line is an entropic term that measures the distribution of cholesterol between the two leaflets (which is not considered part of $g_\pm$).

The condition $\partial G/\partial A = 0$ ensures zero net tension and gives the equilibrium area $A_\mathrm{eq} = (\alpha_+/\mathcal{A}_+ + \alpha_-/\mathcal{A}_-)^{-1}$, where $\alpha_\pm = K_{A,\mathrm{m}\pm}/K_A$. Notice that deriving this condition involves only the elastic contribution (second line) to the free energy. Upon inserting it back, this simplifies to

$$G_\mathrm{elast}(A = A_\mathrm{eq}, N_+) = \frac{1}{2} K_A \alpha_+ \alpha_- \frac{(\mathcal{A}_+ - \mathcal{A}_-)^2}{\alpha_+ \mathcal{A}_- + \alpha_- \mathcal{A}_+} \ . \tag{4.2}$$

Since this is proportional to the square of the difference of the original leaflet areas $\mathcal{A}_\pm$, the elastic part of the free energy *by itself* is minimized when $\mathcal{A}_+ = \mathcal{A}_-$.

The cholesterol distribution now follows from equilibrating cholesterol's chemical potential between the leaflets, which is equivalent to demanding $(\partial G/\partial N_+)_{A_\mathrm{eq}, N} = 0$. Unfortunately, this expression is very messy; but it simplifies considerably under the fairly good assumption that $K_{A,\mathrm{m}+} = K_{A,\mathrm{m}-}$, or $\alpha_+ = \alpha_- = \frac{1}{2}$. Expressing the cholesterol distribution via its deviation from even, $\psi := \varphi - \frac{1}{2}$, and expanding the entropy term to linear order around $\psi = 0$, we find after a short calculation

$$\psi(\Delta g, \Delta A_0, T) = \frac{\Delta g - \phi_0 K_A \Delta A_0 / N}{4 k_\mathrm{B} T + 2 \phi_0 K_A a} \ , \tag{4.3}$$

with the convenient abbreviations

$$\Delta g = g_+ - g_- \ , \tag{4.4a}$$

$$\Delta A_0 = L_+ a_+ - L_- a_- \ , \tag{4.4b}$$

$$\phi_0 = N a / (L_+ a_+ + L_- a_- + N a) \ . \tag{4.4c}$$

These three terms signify, in turn, the partitioning free energy difference per cholesterol molecule, the leaflet area difference in the absence of cholesterol, and cholesterol's

average area fraction in tensionless leaflets. The differential stress associated with this cholesterol distribution is

$$\Sigma_\pm = \left(\frac{\partial G_\pm}{\partial A}\right)_{T,A_{\rm eq},N} = \frac{1}{2}K_A\frac{\mathcal{A}_- - \mathcal{A}_+}{\mathcal{A}_- + \mathcal{A}_+} \tag{4.5a}$$

$$= \mp\phi_0 K_A\left(\frac{\Delta A_0}{2Na} + \psi(\Delta g, \Delta A_0, T)\right) \tag{4.5b}$$

$$= \mp\frac{1}{2}\phi_0 K_A\frac{\Delta A_0/Na + \Delta g/2k_{\rm B}T}{1 + \phi_0 K_A a/2k_{\rm B}T}\ . \tag{4.5c}$$

To elucidate the meaning of these predictions, it is instructive to examine two limiting cases. Let us first look at a situation in which both the partitioning free energy difference and entropic effects vanish (*i. e.*, $\Delta g = 0$ and $T = 0$). In this special case, Eqn. (4.3) simplifies to

$$\psi(\Delta g = 0, \Delta A_0, T = 0) = -\frac{\Delta A_0}{2Na}\ . \tag{4.6}$$

The cholesterol asymmetry is proportional to the bare-lipids area difference in the two leaflets, and it is easy to check that Eqn. (4.6) implies $\mathcal{A}_+ = \mathcal{A}_-$. In other words, the areas are balanced and, within the framework of our model, the differential stress vanishes exactly—as either Eqn. (4.5a) or Eqn. (4.5b) readily show.

Notice, though, that a full stress cancellation only occurs if we neglect entropic effects, because back-filling the expanded leaflet with cholesterol diverted from the compressed leaflet will imply a deviation from the true free energy minimum. Even if cholesterol prefers no leaflet over the other, entropic effects will create a partitioning shift $\Delta\psi$ away from the stress free state:

$$\Delta\psi = \psi(\Delta g = 0, \Delta A_0, T) - \psi(\Delta g = 0, \Delta A_0, T = 0) \tag{4.7a}$$

$$= \frac{\Delta A_0\, k_{\rm B}T}{N\phi_0 K_A a^2} + \mathcal{O}(T^2)\ , \tag{4.7b}$$

or

$$\frac{\Delta\psi}{\psi(\Delta g = 0, \Delta A_0, T = 0)} = -\frac{2\, k_{\rm B}T}{\phi_0 K_A a} + \mathcal{O}(T^2)\ . \tag{4.8}$$

This expression is negative, showing that the shift always *counteracts* the cholesterol displacement from Eqn. (4.6) that would fully eliminate the differential stress. Hence, in the presence of entropy, stress cancellation is incomplete, even when $\Delta g = 0$.

In the general case cholesterol will of course prefer one of the two leaflets of an asymmetric membrane over the other. Let us hence look at the second limiting case, in which a finite preference Δg exists, but where the bilayer creation process achieved $\Delta A_0 = 0$, *i. e.*, a bilayer which in the absence of cholesterol harbors no differential stress. Notice that (within our model) this would stay true if we added cholesterol

evenly to the two leaflets: $N/2$ molecules to each leaflet, or, $\psi = 0$. But if we now permit the cholesterol to flip-flop and find its true free energy minimum, we get

$$\psi(\Delta g, \Delta A_0 = 0, T) = \frac{\Delta g}{4k_{\mathrm{B}}T + 2\phi_0 K_A a} \ , \tag{4.9}$$

showing that if the +-leaflet is preferred by Δg, then a cholesterol asymmetry proportional to Δg arises. In other words: the addition of cholesterol may not only fail to fully balance the stresses, as in the previous case; it may actually *create* a differential stress that was not there in the absence of cholesterol. Notice that this is opposed by two different phenomena: first, the entropy (the first term in the denominator); and second, the fact that the emerging asymmetry creates new stresses that cost elastic energy (the second term in the denominator).

To estimate the magnitude of this asymmetry, let us take $\Delta g \approx 2\, k_{\mathrm{B}}T$, a recently determined partitioning free energy difference for cholesterol between a saturated stearoyl-sphingomyelin bilayer and an unsaturated POPC bilayer [188]. Using furthermore $K_A \approx 250\,\mathrm{mN/m} \approx 60\, k_{\mathrm{B}}T/\mathrm{nm}^2$ [114], $a \approx 0.25\,\mathrm{nm}^2$ [176], and $\phi_0 = 20\%$, this leads to a large partitioning asymmetry of $\psi \approx 36\%$ and, from Eqn. (4.5c), an associated differential stress of $|\Sigma_\pm| \approx 10\,\mathrm{mN/m}$ for the parameters chosen above—a *very* large value. This is most likely outside the regime of validity of our linear expansions, but it indicates that small partitioning differences can drive large stresses.

We hasten to add that this model has many weaknesses. For instance, we assume our partitioning free energies $g_\pm$ to be independent of the cholesterol content in each leaflet. This is incorrect not just because of the obvious role played by the chemical environment; there is also an *elastic* effect: even flat membranes have bending stresses due to nonzero spontaneous curvatures $K_{\mathrm{m}\pm}$, and since $K_{\mathrm{m}\pm}$ generally depends on the cholesterol mole fraction, this creates another thermodynamic driving force, as recently emphasized by Allender *et al.* [117]. An even more subtle issue is the assumption of area additivity, and the prerequisite of giving meaning to the notion of specific lipid area. This is fraught with numerous complications, because the presence of cholesterol in a bilayer changes the conformational ensemble of the host-phase lipids [185], affecting area per lipid [176,179–182] as well as other material parameters, such as the spontaneous curvature [117, 175, 185] and the bending rigidity [177, 178, 183, 184, 186]. In particular, addition of cholesterol can actually *contract* a membrane, leading to a negative *partial* specific area [176, 181]. To do better, we need a quantitative understanding of the underlying equations of state, but this is not the goal of the present work.

Let us now return to the claim by Miettinen and Lipowsky that the presence of a species with a high flip-flop rate will render the individual leaflets tensionless [125]. In their simulations, these authors studied an asymmetric membrane containing POPC in one leaflet, and a mixture of POPC with (two slightly different versions of) the ganglioside GM1 (the glycosphingolipid monosialotetrahexosylganglioside). Since POPC has one monounsaturated tail, and GM1 contributed with its saturated tails

at most up to 25 mol% in one of the leaflets, the partitioning free energy difference Δg is likely very small. These simulations hence appear closer to the first limit discussed above, in which cholesterol fosters an (incomplete) differential stress relaxation (see Eq. 4.7 and Eq. 4.8). This is indeed what the authors find, even if the stress in question is slightly more subtle in nature (namely: a residual differential stress). However, whether cholesterol would also undo a bilayer's differential stress in the presence of a noticeable Δg cannot hence be inferred from these simulations.

4.2 Simulation

In this section we use simulation to address the question whether a rapidly flip-flopping lipid species, such as in particular cholesterol, will distribute between the leaflets such as to eliminate any differential stress. The claim made by Miettinen and Lipowsky [125] contradicts our theory that paints a more complex picture: since the elastic energy is only one of several contributions to cholesterol's chemical potential, it is not the only one that guides its distribution between leaflets. In particular, we have presented a simple model in the previous section that shows how addition of cholesterol may not just fail to fully cancel a stress difference but actually *create* one—namely, if its free energy of partitioning differs sufficiently strongly between the leaflets.

To test the latter scenario in simulation, we have prepared a compositionally asymmetric bilayer of two lipid species with a significant difference in their ability to solvate cholesterol. One is the fully saturated DPPC, the other one the highly unsaturated DIPC (see Fig. 1.3). Since cholesterol prefers to partition into saturated phases [188], we expect it to have a preference for the DPPC side. Fig. 4.1 shows the results of simulations of symmetric MARTINI DPPC and DIPC bilayers with 30% cholesterol in each leaflet at 310 K to compare the flip-flop rate of cholesterol in these systems. These simulations show the flip-flop rate of cholesterol is higher in a DIPC bilayer compared to a DPPC bilayer.

We started by simulating two symmetric mixed membranes that consisted of a 4:1 mixture of either DPPC or DIPC with cholesterol. Using the average area densities obtained this way, we then created an asymmetric membrane with a (4:1) DPPC+Chol mixture on one side (72 DPPC lipids and 18 cholesterols), and a (4:1) DIPC+Chol mixture on the other (56 DIPC lipids and 14 cholesterols). Evolving this system from this initial condition we observed a strong tendency for cholesterol to re-partition into the DPPC leaflet, with an approximately exponential kinetics characterized by a relaxation time of about 200 ns, as illustrated in Fig. 4.2. After less than 1 µs the DPPC leaflet holds about 25 cholesterol molecules, *i. e.* about 80% of the total cholesterol content. Checking the differential tension at this end point, we find that it has the value $\Sigma_{\pm}^{(\mathrm{res})} = -3.71(88)\,\mathrm{mN/m}$, leaving the DPPC+Chol leaflet under a noticeable compressive stress.

The key difference to the simulation presented by Miettinen and Lipowsky is our

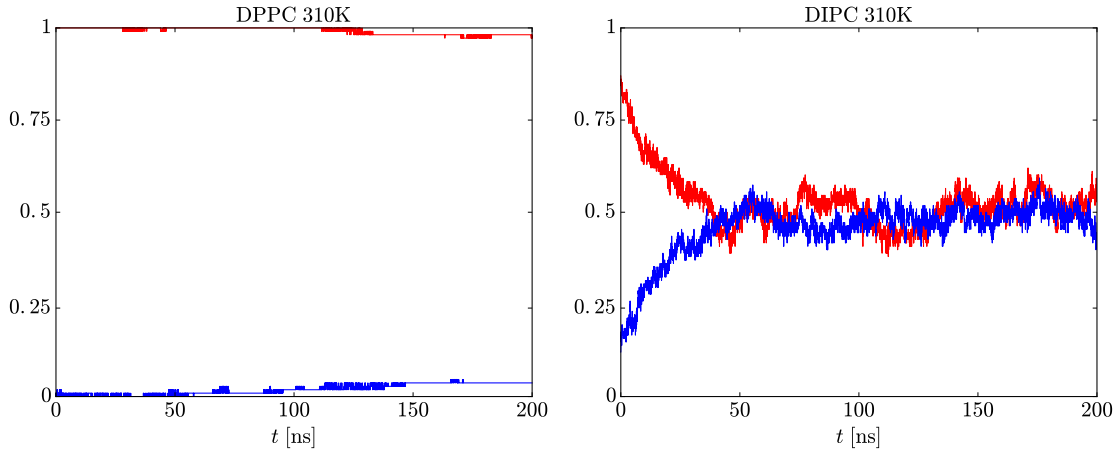

Figure 4.1: Fraction of cholesterol molecules in the upper leaflet with a starting position in the upper (red) or lower (blue) leaflets of symmetric DPPC (left) and DIPC (right) bilayers as a function of time. The initial state contained 30% cholesterol per leaflet (108 cholesterol molecules and 252 DPPC or DIPC lipids in each leaflet). The simulations were conducted at 310 K.

choice of lipid tails: we explicitly set up a situation in which cholesterol experiences a large differential free energy of partitioning Δg between the leaflets. This is not an unphysiological scenario, though. Consider for instance that the outer leaflet of a cell's plasma membrane contains all of the membrane's sphingomyelin, a strong cholestreol "recruiter". In fact Allender *et al.* [117] have estimated that this would drive almost 3/4 of the plasma membrane's cholesterol content into that leaflet, were it not for the elastic cost associated with cholesterol's change of a leaflet's spontaneous curvature, which turns out to counteract the driving force due to solvation. Under realistic situations the magnitude of this effect will depend on many other factors, and in a biological context it will of course be different for different membrane systems inside cells. But for now, our simple counter-example indicates that cholesterol will not automatically eliminate the differential stress of a membrane.

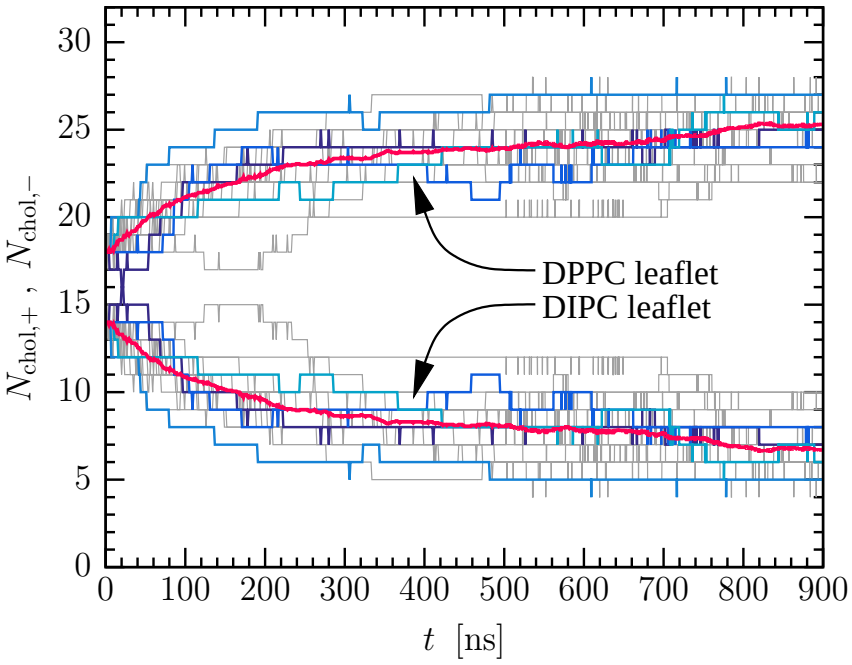

Figure 4.2: Number of cholesterol molecules $N_{\mathrm{chol},\pm}$ in the upper or lower leaflet of a $\frac{\mathrm{DPPC+Chol}}{\mathrm{DIPC+Chol}}$ bilayer as a function of time. The initial state contained 20% cholesterol per leaflet in an area-matched asymmetric system. Cholesterol flip-flop leads to a 25:7 redistribution with a relaxation time of about 200 ns. The graph illustrates 20 independent simulations, four of which are singled out in different shades of blue; the bold red curve is the average over all of them.

Chapter 5

Phase coexistence

In this chapter we present a rundown of methods we used to take a closer look at the coexistence between the disordered, fluid phase and the more ordered, gel-like phase in the compressed leaflet of asymmetrically-stressed bilayers. Furthermore, we address issues related to the free energy barrier separating the phase coexistence state from the fluid state, as observed in simulations of coarse-grained MARTINI lipids.

In order to do any analysis on the different phases during their coexistence, it was first necessary to identify the phase to which each lipid (each lipid tail, to be more precise) belongs at every point in time. Our first naive idea was to directly use the value of the hexatic order parameter (HOP) of the lipid tails as indicator of their phase, identifying tails with HOP greater than a certain threshold as being in the gel phase.

There are two problems with this approach to identifying phases: Firstly, it is not clear how to objectively determine the critical threshold value of HOP separating fluid and gel phases. Secondly, lipid tails that are clearly in the fluid phase, regularly happen to align relative to adjacent lipid tails in configurations corresponding to high HOP values. In fact, the HOP values of lipid tails in a leaflet that is unambiguously in the fluid phase have a distribution that spans the entire possible range of values between 0 and 1, and the fraction of lipid tails having a HOP value higher than any allowed arbitrary critical threshold would be non-zero. Fig. 5.1 shows the distribution of values of HOP of all lipid tails over the entire span of a 1.6 μs simulation of a symmetric bilayer of MARTINI DLPC lipids at 300 K, which is entirely in the fluid phase.

Inspired by a paper from Lyman *et al.* [193], in which the authors successfully used a hidden Markov model (HMM) to identify the local membrane phase in all-atom simulations of ternary systems with L_o/L_d phase coexistence, we decided to try utilizing a similar (but not identical) method. The following section briefly introduces HMMs and describes how we found them advantageous.

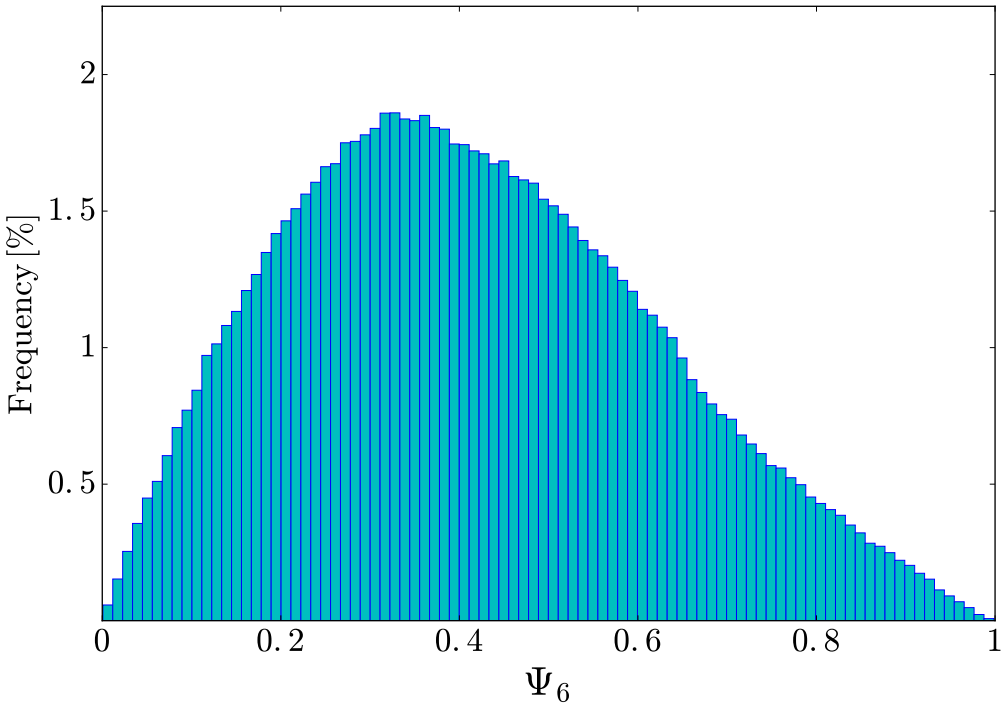

Figure 5.1: Distribution of hexatic order parameter Ψ_6 values of the two tails of 400 MARTINI DLPC lipids of one leaflet of a symmetric bilayer over 800 evenly-spaced snapshots from a simulation at 300 K lasting 1600 ns in total.

5.1 Hidden Markov model

Initially introduced in the late 1960s [189] and extensively used in the field of bioinformatics [191] among others, a hidden Markov model describes a Markov process with a set of unobservable (or *hidden*) states together with a set of observables whose behaviour depends on the Markov process. The hidden state of the system at every step is determined by its hidden state in the previous step through a probability matrix of transition between states, and the observables, which can be discrete or continuous, are determined from the hidden state through output (or *emission*) probabilities [192].

For a given sequence of observables, the most likely values of transition and emission probabilities are determined using the Baum-Welch algorithm [190]. Once these probabilities are known, the Viterbi algorithm can be used to determine the most likely sequence of hidden states corresponding to the observables [194].

While Lyman *et al.* [193] used the local lipid composition (lipid types of the few nearest neighbours to each lipid) as the observable, we used the HOP of the individual lipid tails. Assuming two hidden states (one for the fluid phase and one for the more ordered, gel-like phase), and assuming Gaussian emission probabilities for the HOP

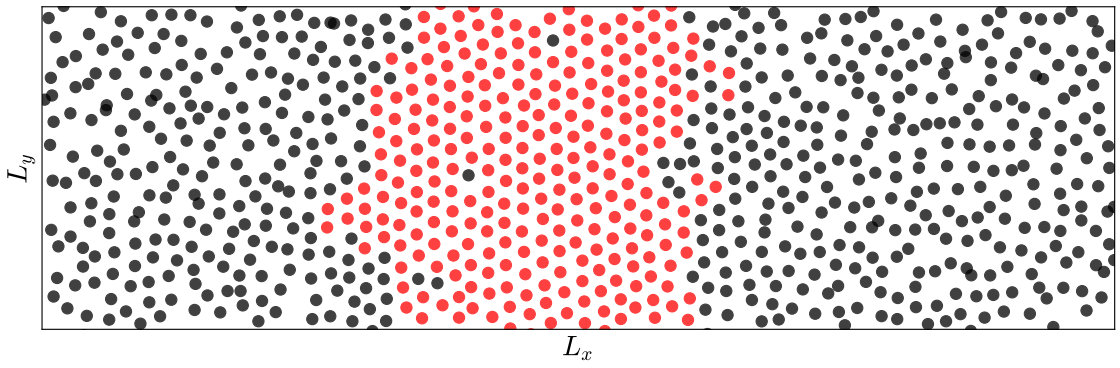

Figure 5.2: Position of lipid tails in the compressed leaflet of a MARTINI DLPC bilayer with asymmetry $\delta n = 3.75\%$ simulated at 297.5 K. Red points represent lipid tails identified as belonging to the ordered phase using a HMM.

values, we used the implementation of the relevant algorithms in the `hmmlearn` Python package to attribute a phase state to each lipid tail at every frame of the trajectories. Fitting of model parameters using trajectories from simulations where ordered bands were present lead to identification of lipid tails in the ordered regions as belonging to a separate phase by the HMM. Fig. 5.2 shows the identification of lipid tails in an ordered band in the the compressed leaflet as belonging to the more ordered phase by the HMM in a simulation of MARTINI DLPC lipids with $\delta n = 3.75\%$ at 297.5 K.

We tried adding more observables to our model, using the average HOP of the 3 or 6 nearest points as 1 or 2 additional observable, without any discernible differences in the results of phase classification. We also considered adding a third hidden state to our model, hypothesizing that it might identify the points at the boundary between the ordered and disordered regions; However, this merely resulted in dividing the fluid phase into two states based on a HOP cutoff whose value depended on the specific trajectory.

A point worth noting is that while we used Gaussian distributions for emission probabilities of the hidden Markov model, given the fact that the range of values for HOP is limited between 0 and 1, beta distributions resemble the shape of the probability distribution of HOP values in the two phases better. Nonetheless, we currently do not have a theory predicting these probability distributions. Fig. 5.3 shows the probability distribution of HOP values of the MARTINI DLPC lipid tails of the compressed leaflet of an asymmetric bilayer with $\delta n = 3.75\%$ simulated at 297.5 K, for the two different phases identified by the HMM.

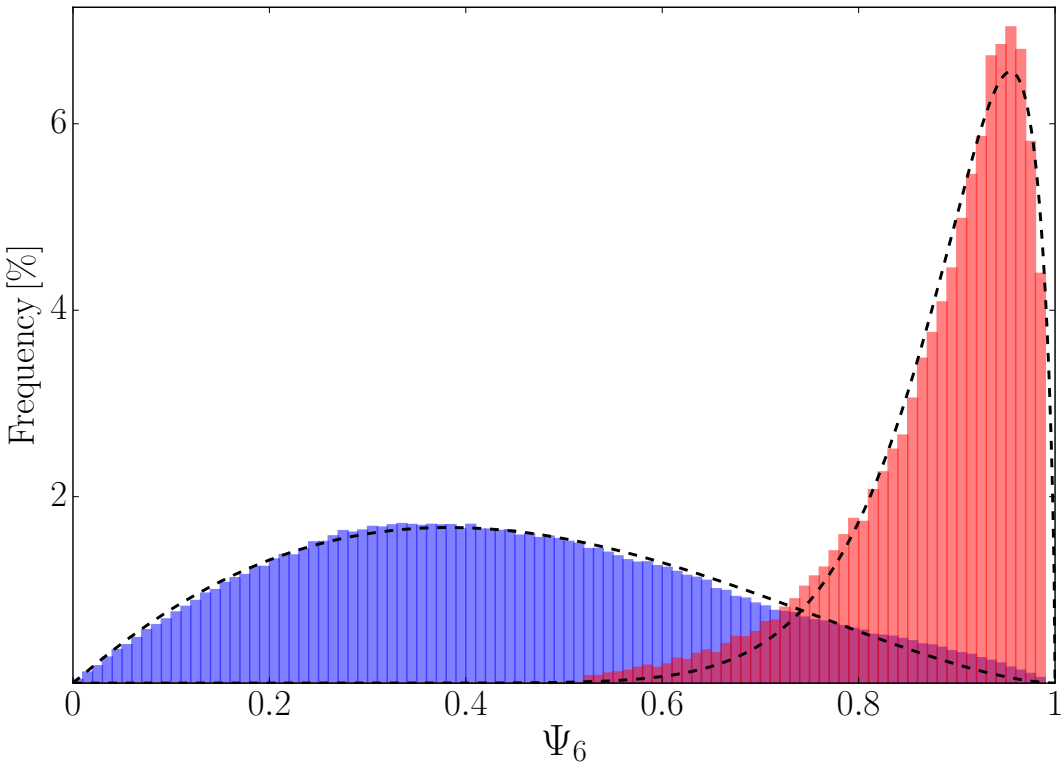

Figure 5.3: Distribution of hexatic order parameter Ψ_6 values of the MARTINI DLPC lipid tails of the compressed leaflet of an asymmetric ($\delta n = 3.75\%$) bilayer at 297.5 K. Blue represents the fluid phase and red represents the gel phase, as identified by the HMM. Dashed lines show beta distributions fitted to the data.

5.2 Barrier crossing issues

We have argued that increasing differential stress past a critical threshold leads to stiffening of bilayers as a result of formation of highly-ordered regions in the compressed leaflet. This suggest a first order transition from a state without the existence of the ordered phase to a state with it, with the latter state having a lower free energy value past the critical asymmetry. Furthermore, this hints at the existence of a free energy barrier between the global thermodynamic equilibrium state and the less favourable local minimum, which needs to be crossed if the system is initially in the local minimum. Our simulations of MARTINI lipids at temperatures and asymmetries where we expect existence of an ordered band to be the favoured state of the system, supports this idea. Fig. 5.4 shows the fraction of lipid tails in the ordered phase (as determined by HMM) of the compressed leaflet as a function of time for 5 identical (except the random seed for initial velocities) simulations of asymmetric MARTINI DLPC bilayers with $\delta n = 4.25\%$ at 297.5 K. While having an ordered band

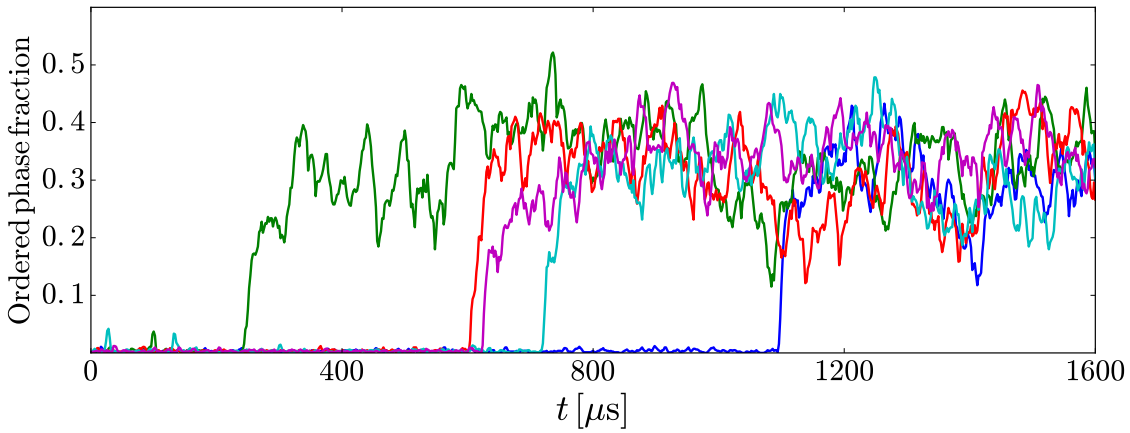

Figure 5.4: The fraction of lipid tails in the ordered phase of the compressed leaflet for 5 simulations of asymmetric MARTINI DLPC bilayers with $\delta n = 4.25\%$ at 297.5 K, as a function of time.

is the favourable state for this system, it took between 300 to 1100 μs for the system to pass the barrier between the fully fluid state and the phase coexistence state.

It is also worth noting that finite-size effects can significantly affect the free energy landscape of the system. As an example, it is intuitively clear that a narrower bilayer strip would facilitate formation of ordered bands by making it easier for them to span the width of the strip and link via the periodic boundary. We could verify this by conducting 5 simulations of asymmetric MARTINI DLPC bilayers with $\delta n = 4.25\%$ at 297.5 K with an increased width of 10 nm (instead of previous value of 8 nm) and observing that in none of these simulations an ordered band spanning the entire with of the strip was formed during the 1600 ns run of the simulations.

A more thorough treatment of this first order transition necessitates development of a theoretical framework for predicting the free energy of these stress asymmetric systems and such analysis is beyond the preview of this work.

Chapter 6

Summary and Outlook

An almost ubiquitous feature of biological lipid membranes is asymmetry between their constituent leaflets. On time scales shorter than lipid flip-flop time, a lipid bilayer can exhibit metastable asymmetry due to two distinct sources: one due to lipid composition of the leaflets, the other due to their lateral stress. Therefore, characterizing a bilayer's asymmetry through the compositional aspect alone is insufficient. However, these two asymmetries are not independent, and their interplay can affect mechanical properties of membranes in unexpected ways. We have proposed a theoretical framework for analyzing this interplay and its consequences, such as existence of residual stress in an asymmetric membrane whose leaflets' area has been chosen to match their symmetric counterparts.

Using coarse-grained MD simulations, we have shown that imposing differential stress onto a lipid bilayer can drive a transition in which the bending modulus discontinuously increases, and propose this as the explanation for observation of increased rigidity for asymmetric membranes in recent experiments.

A stress imbalance between bilayer leaflets, and its impact on any number of membrane properties, is a matter of practical concern, since recently proposed methods for creating compositionally asymmetric membranes might inadvertently also render them differentially stressed. We have explicitly shown how this might happen in the phase transfer protocol, but it is not difficult to imagine causes for imbalance that arise in the lipid exchange protocol. In fact, in many cases of practical relevance a bilayer's spontaneous materials curvature $K_{0\mathrm{b}}$ is so large that macroscopic membrane systems (such as giant unilamellar vesicles, especially deflated ones) should be unstable against tubulation without a counterbalancing differential stress.

We have also shown that incorporating lipid species that can rapidly transition between leaflets, such as cholesterol, renders the situation even more complex. One possibility is that their redistribution expunges differential stress, as recently observed by Miettinen and Lipowsky, but this is not the generic outcome. The chemical potential of these molecules may contain contributions that expressly favor their uneven distribution between leaflets, and so adding them to a stress-balanced membrane

might actually create differential stress. In the case of cholesterol this can easily happen when the two leaflets differ in their tail order, as is for instance the case in the plasma membrane.

Investigating a MARTINI DLPC membrane across a range of temperatures, we found that the asymmetry at which the transition occurs increases with temperature, more quickly so for larger temperatures. We attribute the stiffening to the formation of ordered domains in the compressed leaflet that resemble a gel phase, but cannot immediately permeate the entire compressed leaflet since the coupling between the two leaflets imposes a constraint on what area changes are possible. In particular, the existence of an ordered-disordered coexistence region is not merely a kinetic artifact, even though the breakup of the ordered phase into smaller subdomains might well be. If the emergence of local ordered domains in a fluid background drives an increase in bending rigidity, this implies that (*i*) membranes close to their main transition can be very easily driven into the stiffened regime, but also that (*ii*) no mechanism for further stiffening is available if the initial symmetric membrane is already in the gel phase.

Our findings suggest there is a window of temperature above the membrane's gel transition point over which a given asymmetry can induce stiffening. We estimated that range to be on the order of 10 °C from our MARTINI DLPC simulations, but this might be too conservative of an estimate for two independent reasons: Firstly, we know that the gel transition in atomistic systems affects material properties much more strongly than what coarse-grained models suggest. For example, the bending rigidity of gel-phase membranes is thought to be at least an order of magnitude larger than that of their fluid phase counterparts [163, 165, 166, 168, 171]. The MARTINI DLPC gel phase was recently measured to be about 7 times stiffer than the fluid phase [75], but at a temperature 35 °C below the fluid system. Extrapolating the fluid and gel rigidities to the transition temperature, the difference reduces to a factor of 3–4 [162], which is less than what is expected for real systems or in atomistic simulations. Secondly, we have shown that the critical asymmetries obtained in our simulations are subject to systematic finite size effects, in that their values are smaller in bigger systems. Given how much smaller our systems are compared to those investigated in experiments, this discrepancy between our model predictions and experimentally relevant scales could have a significant effect on the transition window. Our buckles are about 40 nm long, while the GUVs studied in Refs. [90, 92] have a diameter between about 40 µm and 110 µm, showing that we need to bridge about 3 orders of magnitude (we get a similar ratio if we instead compare typical curvatures). Specifically, if real (and therefore bigger) systems can be driven into a stiffer phase by smaller asymmetries than the ones our model membranes require, then the overall temperature range over which this is possible could be substantially larger.

These two points might explain an otherwise puzzling observation about the experimental model systems that first reported the phenomenon of asymmetry-induced

stiffening. The measurements performed in Ref. [84, 90] use POPC and DOPC (1,2-dioleoyl-*sn*-glycero-3-phosphocholine), and of those two POPC is the high melting lipid ($T_\mathrm{m} \approx -2.5\,^\circ\mathrm{C}$ [170]). Since the measurements had been done at approximately room temperature (22 °C for [84], 21 °C for [90]) both experiments were approximately 24 °C above the gel transition temperature of the high melting lipid. The viable temperature range of 10 °C we derived based on our MARTINI DLPC simulations would hence be too small to explain the effect. A larger range due to finite size effects could remove this discrepancy.

Also puzzling, but for a different reason, are the stiffening results reported in Ref. [92], where DMPC (1,2-dimyristoyl-*sn*-glycero-3-phosphocholine) and DOPC were used. In this case DMPC is the high melting lipid, with a transition temperature of 23.4 °C [163]. The experiments were conducted at 22.5 °C, nominally a degree below the gel transition, but the rigidity of a pure DMPC vesicle was reported to be $(11.8 \pm 1.3) \times 10^{-20}\,\mathrm{J} = (28.9 \pm 3.2) k_\mathrm{B}T$, a value entirely compatible with a fluid phase membrane. The authors correctly point out that the rigidity of DMPC decreases (within an $\approx 3\,^\circ\mathrm{C}$ window) upon approaching the main phase transition from above and is smallest at the transition, an effect known as "anomalous swelling" [163,195,196]. But their interpretation that this might indicate a coexistence of fluid- and gel-state lipids at the point of measurement, leading to the formation of periodic membrane ripples, strikes us as implausible in view of the actual temperature dependence of DMPC's bending rigidity, which exhibits an abrupt and very steep increase of the rigidity below the gel transition [163]. It is unclear why the DMPC phase was so soft, but we suspect that trace contaminations [32] or remnants of oil from the microfluidic fabrication process have slightly lowered the transition temperature. Still, in an asymmetric DMPC/DOPC system the DMPC leaflet would be extremely close to the gel transition, and even a small stress asymmetry (triggered for example by the mismatch between the equilibrium area per lipid in a monolayer compared to a bilayer) could induce stiffening.

At any rate, our findings indicate that (*i*) the gel transition in differentially stressed membranes is of potentially significant interest for asymmetric membranes, and that (*ii*) the matter in which it manifests is more subtle than the all-or-nothing transition we see for symmetric membranes. We find finite domains of the ordered phase in the compressed leaflet, which render these systems inhomogeneous composites. Their elastic behavior can be approximately described by an effective modulus in cases such as the simple buckles we study, in which these domains give rise to well localized stripes that give the half-buckles that host them an identifiable rigidity. But in more complex situations this might not be quite so easy. For instance, in larger membranes with overall lower curvatures we expect the curvature localization to flat regions to be less effective, rendering the overall composite less well organized. Modeling the thermodynamic and elastic properties of such stress-asymmetric systems will hence require new ideas. But given that their properties conceivably link readily accessible observables (such as transition temperatures or gel fractions) with

system properties for which currently no way of measuring them exists (such as the differential stress), one may hope that a good theory can turn some of the former observables into proxies for the latter, and thereby deepen our understanding of the microscopic physics underlying asymmetric membrane thermodynamics. Aside from developing a theory treating the asymmetry-induced phase transition evidently occurring in these membranes, and looking for evidence of differential stress in model lipid bilayers using appropriate proxies, replication of results presented in this work using atomistic models could be another avenue for deepening our understanding of asymmetric membranes.

Chapter 7

Glossary

For the convenience of the reader, this glossary gives a list of the most common mathematical symbols and notations used in this thesis.

Symbol	**description**
$\pm$	subscript denoting upper (+) or lower (−) leaflet
$\alpha_\pm$	fraction of membrane expansion modulus due to ±-leaflet, $= K_{A,\mathrm{m}\pm}/K_A$
α_{sc}	stress-curvature parameter, Eqn. (2.12)
$\mathcal{A}_\pm$	equilibrium area of a mixed (flat) leaflet, Eqn. (4.1)
d	total bilayer thickness
d_{h}	thickness of a bilayer's hydrophobic region
δ	dimensionless curvature softening parameter
δn	number asymmetry, Eqn. (3.15)
δn_{c}	stiffening critical asymmetry
$g_\pm$	cholesterol partitioning free energy into ± leaflet, Eqn. (4.1)
Δg	cholesterol partitioning difference, $= g_+ - g_-$
γ	buckling strain, Eqn. (3.1)eq:gamma-pm
$\gamma_\pm$	monolayer area strain, Eqn. (2.5)
K	curvature of bilayer, measured at midplane
$K_{A,\mathrm{m}\pm}$	monolayer area expansion modulus, Eqn. (2.6a)
K_A	bilayer area expansion modulus, $= K_{A,+} + K_{A,-}$
$K_{0\mathrm{b}}$	a bilayer's spontaneous materials curvature, created due to lipid curvature, Eqn. (2.2)
$K_{0\mathrm{s}}$	bilayer curvature at which differential stress vanishes, Eqn. (2.5)
$K_0^\star$	bilayer curvature at which overall bending and stretching energy is minimized, Eqn. (2.9)
$K_{\mathrm{m}\pm}$	spontaneous leaflet curvature due to lipids, Eqn. (2.1)
$\bar{K}$	surface-averaged curvature, Eqn. (2.6c)
κ	bilayer curvature modulus, Eqn. (2.3)
κ_{nl}	nonlocal bilayer curvature modulus, Eqn. (2.7)
$\kappa_{\mathrm{m}\pm}$	monolayer curvature modulus, Eqn. (2.1)

ℓ	curvature crossover length, Eqn. (3.4)
Ψ_6	hexatic order parameter, Eqn. (3.10)
χ^2_ν	reduced chi-squared, Eqn. (3.17)
Σ	net bilayer tension, $= \Sigma_+ + \Sigma_-$
$\Sigma_\pm$	individual leaflet tension
$\Sigma_\pm^{(\mathrm{res})}$	residual differential stress in an area balanced membrane, Eqn. (2.15)
$\sigma_0(z)$	lateral stress profile, Eqn. (3.6)
$\mathcal{T}$	torque density, Eqn. (2.16)
$\mathcal{T}_\pm$	monolayer torque density, Eqn. (2.22)
$z_\pm$	distance of upper (+) or lower (−) neutral surface from bilayer midplane
z_0	value of $z_\pm$ if we assume $z_+ \approx z_-$

Bibliography

[1] Andrej Shevchenko and Kai Simons. Lipidomics: coming to grips with lipid diversity. *Nature reviews Molecular cell biology*, 11(8):593–598, 2010.

[2] Bruce Alberts. Molecular biology of the cell, 2008.

[3] Bruce Alberts, Dennis Bray, Karen Hopkin, Alexander D Johnson, Julian Lewis, Martin Raff, Keith Roberts, and Peter Walter. *Essential cell biology*. Garland Science, 2015.

[4] Ira R Cooke and Markus Deserno. Coupling between lipid shape and membrane curvature. *Biophysical journal*, 91(2):487–495, 2006.

[5] Jacob N Israelachvili, D John Mitchell, and Barry W Ninham. Theory of self-assembly of hydrocarbon amphiphiles into micelles and bilayers. *Journal of the Chemical Society, Faraday Transactions 2: Molecular and Chemical Physics*, 72:1525–1568, 1976.

[6] Thomas J Piggot, Jane R Allison, Richard B Sessions, and Jonathan W Essex. On the calculation of acyl chain order parameters from lipid simulations. *Journal of chemical theory and computation*, 13(11):5683–5696, 2017.

[7] Ludmila Bezrukov, Paul S Blank, Ivan V Polozov, and Joshua Zimmerberg. An adhesion-based method for plasma membrane isolation: evaluating cholesterol extraction from cells and their membranes. *Analytical biochemistry*, 394(2):171–176, 2009.

[8] Akash Das, Joseph L Goldstein, Donald D Anderson, Michael S Brown, and Arun Radhakrishnan. Use of mutant 125i-perfringolysin o to probe transport and organization of cholesterol in membranes of animal cells. *Proceedings of the National Academy of Sciences*, 110(26):10580–10585, 2013.

[9] Y Lange, MH Swaisgood, BV Ramos, and TL Steck. Plasma membranes contain half the phospholipid and 90% of the cholesterol and sphingomyelin in cultured human fibroblasts. *Journal of Biological Chemistry*, 264(7):3786–3793, 1989.

[10] Kakoli Mitra, Iban Ubarretxena-Belandia, Tomohiko Taguchi, Graham Warren, and Donald M Engelman. Modulation of the bilayer thickness of exocytic pathway membranes by membrane proteins rather than cholesterol. *Proceedings of the National Academy of Sciences*, 101(12):4083–4088, 2004.

[11] Rumiana Koynova and Martin Caffrey. Phases and phase transitions of the phosphatidylcholines. *Biochimica et Biophysica Acta (BBA) - Reviews on Biomembranes*, 1376(1):91–145, 1998.

[12] John F. Nagle and Stephanie Tristram-Nagle. Structure of lipid bilayers. *Biochimica et Biophysica Acta (BBA) - Reviews on Biomembranes*, 1469(3):159–195, 2000.

[13] Tim Bartels, Ravi S Lankalapalli, Robert Bittman, Klaus Beyer, and Michael F Brown. Raftlike mixtures of sphingomyelin and cholesterol investigated by solid-state 2h nmr spectroscopy. *Journal of the American Chemical Society*, 130(44):14521–14532, 2008.

[14] Gerald W Feigenson. Phase boundaries and biological membranes. *Annu. Rev. Biophys. Biomol. Struct.*, 36:63–77, 2007.

[15] Sarah L Veatch and Sarah L Keller. Seeing spots: complex phase behavior in simple membranes. *Biochimica et Biophysica Acta (BBA)-Molecular Cell Research*, 1746(3):172–185, 2005.

[16] Michael P Allen and Dominic J Tildesley. *Computer simulation of liquids*. Oxford university press, 2017.

[17] Daan Frenkel and Berend Smit. *Understanding molecular simulation: from algorithms to applications*, volume 1. Elsevier, 2001.

[18] Philippe H Hünenberger. Thermostat algorithms for molecular dynamics simulations. *Advanced computer simulation*, pages 105–149, 2005.

[19] Sergei Izvekov and Gregory A Voth. A multiscale coarse-graining method for biomolecular systems. *The Journal of Physical Chemistry B*, 109(7):2469–2473, 2005.

[20] Martin Karplus and J Andrew McCammon. Molecular dynamics simulations of biomolecules. *Nature structural biology*, 9(9):646–652, 2002.

[21] Ross A Lippert, Cristian Predescu, Douglas J Ierardi, Kenneth M Mackenzie, Michael P Eastwood, Ron O Dror, and David E Shaw. Accurate and efficient integration for molecular dynamics simulations at constant temperature and pressure. *The Journal of chemical physics*, 139(16):10B621_1, 2013.

[22] Siewert J Marrink, Valentina Corradi, Paulo CT Souza, Helgi I Ingolfsson, D Peter Tieleman, and Mark SP Sansom. Computational modeling of realistic cell membranes. *Chemical reviews*, 119(9):6184–6226, 2019.

[23] Glenn J Martyna, Douglas J Tobias, and Michael L Klein. Constant pressure molecular dynamics algorithms. *The Journal of chemical physics*, 101(5):4177–4189, 1994.

[24] J Andrew McCammon, Bruce R Gelin, and Martin Karplus. Dynamics of folded proteins. *Nature*, 267(5612):585–590, 1977.

[25] Florian Müller-Plathe. Coarse-graining in polymer simulation: from the atomistic to the mesoscopic scale and back. *ChemPhysChem*, 3(9):754–769, 2002.

[26] WG Noid, Jhih-Wei Chu, Gary S Ayton, Vinod Krishna, Sergei Izvekov, Gregory A Voth, Avisek Das, and Hans C Andersen. The multiscale coarse-graining method. i. a rigorous bridge between atomistic and coarse-grained models. *The Journal of chemical physics*, 128(24):244114, 2008.

[27] Michele Parrinello and Aneesur Rahman. Polymorphic transitions in single crystals: A new molecular dynamics method. *Journal of Applied physics*, 52(12):7182–7190, 1981.

[28] Christine Peter and Kurt Kremer. Multiscale simulation of soft matter systems–from the atomistic to the coarse-grained level and back. *Soft Matter*, 5(22):4357–4366, 2009.

[29] Karl E Petersen. *Ergodic theory*, volume 2. Cambridge University Press, 1989.

[30] Valentina Tozzini. Coarse-grained models for proteins. *Current opinion in structural biology*, 15(2):144–150, 2005.

[31] Gregory A Voth. *Coarse-graining of condensed phase and biomolecular systems*. CRC press, 2008.

[32] Rumiana Dimova. Recent developments in the field of bending rigidity measurements on membranes. *Advances in colloid and interface science*, 208:225–234, 2014.

[33] M Hamm and MM Kozlov. Elastic energy of tilt and bending of fluid membranes. *The European Physical Journal E*, 3(4):323–335, 2000.

[34] David Needham and Rashmi S Nunn. Elastic deformation and failure of lipid bilayer membranes containing cholesterol. *Biophysical journal*, 58(4):997–1009, 1990.

[35] Siewert J Marrink, Alex H De Vries, and Alan E Mark. Coarse grained model for semiquantitative lipid simulations. *The Journal of Physical Chemistry B*, 108(2):750–760, 2004.

[36] Siewert J Marrink, Jelger Risselada, and Alan E Mark. Simulation of gel phase formation and melting in lipid bilayers using a coarse grained model. *Chemistry and physics of lipids*, 135(2):223–244, 2005.

[37] Siewert-Jan Marrink and Alan E Mark. Molecular view of hexagonal phase formation in phospholipid membranes. *Biophysical journal*, 87(6):3894–3900, 2004.

[38] Siewert J Marrink, H Jelger Risselada, Serge Yefimov, D Peter Tieleman, and Alex H De Vries. The martini force field: coarse grained model for biomolecular simulations. *The journal of physical chemistry B*, 111(27):7812–7824, 2007.

[39] Xavier Periole and Siewert-Jan Marrink. The martini coarse-grained force field. *Biomolecular Simulations*, pages 533–565, 2013.

[40] Susan L Duncan, Indranil S Dalal, and Ronald G Larson. Molecular dynamics simulation of phase transitions in model lung surfactant monolayers. *Biochim. Biophys. Acta, Biomembr.*, 1808(10):2450–2465, 2011.

[41] Helgi I Ingólfsson, Harsh Bhatia, Talia Zeppelin, WF Drew Bennett, Kristy A Carpenter, Pin-Chia Hsu, Gautham Dharuman, Peer-Timo Bremer, Birgit Schiøtt, Felice C Lightstone, et al. Capturing biologically complex tissue-specific membranes at different levels of compositional complexity. *The Journal of Physical Chemistry B*, 124(36):7819–7829, 2020.

[42] M. N. Melo, Helgi I. Ingólfsson, and Siewert Jan Marrink. Parameters for martini sterols and hopanoids based on a virtual-site description. *J. Chem. Phys.*, 143(24):243152, 2015.

[43] O H Samuli Ollila, H Jelger Risselada, Martti Louhivuori, Erik Lindahl, Ilpo Vattulainen, and Siewert J Marrink. 3d pressure field in lipid membranes and membrane-protein complexes. *Phys. Rev. Lett.*, 102(7):078101, 2009.

[44] Juan M Vanegas, Alejandro Torres-Sánchez, and Marino Arroyo. Importance of force decomposition for local stress calculations in biomembrane molecular simulations. *J. Chem. Theory Comput.*, 10(2):691–702, 2014.

[45] Qaiser Waheed, Richard Tjörnhammar, and Olle Edholm. Phase transitions in coarse-grained lipid bilayers containing cholesterol by molecular dynamics simulations. *Biophys. J.*, 103(10):2125–2133, 2012.

[46] F-Xabier Contreras, Lissete Sánchez-Magraner, Alicia Alonso, and Félix M Goñi. Transbilayer (flip-flop) lipid motion and lipid scrambling in membranes. *FEBS letters*, 584(9):1779–1786, 2010.

[47] Hannah M Hankins, Ryan D Baldridge, Peng Xu, and Todd R Graham. Role of flippases, scramblases and transfer proteins in phosphatidylserine subcellular distribution. *Traffic*, 16(1):35–47, 2015.

[48] KC Courtney, W Pezeshkian, R Raghupathy, C Zhang, A Darbyson, JH Ipsen, DA Ford, H Khandelia, JF Presley, and X Zha. C24 sphingolipids govern the transbilayer asymmetry of cholesterol and lateral organization of model and live-cell plasma membranes. *Cell reports*, 24(4):1037–1049, 2018.

[49] David L Daleke. Phospholipid flippases. *Journal of Biological Chemistry*, 282(2):821–825, 2007.

[50] Milka Doktorova, Jessica L Symons, and Ilya Levental. Structural and functional consequences of reversible lipid asymmetry in living membranes. *Nature chemical biology*, 16(12):1321–1330, 2020.

[51] Naoki Hisamoto, Anna Tsuge, Strahil Iv Pastuhov, Tatsuhiro Shimizu, Hiroshi Hanafusa, and Kunihiro Matsumoto. Phosphatidylserine exposure mediated by abc transporter activates the integrin signaling pathway promoting axon regeneration. *Nature communications*, 9(1):1–11, 2018.

[52] Shu-Lin Liu, Ren Sheng, Jae Hun Jung, Li Wang, Ewa Stec, Matthew J O'Connor, Seohyoen Song, Rama Kamesh Bikkavilli, Robert A Winn, Daesung Lee, et al. Orthogonal lipid sensors identify transbilayer asymmetry of plasma membrane cholesterol. *Nature chemical biology*, 13(3):268–274, 2017.

[53] JH Lorent, KR Levental, L Ganesan, G Rivera-Longsworth, E Sezgin, M Doktorova, E Lyman, and I Levental. Plasma membranes are asymmetric in lipid unsaturation, packing and protein shape. *Nature chemical biology*, 16(6):644–652, 2020.

[54] Amanda MacKenzie, Heather L Wilson, Endre Kiss-Toth, Steven K Dower, R Alan North, and Annmarie Surprenant. Rapid secretion of interleukin-1β by microvesicle shedding. *Immunity*, 15(5):825–835, 2001.

[55] Maria Makarova and Dylan M Owen. Asymmetry across the membrane. *Nature chemical biology*, 16(6):605–606, 2020.

[56] Sophie Martin, Isabel Pombo, Pascal Poncet, B David, M Arock, and Ulrich Blank. Immunologic stimulation of mast cells leads to the reversible exposure of phosphatidylserine in the absence of apoptosis. *International archives of allergy and immunology*, 123(3):249–258, 2000.

[57] Cédric Montigny, Joseph Lyons, Philippe Champeil, Poul Nissen, and Guillaume Lenoir. On the molecular mechanism of flippase-and scramblase-mediated phospholipid transport. *Biochimica et Biophysica Acta (BBA)-Molecular and Cell Biology of Lipids*, 1861(8):767–783, 2016.

[58] Brent Neumann, Sean Coakley, Rosina Giordano-Santini, Casey Linton, Eui Seung Lee, Akihisa Nakagawa, Ding Xue, and Massimo A Hilliard. Eff-1-mediated regenerative axonal fusion requires components of the apoptotic pathway. *Nature*, 517(7533):219–222, 2015.

[59] Stéphane Ory, Mara Ceridono, Fanny Momboisse, Sébastien Houy, Sylvette Chasserot-Golaz, Dimitri Heintz, Valérie Calco, Anne-Marie Haeberlé, Flor A Espinoza, Peter J Sims, et al. Phospholipid scramblase-1-induced lipid reorganization regulates compensatory endocytosis in neuroendocrine cells. *Journal of Neuroscience*, 33(8):3545–3556, 2013.

[60] A Rawyler, PH Van der Schaft, B Roelofsen, and JAF Op den Kamp. Phospholipid localization in the plasma membrane of friend erythroleukemic cells and mouse erythrocytes. *Biochemistry*, 24(7):1777–1783, 1985.

[61] W Renooij, LMG Van Golde, RFA Zwaal, B Roelofsen, and LLM Van Deenen. Preferential incorporation of fatty acids at the inside of human erythrocyte membranes. *Biochimica et Biophysica Acta (BBA)-Biomembranes*, 363(2):287–292, 1974.

[62] Claudia M Rival, Wenhao Xu, Laura S Shankman, Sho Morioka, Sanja Arandjelovic, Chang Sup Lee, Karen M Wheeler, Ryan P Smith, Lisa B Haney, Brant E Isakson, et al. Phosphatidylserine on viable sperm and phagocytic machinery in oocytes regulate mammalian fertilization. *Nature communications*, 10(1):1–13, 2019.

[63] Noel M Rysavy, Lori MN Shimoda, Alyssa M Dixon, Mark Speck, Alexander J Stokes, Helen Turner, and Eric Y Umemoto. Beyond apoptosis: the mechanism and function of phosphatidylserine asymmetry in the membrane of activating mast cells. *Bioarchitecture*, 4(4-5):127–137, 2014.

[64] MM Sperotto and A Ferrarini. The biophysics of cell membranes, 2017.

[65] WF Drew Bennett, Justin L MacCallum, Marlon J Hinner, Siewert J Marrink, and D Peter Tieleman. Molecular view of cholesterol flip-flop and chemical potential in different membrane environments. *Journal of the American Chemical Society*, 131(35):12714–12720, 2009.

[66] RJ Bruckner, SS Mansy, A Ricardo, L Mahadevan, and JW Szostak. Flip-flop-induced relaxation of bending energy: implications for membrane remodeling. *Biophysical journal*, 97(12):3113–3122, 2009.

[67] Sunhwan Jo, Huan Rui, Joseph B Lim, Jeffery B Klauda, and Wonpil Im. Cholesterol flip-flop: insights from free energy simulation studies. *The Journal of Physical Chemistry B*, 114(42):13342–13348, 2010.

[68] Theodore L Steck, Jin Ye, and Yvonne Lange. Probing red cell membrane cholesterol movement with cyclodextrin. *Biophysical journal*, 83(4):2118–2125, 2002.

[69] Theodore L Steck and Yvonne Lange. Transverse distribution of plasma membrane bilayer cholesterol: picking sides. *Traffic*, 19(10):750–760, 2018.

[70] Stefan M van den Eijnde, Maurice JB van den Hoff, Chris PM Reutelingsperger, Waander L van Heerde, Mieke ER Henfling, Christl Vermeij-Keers, Bert Schutte, Marcel Borgers, and Frans CS Ramaekers. Transient expression of phosphatidylserine at cell-cell contact areas is required for myotube formation. *Journal of cell science*, 114(20):3631–3642, 2001.

[71] PH Van der Schaft, B Roelofsen, JAF Op den Kamp, and LLM Van Deenen. Phospholipid asymmetry during erythropoiesis. a study on friend erythroleukemic cells and mouse reticulocytes. *Biochimica et Biophysica Acta (BBA)-Biomembranes*, 900(1):103–115, 1987.

[72] AJ Verkleij, RFA Zwaal, B Roelofsen, P Comfurius, D Kastelijn, and LLM Van Deenen. The asymmetric distribution of phospholipids in the human red cell membrane. a combined study using phospholipases and freeze-etch electron microscopy. *Biochimica et Biophysica Acta (BBA)-Biomembranes*, 323(2):178–193, 1973.

[73] Hiroshi Noguchi. Anisotropic surface tension of buckled fluid membranes. *Phys. Rev. E*, 83:061919, Jun 2011.

[74] Mingyang Hu, Patrick Diggins, and Markus Deserno. Determining the bending modulus of a lipid membrane by simulating buckling. *The Journal of Chemical Physics*, 138(21):214110, 2013.

[75] Patrick Diggins, Zachary A. McDargh, and Markus Deserno. Curvature softening and negative compressibility of gel-phase lipid membranes. *Journal of the American Chemical Society*, 137(40):12752–12755, 2015. PMID: 26413857.

[76] Paolo Carrara, Pasquale Stano, and Pier Luigi Luisi. Giant vesicles colonies: a model for primitive cell communities. *ChemBioChem*, 13(10):1497–1502, 2012.

[77] Chuanwei Cheng, Bo Liu, Huiying Yang, Weiwei Zhou, Li Sun, Rui Chen, Siu Fung Yu, Jixuan Zhang, Hao Gong, Handong Sun, et al. Hierarchical assembly of zno nanostructures on sno2 backbone nanowires: low-temperature hydrothermal preparation and optical properties. *ACS nano*, 3(10):3069–3076, 2009.

[78] Liang Cheng, Kai Yang, Yonggang Li, Jianhua Chen, Chao Wang, Mingwang Shao, Shuit-Tong Lee, and Zhuang Liu. Facile preparation of multifunctional upconversion nanoprobes for multimodal imaging and dual-targeted photothermal therapy. *Angewandte Chemie*, 123(32):7523–7528, 2011.

[79] Salvatore Chiantia, Petra Schwille, Andrey S Klymchenko, and Erwin London. Asymmetric guvs prepared by mβcd-mediated lipid exchange: an fcs study. *Biophysical journal*, 100(1):L1–L3, 2011.

[80] Milka Doktorova, Frederick A Heberle, Barbara Eicher, Robert F Standaert, John Katsaras, Erwin London, Georg Pabst, and Drew Marquardt. Preparation of asymmetric phospholipid vesicles for use as cell membrane models. *Nature protocols*, 13(9):2086–2101, 2018.

[81] Barbara Eicher, Drew Marquardt, Frederick A Heberle, Ilse Letofsky-Papst, Gerald N Rechberger, Marie-Sousai Appavou, John Katsaras, and Georg Pabst. Intrinsic curvature-mediated transbilayer coupling in asymmetric lipid vesicles. *Biophys. J.*, 114(1):146–157, 2018.

[82] Yuval Elani, Antony Gee, Robert V Law, and Oscar Ces. Engineering multicompartment vesicle networks. *Chemical Science*, 4(8):3332–3338, 2013.

[83] Yuval Elani, Robert V Law, and Oscar Ces. Vesicle-based artificial cells as chemical microreactors with spatially segregated reaction pathways. *Nature communications*, 5(1):1–5, 2014.

[84] Yuval Elani, Sowmya Purushothaman, Paula J Booth, John M Seddon, Nicholas J Brooks, Robert V Law, and Oscar Ces. Measurements of the effect of membrane asymmetry on the mechanical properties of lipid bilayers. *Chemical Communications*, 51(32):6976–6979, 2015.

[85] Thais A Enoki and Gerald W Feigenson. Asymmetric bilayers by hemifusion: method and leaflet behaviors. *Biophysical journal*, 117(6):1037–1050, 2019.

[86] Maik Hadorn, Eva Boenzli, Kristian T Sørensen, Davide De Lucrezia, Martin M Hanczyc, and Tetsuya Yomo. Defined dna-mediated assemblies of gene-expressing giant unilamellar vesicles. *Langmuir*, 29(49):15309–15319, 2013.

[87] Tsutomu Hamada, Yoko Miura, Yuuki Komatsu, Yuko Kishimoto, Mundelanji Vestergaard, and Masahiro Takagi. Construction of asymmetric cell-sized lipid vesicles from lipid-coated water-in-oil microdroplets. *The journal of physical chemistry B*, 112(47):14678–14681, 2008.

[88] Frederick A Heberle, Drew Marquardt, Milka Doktorova, Barbara Geier, Robert F Standaert, Peter Heftberger, Benjamin Kollmitzer, Jonathan D Nickels, Robert A Dick, Gerald W Feigenson, et al. Subnanometer structure of an

asymmetric model membrane: interleaflet coupling influences domain properties. *Langmuir*, 32(20):5195–5200, 2016.

[89] Peichi C Hu, Su Li, and Noah Malmstadt. Microfluidic fabrication of asymmetric giant lipid vesicles. *ACS applied materials & interfaces*, 3(5):1434–1440, 2011.

[90] K Karamdad, RV Law, JM Seddon, NJ Brooks, and O Ces. Studying the effects of asymmetry on the bending rigidity of lipid membranes formed by microfluidics. *Chem. Comm.*, 52(30):5277–5280, 2016.

[91] Qingqing Lin and Erwin London. The influence of natural lipid asymmetry upon the conformation of a membrane-inserted protein (perfringolysin o). *J. Biol. Chem.*, 289(9):5467–5478, 2014.

[92] Li Lu, William J Doak, Jeffrey W Schertzer, and Paul R Chiarot. Membrane mechanical properties of synthetic asymmetric phospholipid vesicles. *Soft Matter*, 12(36):7521–7528, 2016.

[93] Sandro Matosevic and Brian M Paegel. Layer-by-layer cell membrane assembly. *Nature chemistry*, 5(11):958–963, 2013.

[94] Jonathan D Nickels, Jeremy C Smith, and Xiaolin Cheng. Lateral organization, bilayer asymmetry, and inter-leaflet coupling of biological membranes. *Chem. Phys. Lipids*, 192:87–99, 2015.

[95] Vincent Noireaux and Albert Libchaber. A vesicle bioreactor as a step toward an artificial cell assembly. *Proceedings of the National Academy of Sciences*, 101(51):17669–17674, 2004.

[96] Vincent Noireaux, Yusuke T Maeda, and Albert Libchaber. Development of an artificial cell, from self-organization to computation and self-reproduction. *Proceedings of the National Academy of Sciences*, 108(9):3473–3480, 2011.

[97] Sophie Pautot, Barbara J Frisken, and DA Weitz. Engineering asymmetric vesicles. *Proceedings of the National Academy of Sciences*, 100(19):10718–10721, 2003.

[98] Vanesa L Perillo, Daniel A Penalva, Alejandro J Vitale, Francisco J Barrantes, and Silvia S Antollini. Transbilayer asymmetry and sphingomyelin composition modulate the preferential membrane partitioning of the nicotinic acetylcholine receptor in lo domains. *Arch. Biochem. Biophys.*, 591:76–86, 2016.

[99] Haden L Scott, Frederick A Heberle, John Katsaras, and Francisco N Barrera. Phosphatidylserine asymmetry promotes the membrane insertion of a transmembrane helix. *Biophys. J.*, 116(8):1495–1506, 2019.

[100] Pasquale Stano, Giordano Rampioni, Paolo Carrara, Luisa Damiano, Livia Leoni, and Pier Luigi Luisi. Semi-synthetic minimal cells as a tool for biochemical ict. *BioSystems*, 109(1):24–34, 2012.

[101] Zhenhai Zhang, Zhifei Li, Wei Yu, Kejie Li, Zhihong Xie, and Zhiguo Shi. Propulsion of liposomes using bacterial motors. *Nanotechnology*, 24(18):185103, 2013.

[102] Raktim Dasgupta, Markus S Miettinen, Nico Fricke, Reinhard Lipowsky, and Rumiana Dimova. The glycolipid gm1 reshapes asymmetric biomembranes and giant vesicles by curvature generation. *Proc. Nat. Acad. Sci. (USA)*, 115(22):5756–5761, 2018.

[103] Markus Deserno. Fluid lipid membranes: From differential geometry to curvature stresses. *Chem. Phys. Lipids*, 185:11–45, 2015.

[104] Manfredo P Do Carmo. *Differential Geometry of Curves and Surfaces: Revised and Updated Second Edition*. Dover, 2016.

[105] Santi Esteban-Martín, H Jelger Risselada, Jesús Salgado, and Siewert J Marrink. Stability of asymmetric lipid bilayers assessed by molecular dynamics simulations. *J. Am. Chem. Soc.*, 131(42):15194–15202, 2009.

[106] Evan A Evans. Bending resistance and chemically induced moments in membrane bilayers. *Biophys. J.*, 14(12):923–931, 1974.

[107] Evan A Evans. Minimum energy analysis of membrane deformation applied to pipet aspiration and surface adhesion of red blood cells. *Biophys. J.*, 30(2):265–284, 1980.

[108] Volkmar Heinrich, Saša Svetina, and Boštjan Žekš. Nonaxisymmetric vesicle shapes in a generalized bilayer-couple model and the transition between oblate and prolate axisymmetric shapes. *Phys. Rev. E*, 48(4):3112, 1993.

[109] Michael M Kozlov and M Winterhalter. Elastic moduli for strongly curved monoplayers. position of the neutral surface. *J. Phys. II (France)*, 1(9):1077–1084, 1991.

[110] S Leikin, Michael M Kozlov, Nola L Fuller, and R Peter Rand. Measured effects of diacylglycerol on structural and elastic properties of phospholipid membranes. *Biophys. J.*, 71(5):2623–2632, 1996.

[111] Ling Miao, Udo Seifert, Michael Wortis, and Hans-Günther Döbereiner. Budding transitions of fluid-bilayer vesicles: the effect of area-difference elasticity. *Phys. Rev. E*, 49(6):5389, 1994.

[112] Soohyung Park, Andrew H Beaven, Jeffery B Klauda, and Wonpil Im. How tolerant are membrane simulations with mismatch in area per lipid between leaflets? *J. Chem. Theory Comput.*, 11(7):3466–3477, 2015.

[113] R. P. Rand, N. L. Fuller, Sol M. Gruner, and V. Adrian Parsegian. Membrane curvature, lipid segregation, and structural transitions for phospholipids under dual-solvent stress. *Biochemistry*, 29(1):76–87, 1990.

[114] W Rawicz, KC Olbrich, T McIntosh, D Needham, and E Evans. Effect of chain length and unsaturation on elasticity of lipid bilayers. *Biophys. J.*, 79(1):328–339, 2000.

[115] Bartosz Różycki and Reinhard Lipowsky. Spontaneous curvature of bilayer membranes from molecular simulations: Asymmetric lipid densities and asymmetric adsorption. *J. Chem. Phys.*, 142(5):02B601_1, 2015.

[116] Bartosz Różycki and Reinhard Lipowsky. Membrane curvature generated by asymmetric depletion layers of ions, small molecules, and nanoparticles. *J. Chem. Phys.*, 145(7):074117, 2016.

[117] D. W. Allender, Alexander J. Sodt, and Michael Schick. Cholesterol-dependent bending energy is important in cholesterol distribution of the plasma membrane. *Biophys. J.*, 116:2356–2366, 2019.

[118] Udo Seifert, Ling Miao, H-G Döbereiner, and Michael Wortis. Budding transition for bilayer fluid vesicles with area-difference elasticity. In Reinhard Lipowsky, D Richter, and Kurt Kremer, editors, *The structure and conformation of amphiphilic membranes*, pages 93–96. Springer, 1992.

[119] Maria Maddalena Sperotto and Alberta Ferrarini. Spontaneous lipid flip-flop in membranes: A still unsettled picture from experiments and simulations. In Richard M. Epand and Jean-Marie Ruysschaert, editors, *The Biophysics of Cell Membranes: Biological Consequences*, pages 29–60. Springer Singapore, Singapore, 2017.

[120] Aparna Sreekumari and Reinhard Lipowsky. Lipids with bulky head groups generate large membrane curvatures by small compositional asymmetries. *J. Chem. Phys.*, 149(8):084901, 2018.

[121] Saša Svetina, Milan Brumen, and B Zeks. Lipid bilayer elasticity and the bilayer couple interpretation of red-cell shape transformations and lysis. *Stud. Biophys.*, 110(1-3):177–184, 1985.

[122] Mounir Traïkia, Dror E Warschawski, Olivier Lambert, Jean-Louis Rigaud, and Philippe F Devaux. Asymmetrical membranes and surface tension. *Biophys. J.*, 83(3):1443–1454, 2002.

[123] Richard M Venable, Frank LH Brown, and Richard W Pastor. Mechanical properties of lipid bilayers from molecular dynamics simulation. *Chem. Phys. Lipids*, 192:60–74, 2015.

[124] Milka Doktorova and Harel Weinstein. Accurate in silico modeling of asymmetric bilayers based on biophysical principles. *Biophys. J.*, 115(9):1638–1643, 2018.

[125] Markus Sakari Miettinen and Reinhard Lipowsky. Bilayer membranes with frequent flip-flops have tensionless leaflets. *Nano letters*, 19:5011–5016, 2019.

[126] Felix Campelo, Clement Arnarez, Siewert J Marrink, and Michael M Kozlov. Helfrich model of membrane bending: from gibbs theory of liquid interfaces to membranes as thick anisotropic elastic layers. *Adv. Colloid Interface Sci.*, 208:25–33, 2014.

[127] R. P. Rand, N. L. Fuller, Sol M. Gruner, and V. Adrian Parsegian. Membrane curvature, lipid segregation, and structural transitions for phospholipids under dual-solvent stress. *Biochemistry*, 29(1):76–87, 1990.

[128] W. Helfrich. Amphiphilic mesophases made of defects. In R. Balian, M. Kléman, and J. P. Poirier, editors, *Physics of Defects*. North Holland, Amsterdam, 1981.

[129] Ira R Cooke and Markus Deserno. Solvent-free model for self-assembling fluid bilayer membranes: stabilization of the fluid phase based on broad attractive tail potentials. *The Journal of chemical physics*, 123(22):224710, 2005.

[130] Ira R Cooke, Kurt Kremer, and Markus Deserno. Tunable generic model for fluid bilayer membranes. *Physical Review E*, 72(1):011506, 2005.

[131] Samuel Foley and Markus Deserno. Stabilizing leaflet asymmetry under differential stress in a highly coarse-grained lipid membrane model. *Journal of Chemical Theory and Computation*, 16(11):7195–7206, 2020.

[132] Gary Ayton and Gregory A Voth. Bridging microscopic and mesoscopic simulations of lipid bilayers. *Biophysical Journal*, 83(6):3357–3370, 2002.

[133] Erik G Brandt, Anthony R Braun, Jonathan N Sachs, John F Nagle, and Olle Edholm. Interpretation of fluctuation spectra in lipid bilayer simulations. *Biophysical journal*, 100(9):2104–2111, 2011.

[134] Grace Brannigan, Peter F Philips, and Frank LH Brown. Flexible lipid bilayers in implicit solvent. *Physical Review E*, 72(1):011915, 2005.

[135] Oded Farago. water-free computer model for fluid bilayer membranes. *The Journal of chemical physics*, 119(1):596–605, 2003.

[136] Rüdiger Goetz, Gerhard Gompper, and Reinhard Lipowsky. Mobility and elasticity of self-assembled membranes. *Phys. Rev. Lett.*, 82:221–224, Jan 1999.

[137] Erik Lindahl and Olle Edholm. Mesoscopic undulations and thickness fluctuations in lipid bilayers from molecular dynamics simulations. *Biophysical journal*, 79(1):426–433, 2000.

[138] Siewert J Marrink, Alex H De Vries, and Alan E Mark. Coarse grained model for semiquantitative lipid simulations. *The Journal of Physical Chemistry B*, 108(2):750–760, 2004.

[139] SJ Marrink and AE Mark. Effect of undulations on surface tension in simulated bilayers. *The Journal of Physical Chemistry B*, 105(26):6122–6127, 2001.

[140] ER May, A Narang, and DI Kopelevich. Molecular modeling of key elastic properties for inhomogeneous lipid bilayers. *Molecular Simulation*, 33(9-10):787–797, 2007.

[141] Eric R May, Atul Narang, and Dmitry I Kopelevich. Role of molecular tilt in thermal fluctuations of lipid membranes. *Physical Review E*, 76(2):021913, 2007.

[142] Hayato Shiba and Hiroshi Noguchi. Estimation of the bending rigidity and spontaneous curvature of fluid membranes in simulations. *Physical Review E*, 84(3):031926, 2011.

[143] Zun-Jing Wang and Daan Frenkel. Modeling flexible amphiphilic bilayers: a solvent-free off-lattice monte carlo study. *The Journal of chemical physics*, 122(23):234711, 2005.

[144] Max C Watson, Evgeni S Penev, Paul M Welch, and Frank LH Brown. Thermal fluctuations in shape, thickness, and molecular orientation in lipid bilayers. *The Journal of chemical physics*, 135(24):244701, 2011.

[145] Wolfgang Helfrich. Elastic properties of lipid bilayers: theory and possible experiments. *Zeitschrift für Naturforschung c*, 28(11-12):693–703, 1973.

[146] Zachary A McDargh. *Geometry, Mechanics, and Biology Applications for Membranes and Filaments*. PhD thesis, Carnegie Mellon University.

[147] W. Helfrich. Amphiphilic mesophases made of defects. In R. Balian, M. Kléman, and J. P. Poirier, editors, *Physics of Defects*. North Holland, Amsterdam, 1981.

[148] Mingyang Hu, Djurre H de Jong, Siewert J Marrink, and Markus Deserno. Gaussian curvature elasticity determined from global shape transformations and local stress distributions: a comparative study using the MARTINI model. *Faraday Discuss.*, 161:365–382, 2013.

[149] John Shipley Rowlinson and Benjamin Widom. *Molecular Theory of Capillarity*. Dover, Mineola, NY, 2002.

[150] Igal Szleifer, Diego Kramer, Avinoam Ben-Shaul, William M Gelbart, and Sam A Safran. Molecular theory of curvature elasticity in surfactant films. *J. Chem. Phys.*, 92(11):6800–6817, 1990.

[151] A Goebel and Klaus Lunkenheimer. Interfacial tension of the water/n-alkane interface. *Langmuir*, 13(2):369–372, 1997.

[152] M Mert Terzi and Markus Deserno. Lipid membranes: From self-assembly to elasticity. In *The Role of Mechanics in the Study of Lipid Bilayers*, pages 105–166. Springer, 2018.

[153] Pauli Virtanen, Ralf Gommers, Travis E Oliphant, Matt Haberland, Tyler Reddy, David Cournapeau, Evgeni Burovski, Pearu Peterson, Warren Weckesser, Jonathan Bright, et al. Scipy 1.0: fundamental algorithms for scientific computing in python. *Nature methods*, 17(3):261–272, 2020.

[154] Eric Jones, Travis Oliphant, Pearu Peterson, et al. Scipy: Open source scientific tools for python. 2001.

[155] Joachim Seelig. Deuterium magnetic resonance: theory and application to lipid membranes. *Quarterly reviews of biophysics*, 10(3):353–418, 1977.

[156] Louic S Vermeer, Bert L De Groot, Valérie Réat, Alain Milon, and Jerzy Czaplicki. Acyl chain order parameter profiles in phospholipid bilayers: computation from molecular dynamics simulations and comparison with 2 h nmr experiments. *European Biophysics Journal*, 36(8):919–931, 2007.

[157] M.J. Abraham, D. van der Spoel, E. Lindahl, B. Hess, and the GROMACS development team. *GROMACS User Manual version 2016-rc1*. www.gromacs.org, 2016.

[158] Mark James Abraham, Teemu Murtola, Roland Schulz, Szilárd Páll, Jeremy C Smith, Berk Hess, and Erik Lindahl. GROMACS: High performance molecular simulations through multi-level parallelism from laptops to supercomputers. *SoftwareX*, 1:19–25, 2015.

[159] Herman J C Berendsen, J P M van Postma, Wilfred F van Gunsteren, A R H J DiNola, and J R Haak. Molecular dynamics with coupling to an external bath. *J. Chem. Phys*, 81(8):3684–3690, 1984.

[160] Djurre H De Jong, Svetlana Baoukina, Helgi I Ingólfsson, and Siewert J Marrink. Martini straight: Boosting performance using a shorter cutoff and gpus. *Computer Physics Communications*, 199:1–7, 2016.

[161] Markus Deserno. Mesoscopic membrane physics: concepts, simulations, and selected applications. *Macromol. Rapid Comm.*, 30(9-10):752–771, 2009.

[162] Patrick Diggins IV. *Investigation of Elastic Properties of Lipids and Proteins using Computer Simulations*. PhD thesis, Carnegie Mellon University, (unpublished), 3 2016.

[163] R Dimova, B Pouligny, and C Dietrich. Pretransitional effects in dimyristoylphosphatidylcholine vesicle membranes: optical dynamometry study. *Biophys. J.*, 79(1):340–356, 2000.

[164] Norbert Kučerka, Stephanie Tristram-Nagle, and John F Nagle. Structure of fully hydrated fluid phase lipid bilayers with monounsaturated chains. *J. Membr. Biol.*, 208(3):193–202, 2006.

[165] Chau-Hwang Lee, Wan-Chen Lin, and Jyhpyng Wang. All-optical measurements of the bending rigidity of lipid-vesicle membranes across structural phase transitions. *Phys. Rev. E*, 64(2):020901, 2001.

[166] Siegfried Steltenkamp, Martin Michael Müller, Markus Deserno, Christian Hennesthal, Claudia Steinem, and Andreas Janshoff. Mechanical properties of pore-spanning lipid bilayers probed by atomic force microscopy. *Biophys. J.*, 91(1):217–226, 2006.

[167] K Olbrich, W Rawicz, D Needham, and E Evans. Water permeability and mechanical strength of polyunsaturated lipid bilayers. *Biophys. J.*, 79(1):321–327, 2000.

[168] L Fernandez-Puente, I Bivas, MD Mitov, and P Méléard. Temperature and chain length effects on bending elasticity of phosphatidylcholine bilayers. *Europhys. Lett.*, 28(3):181, 1994.

[169] Michael Heinrich, Aiwei Tian, Cinzia Esposito, and Tobias Baumgart. Dynamic sorting of lipids and proteins in membrane tubes with a moving phase boundary. *Proceedings of the National Academy of Sciences*, 107(16):7208–7213, 2010.

[170] Burton J Litman, E Neil Lewis, and Ira W Levin. Packing characteristics of highly unsaturated bilayer lipids: Raman spectroscopic studies of multilamellar phosphatidylcholine dispersions. *Biochemistry*, 30(2):313–319, 1991.

[171] Tze-Hsuan Liu, Jian-Long Xiao, Chau-Hwang Lee, and Jiunn-Yuan Lin. Measurement of membrane rigidity on trapped unilamellar phospholipid vesicles by using differential confocal microscopy. *Applied optics*, 50(19):3311–3315, 2011.

[172] Jocelyn M Rodgers, Jesper Sørensen, Frederick J-M de Meyer, Birgit Schiøtt, and Berend Smit. Understanding the phase behavior of coarse-grained model lipid bilayers through computational calorimetry. *J. Phys. Chem. B*, 116(5):1551–1569, 2012.

[173] Aurélien Roux, Damien Cuvelier, Pierre Nassoy, Jacques Prost, Patricia Bassereau, and Bruno Goud. Role of curvature and phase transition in lipid sorting and fission of membrane tubules. *The EMBO journal*, 24(8):1537–1545, 2005.

[174] Pieter R Cullis, David B. Fenske, and Michael J Hope. Physical properties and functional roles of lipids in membranes. In D. E. Vance and J. Vance, editors, *Biochemistry of Lipids, Lipoproteins, and Membranes*, chapter 1, pages 1–33. Amsterdam, 1996.

[175] Z Chen and R Peter Rand. The influence of cholesterol on phospholipid membrane curvature and bending elasticity. *Biophys. J.*, 73(1):267–276, 1997.

[176] Olle Edholm and John F Nagle. Areas of molecules in membranes consisting of mixtures. *Biophys. J.*, 89(3):1827–1832, 2005.

[177] Rubèn Serral Gracià, Natalya Bezlyepkina, Roland L Knorr, Reinhard Lipowsky, and Rumiana Dimova. Effect of cholesterol on the rigidity of saturated and unsaturated membranes: fluctuation and electrodeformation analysis of giant vesicles. *Soft Matter*, 6(7):1472–1482, 2010.

[178] Jonas Henriksen, Amy C Rowat, and John H Ipsen. Vesicle fluctuation analysis of the effects of sterols on membrane bending rigidity. *Eur. Biophys. J.*, 33(8):732–741, 2004.

[179] Wei-Chin Hung, Ming-Tao Lee, Fang-Yu Chen, and Huey W Huang. The condensing effect of cholesterol in lipid bilayers. *Biophys. J.*, 92(11):3960–3967, 2007.

[180] Norbert Kučerka, Jason D Perlmutter, Jianjun Pan, Stephanie Tristram-Nagle, John Katsaras, and Jonathan N Sachs. The effect of cholesterol on short-and long-chain monounsaturated lipid bilayers as determined by molecular dynamics simulations and x-ray scattering. *Biophys. J.*, 95(6):2792–2805, 2008.

[181] Felix Leeb and Lutz Maibaum. Spatially resolving the condensing effect of cholesterol in lipid bilayers. *Biophys. J.*, 115(11):2179–2188, 2018.

[182] Thomas J McIntosh. The effect of cholesterol on the structure of phosphatidylcholine bilayers. *Biochim. Biophys. Acta, Biomembr.*, 513(1):43–58, 1978.

[183] Jianjun Pan, Thalia T Mills, Stephanie Tristram-Nagle, and John F Nagle. Cholesterol perturbs lipid bilayers nonuniversally. *Phys. Rev. Lett*, 100(19):198103, 2008.

[184] Jianjun Pan, Stephanie Tristram-Nagle, and John F Nagle. Effect of cholesterol on structural and mechanical properties of membranes depends on lipid chain saturation. *Phys. Rev. E*, 80(2):021931, 2009.

[185] AJ Sodt, RM Venable, E Lyman, and RW Pastor. Nonadditive compositional curvature energetics of lipid bilayers. *Phys. Rev. Lett.*, 117(13):138104, 2016.

[186] Jianben Song and Richard E Waugh. Bending rigidity of SOPC membranes containing cholesterol. *Biophys. J.*, 64(6):1967–1970, 1993.

[187] Maria Maddalena Sperotto and Alberta Ferrarini. Spontaneous lipid flip-flop in membranes: A still unsettled picture from experiments and simulations. In Richard M. Epand and Jean-Marie Ruysschaert, editors, *The Biophysics of Cell Membranes: Biological Consequences*, pages 29–60. Springer Singapore, Singapore, 2017.

[188] Zhancheng Zhang, Lanyuan Lu, and Max L Berkowitz. Energetics of cholesterol transfer between lipid bilayers. *J. Phys. Chem. B*, 112(12):3807–3811, 2008.

[189] Leonard E Baum and Ted Petrie. Statistical inference for probabilistic functions of finite state markov chains. *The annals of mathematical statistics*, 37(6):1554–1563, 1966.

[190] Leonard E Baum, Ted Petrie, George Soules, and Norman Weiss. A maximization technique occurring in the statistical analysis of probabilistic functions of markov chains. *The annals of mathematical statistics*, 41(1):164–171, 1970.

[191] Richard Durbin, Sean R Eddy, Anders Krogh, and Graeme Mitchison. *Biological sequence analysis: probabilistic models of proteins and nucleic acids*. Cambridge university press, 1998.

[192] Lawrence R Rabiner. A tutorial on hidden markov models and selected applications in speech recognition. *Proceedings of the IEEE*, 77(2):257–286, 1989.

[193] Alexander J Sodt, Michael Logan Sandar, Klaus Gawrisch, Richard W Pastor, and Edward Lyman. The molecular structure of the liquid-ordered phase of lipid bilayers. *Journal of the American Chemical Society*, 136(2):725–732, 2014.

[194] Andrew Viterbi. Error bounds for convolutional codes and an asymptotically optimum decoding algorithm. *IEEE transactions on Information Theory*, 13(2):260–269, 1967.

[195] Nanjun Chu, Norbert Kučerka, Yufeng Liu, Stephanie Tristram-Nagle, and John F Nagle. Anomalous swelling of lipid bilayer stacks is caused by softening of the bending modulus. *Phys. Rev. E*, 71(4):041904, 2005.

[196] Philippe Méléard, Claire Gerbeaud, Tanja Pott, Laurent Fernandez-Puente, Isak Bivas, Marin D Mitov, Jean Dufourcq, and Pierre Bothorel. Bending elasticities of model membranes: influences of temperature and sterol content. *Biophys. J.*, 72(6):2616–2629, 1997.